

Development of a Blade Element Method for CFD Simulations of Helicopter Rotors using the Actuator Disk Approach

Daniel Viguera Leza

DEVELOPMENT OF A BLADE ELEMENT METHOD FOR CFD SIMULATIONS OF HELICOPTER ROTORS USING THE ACTUATOR DISK APPROACH

by

Daniel Viguera Leza

in partial fulfillment of the requirements for the degree of

Master of Science
in Aerospace Engineering

at the Delft University of Technology,
to be defended publicly on Friday January 19, 2018 at 13:00.

Supervisors:	Dr.ir. M. Voskuil,	TU Delft
	Dipl.-Ing. M. Schmid,	DLR
Thesis committee:	Prof.dr.ir L.L.M. Veldhuis,	TU Delft
	Dr.ir. M. Voskuil,	TU Delft
	Dr.ir. W.A.A.M. Bierbooms,	TU Delft

An electronic version of this thesis is available at <http://repository.tudelft.nl/>.

PREFACE

This thesis is the end of a journey that started six years ago. During this time, not only have I gained technical knowledge but also shared great moments with amazing people. After all these experiences, I feel confident and optimistic about the upcoming challenges.

I would like to express my gratitude to Thorsten Schwarz for offering me the opportunity to join his team at the DLR in Braunschweig, where the thesis work has been carried out. Special thanks to Matthias Schmid and Marc Wentrup for their continuous support and guidance throughout these months. I am also grateful for the assistance provided by Jan-Hendrik Wendisch and Gunther Wilke, who were always willing to share their sound knowledge of helicopters with me.

I really appreciate the guidelines and recommendations given by my supervisor, Mark Voskuil, which have been of great help along the project.

Last but not least, I would like to thank my friends and family, especially my parents and sister for their unconditional support.

*Daniel Viguera Leza
Delft, January 2018*

SUMMARY

The flow field subjected to the influence of the helicopter rotor is characterized by its three-dimensional pattern and unsteadiness. The accurate modeling of the flow around the rotor blades addressed by Computational Fluid Dynamics (CFD) simulations is associated with high computational costs. The complexity of the analysis can be reduced by means of simplified methods such as the actuator disk approach, where the rotor is modeled as a zero-thickness porous surface.

The CFD solver TAU developed at the German Aerospace Center (DLR) includes among its features an actuator disk module which transmits to the flow field prescribed time-averaged load distributions both in axial and tangential directions by means of pressure and tangential velocity jumps. The computation of these loads can be achieved by using the Blade Element Analysis Tool (BEAT), a developed rotor code based on the blade element theory. In addition, since it is considered that changes in blade motion about the feathering bearing and flapping hinge induce variations in the aerodynamic loads acting on the blades and vice versa, the loads need to be calculated under trimmed or equilibrium conditions.

The coupling between BEAT and the TAU actuator disk is defined in a way that the velocity captured at the grid points of the actuator disk surface after each simulation performed in TAU is transferred to BEAT, which computes an updated aerodynamic load distribution. The performance of this approach is tested for an isolated rotor configuration in hovering and forward flight conditions. In hovering flight, the convergence of the CFD flow simulations towards the steady state solution is not satisfactory due to the stiffness of the compressible Navier-Stokes equations at low Mach numbers. Furthermore, reverse flow regions are determined by TAU at the inner and outer boundaries of the actuator disk. The recirculation flow entails high gradients in angle of attack between neighboring blade sectional elements, which yields to the unstable formation of new reverse flow regions. Nevertheless, in forward flight conditions the performance of the flow solver is robust and convergent solutions can be obtained. Moreover, as the flight speed is increased, the shed vorticity is displaced more quickly outside the rotor disk and, hence, its associated effects on the performance of the rotor are diminished.

The accuracy of the coupling approach is validated by comparing the computed results with those measured in a wind tunnel test campaign. The found differences in pitch control angles are assigned to the fact that the blade elastic deformations are neglected in the developed method. This statement constitutes the baseline to be developed for future work.

Finally, the reduction in computation time required by the coupling approach with respect to other more accurate methods enhances the idea of further developments. Therefore, the developed method can be regarded as a suitable strategy to tackle the problem in forward flight conditions in cases where high fidelity results are not needed, such as in the preliminary design stages.

CONTENTS

Preface	iii
Summary	v
List of Figures	ix
List of Tables	xiii
Nomenclature	xv
1 Introduction	1
1.1 Problem statement	1
1.2 Objective	1
1.3 Overview	2
2 State of the art	3
2.1 Historical review of rotor theories	3
2.1.1 Momentum theory	3
2.1.2 Blade element theory.	4
2.1.3 Vortex theory.	5
2.2 Rotor modeling	5
2.2.1 CFD simulations	5
2.2.2 Wake models.	6
2.2.3 Actuator disk approach	6
2.3 Helicopter rotor simulations at DLR	9
2.3.1 CFD	9
2.3.2 Panel methods.	10
2.4 Overview	11
3 BEAT: Blade Element Analysis Tool	13
3.1 User-defined input data	14
3.2 Rotor aerodynamics.	16
3.2.1 Velocity field	16
3.2.2 Blade element analysis.	19
3.2.3 Airfoil polars	22
3.3 Rotor aeromechanics	23
3.3.1 Rotor trim	25
3.3.2 Blade flapping motion	26
3.4 BEAT structure overview	30
4 Analysis of the results and verification of BEAT	33
4.1 Reference helicopter rotor	33
4.2 Hover	35
4.2.1 Effect of the input variables	35

4.2.2	Comparison with HOST results	38
4.3	Forward flight	40
4.3.1	Effect of the input variables	41
4.3.2	Comparison with HOST results	42
4.4	Analysis overview	46
5	The CFD flow solver TAU	49
5.1	Spatial discretization	49
5.2	Partitioning/Parallelization	50
5.3	Chimera method	51
5.4	Flow solver	52
5.5	Multigrid methods	54
5.6	Boundary conditions	55
5.7	Actuator disk module	56
5.8	Overview	57
6	Coupling between BEAT and TAU	59
6.1	Coupling definition	59
6.2	Grid	62
6.3	Simulation set up	62
6.4	Analysis of results	63
6.4.1	Hover	63
6.4.2	Forward flight	68
6.5	Coupling overview	71
7	Validation of the coupling	73
7.1	HART II test	73
7.1.1	Wind tunnel facility	73
7.1.2	Rotor model and test rig	74
7.1.3	Rotor trim	75
7.2	Grid	76
7.3	Simulation set up	77
7.4	Analysis of the results	77
7.4.1	Effect of fuselage	77
7.4.2	Comparison with experimental results	79
7.4.3	Comparison with other approaches	82
7.5	Analysis overview	83
8	Conclusions and Recommendations	85
8.1	Conclusions	85
8.2	Recommendations	86
A	Axial load distribution in forward flight conditions	89
A.1	Low speed forward flight ($v_h=20$ m/s)	89
A.2	High speed forward flight ($v_h=66.7$ m/s)	90
	Bibliography	93

LIST OF FIGURES

2.1	Actuator disk implementation into a numerical solver	9
(a)	Boundary condition formulation	9
(b)	Source formulation	9
2.2	Different helicopter rotor modeling approaches depending on their associated fidelity and computational cost [52, 54]	12
3.1	Rotor hub with hinges for pitching, flapping and lagging [55]	14
3.2	Rotor disk local reference system	17
3.3	Blade local reference system	19
3.4	Aerodynamic forces acting on a blade section	21
3.5	OA213 airfoil aerodynamic coefficients	22
(a)	Lift coefficient	22
(b)	Drag coefficient	22
3.6	Interpolation scheme used to determine the airfoil aerodynamic coefficients	23
3.7	Basic helicopter control system[60]	24
3.8	Flapping hinge equilibrium	27
3.9	Blade flapping motion algorithm	30
3.10	BEAT structure scheme	31
4.1	Bo 105 helicopter	34
(a)	DLR research Bo 105. Source: DLR	34
(b)	Bo 105 main rotor hub. Source: American Helicopter Society (AHS)	34
4.2	Effect of the radial discretization in hover	36
(a)	Collective pitch control	36
(b)	Flap angle	36
4.3	Effect of the rotor radius on the collective pitch control	36
4.4	Effect of the helicopter mass on the adjusted collective control	37
4.5	Effect of the blade mass on the flap angle	37
4.6	Effect of the shaft rotational speed on the collective pitch control and flap angle	38
4.7	Aerodynamic load distribution in hover	39
(a)	Tangential aerodynamic load along the blade radius	39
(b)	Axial aerodynamic load along the blade radius	39
4.8	Aerodynamic load distribution in hover	40
(a)	Tangential aerodynamic load along the blade radius	40
(b)	Axial aerodynamic load along the blade radius	40
4.9	Effect of the spatial discretization in forward flight ($v_h = 40 \text{ m/s}$)	41
(a)	Effect of the radial discretization for $n_a = 100$	41
(b)	Effect of the azimuthal discretization for $n_r = 25$	41
4.10	Pitch control angles for different flight velocities	42

4.11 Comparison of the blade flapping distribution computed by BEAT and HOST	43
(a) Forward flight velocity $v_h = 20 \text{ m/s}$	43
(b) Forward flight velocity $v_h = 40 \text{ m/s}$	43
(c) Forward flight velocity $v_h = 66.7 \text{ m/s}$	43
4.12 Comparison of the aerodynamic load distribution computed by BEAT and HOST for $v_h = 20 \text{ m/s}$	44
(a) Tangential aerodynamic load distribution $f_{y_b}/dr \text{ (N/m)}$ computed by BEAT	44
(b) Tangential aerodynamic load distribution $f_{y_b}/dr \text{ (N/m)}$ computed by HOST	44
(c) Axial aerodynamic load distribution $f_{z_b}/dr \text{ (N/m)}$ computed by BEAT	44
(d) Axial aerodynamic load distribution $f_{z_b}/dr \text{ (N/m)}$ computed by HOST	44
4.13 Comparison of the aerodynamic load distribution computed by BEAT and HOST for $v_h = 40 \text{ m/s}$	45
(a) Tangential aerodynamic load distribution $f_{y_b}/dr \text{ (N/m)}$ computed by BEAT	45
(b) Tangential aerodynamic load distribution $f_{y_b}/dr \text{ (N/m)}$ computed by HOST	45
(c) Axial aerodynamic load distribution $f_{z_b}/dr \text{ (N/m)}$ computed by BEAT	45
(d) Axial aerodynamic load distribution $f_{z_b}/dr \text{ (N/m)}$ computed by HOST	45
4.14 Comparison of the aerodynamic load distribution computed by BEAT and HOST for $v_h = 66.7 \text{ m/s}$	46
(a) Tangential aerodynamic load distribution $f_{y_b}/dr \text{ (N/m)}$ computed by BEAT	46
(b) Tangential aerodynamic load distribution $f_{y_b}/dr \text{ (N/m)}$ computed by HOST	46
(c) Axial aerodynamic load distribution $f_{z_b}/dr \text{ (N/m)}$ computed by BEAT	46
(d) Axial aerodynamic load distribution $f_{z_b}/dr \text{ (N/m)}$ computed by HOST	46
5.1 Primary and secondary grids about a NACA 0012 airfoil [70]	50
5.2 Chimera technique scheme	53
(a) Grid generation	53
(b) Hole cutting	53
5.3 Multigrid cycles implemented in TAU	54
5.4 V-cycle scheme	55
5.5 Grid section through the disk [79]	56
5.6 Force distribution over the actuator disk [80]	57
6.1 Coupling diagram	60
6.2 Rotor disk discretization	61
6.3 Convergence history of the density residual and mass flow rate through the actuator disk for the first hovering flight simulation	64
6.4 Velocity field about the actuator disk in hover computed at the first coupling cycle	65
6.5 Comparison of the initial and first coupling cycle axial velocity and load distributions about the actuator disk in hover	65
(a) Axial velocity distribution	65

(b)	Axial aerodynamic load distribution	65
6.6	Comparison of the axial velocity and load distributions about the actuator disk in hover along the coupling cycles	66
(a)	Axial velocity distribution	66
(b)	Axial aerodynamic load distribution	66
6.7	Comparison of the shed vorticity pattern about the actuator disk in hover	66
(a)	First coupling cycle	66
(b)	Twenty-fourth coupling cycle	66
6.8	Computed collective control angle at different coupling cycles for hovering flight	67
6.9	Streamlines for hovering and axial flight conditions [26]	67
(a)	Hover	67
(b)	Axial flight	67
6.10	Convergence history of the density residual and mass flow rate through the actuator disk for the first forward flight simulation	68
(a)	Low speed flight ($v_h = 20 \text{ m/s}$)	68
(b)	High speed flight ($v_h = 66.7 \text{ m/s}$)	68
6.11	Aerodynamic axial load distribution for low speed forward flight conditions ($v_h = 20 \text{ m/s}$)	69
(a)	Initial axial load distribution computed by BEAT	69
(b)	Axial load distribution computed by BEAT after 10 coupling cycles	69
6.12	Aerodynamic axial load distribution for high speed forward flight conditions ($v_h = 66.7 \text{ m/s}$)	69
(a)	Initial axial load distribution computed by BEAT	69
(b)	Axial load distribution computed by BEAT after 10 coupling cycles	69
6.13	Comparison of the the shed vorticity pattern about the actuator disk in forward flight after 10 coupling cycles	70
(a)	Low speed flight ($v_h = 20 \text{ m/s}$)	70
(b)	High speed flight ($v_h = 66.7 \text{ m/s}$)	70
6.14	Vorticity pattern about a Bo 105 during a swinging maneuver [83]	70
6.15	Computed pitch control angles at different coupling cycles for foward flight conditions	71
(a)	Low speed flight ($v_h = 20 \text{ m/s}$)	71
(b)	High speed flight ($v_h = 66.7 \text{ m/s}$)	71
7.1	Large Low-speed Facility of the DNW [84]	74
7.2	HART II test configuration [84]	75
7.3	HART II grid structure	76
7.4	Computed pitch control angles at different coupling cycles with and without a fuselage underneath the rotor	78
(a)	Collective	78
(b)	Lateral cyclic control	78
(c)	Longitudinal cyclic control	78
7.5	Fuselage-rotor interference	78
7.6	Axial velocity distribution over the actuator disk surface computed at the first coupling cycle	79
(a)	Isolated rotor	79

(b) Fuselage and rotor	79
7.7 Measured blade torsional deformations of the HART II rotor [84, 85]	80
7.8 Comparison between the computed and the measured blade pitch angle distribution at $r/R = 0.725$	81
7.9 Recommended scheme for a future coupling version	81
A.1 Initial axial load distribution computed by BEAT ($v_h = 20 \text{ m/s}$)	89
A.2 Axial load distribution computed by BEAT after 3 coupling cycles ($v_h = 20 \text{ m/s}$)	89
A.3 Axial load distribution computed by BEAT after 6 coupling cycles ($v_h = 20 \text{ m/s}$)	90
A.4 Axial load distribution computed by BEAT after 8 coupling cycles ($v_h = 20 \text{ m/s}$)	90
A.5 Axial load distribution computed by BEAT after 10 coupling cycles ($v_h = 20 \text{ m/s}$)	90
A.6 Initial axial load distribution computed by BEAT ($v_h = 66.7 \text{ m/s}$)	90
A.7 Axial load distribution computed by BEAT after 3 coupling cycles ($v_h = 66.7 \text{ m/s}$)	90
A.8 Axial load distribution computed by BEAT after 6 coupling cycles ($v_h = 66.7 \text{ m/s}$)	91
A.9 Axial load distribution computed by BEAT after 8 coupling cycles ($v_h = 66.7 \text{ m/s}$)	91
A.10 Axial load distribution computed by BEAT after 10 coupling cycles ($v_h = 66.7 \text{ m/s}$)	91

LIST OF TABLES

2.1	Characteristics of different rotor analysis approaches. [53]	11
3.1	Geometry modeling input data	15
3.2	Flight conditions input data	15
3.3	Ambient conditions input data	15
3.4	Analysis set-up input data	16
4.1	Rotor blade geometric data	34
4.2	Pitch control inputs and flap angle at hovering flight	38
4.3	Pitch control inputs and flap angle at hovering flight considering the same axial induced velocity $v_i = 11.4 \text{ m/s}$	40
4.4	Comparison of the pitch control angles computed by BEAT and HOST	42
6.1	Aerodynamic loads prescription output file	62
6.2	Grid characteristics	62
7.1	Wind tunnel flow data	74
7.2	Control inputs of the baseline case	76
7.3	Grid characteristics	76
7.4	Computed pitch controls after 8 coupling cycles with and without a fuselage underneath the rotor	77
7.5	Rotor control angles of the HART II baseline case	80
7.6	Trim controls computed by different approaches for the HART II baseline case	82
7.7	CPU time required by the CFD solver to perform the first coupling cycle simulation	83

NOMENCLATURE

List of symbols

α	Angle of attack
α_s	Shaft angle
β	Flap angle
χ	Wake skew angle
η	Perturbation in control inputs
γ	Heat capacity ratio
ϕ	Relative inflow angle
ψ	Azimuth angle
ρ	Density
θ	Pitch angle
θ_0	Collective pitch control
θ_{1c}	Lateral cyclic control
θ_{1s}	Longitudinal cyclic control
θ_{def}	Torsional deformation
θ_r	Blade twist at the root
θ_{tw}	Linear blade twist rate
ε	Tolerance
Ω	Rotational speed
A	Rotor area
a	Speed of sound
c	Rotor blade chord
c_d	Airfoil drag coefficient
c_l	Airfoil lift coefficient

c_{PM}	Pitching moment coefficient
c_{RM}	Rolling moment coefficient
c_T	Thrust coefficient
D	Drag
e	Flapping hinge offset
F	Fluxes through a control volume
f	Blade load
F_T	Tangential load component
g	Gravitational acceleration
I_β	Blade moment of inertia about the flapping hinge
J	Jacobian
L	Lift
M	Mach number
M_β	Moment about the flapping hinge
m_b	Blade mass
m_h	Helicopter mass
n_a	Number of azimuthal stations
n_r	Number of radial stations
p	pressure
R	Blade radius
r	Radial location
r_p	Start of the profiled part
S	Area
T	Thrust force
t	time
T_∞	Air temperature
U_P	Axial velocity component
U_T	Tangential velocity component

v	Velocity
v_a	Helicopter axial velocity
V_c	Control volume
v_h	Helicopter forward velocity
v_i	Induced velocity
W	Weight
X	Control variable
Y	Response variable

Additional subscripts

∞	Freestream
b	Blade reference system
CF	Centrifugal force contribution
com	Computed value
d	Rotor disk reference system
exp	Experimental value
I	Inertia contribution
i	Inner
o	outer
R	Resultant
T	Aerodynamic contribution
W	Gravitational contribution
x	Along the x-axis
y	Along the y-axis
z	Along the z-axis

Abbreviations

AD	Actuator Disk
$BEAT$	Blade Element Analysis Tool
BET	Blade Element Theory

BOS Background-Oriented Schlieren
CFD Computational Fluid Dynamics
CFL Courant-Friedrichs-Lewy
DLR German Aerospace Center
DNW German-Dutch Wind Tunnels
HART Higher harmonic control Aeroacoustic Rotor Test
HHC Higher Harmonic Control
HOST Helicopter Overall Simulation Tool
LAPACK Linear Algebra Package
LLF Large Low-speed Facility
MPI Message Passing Interface
ONERA French Aerospace Lab
PIV Particle Image Velocimetry
RANS Reynolds Averaged Navier-Stokes
UPM Unsteady Panel Method

1

INTRODUCTION

1.1. PROBLEM STATEMENT

The rotor plays a key role in the performance of helicopters and must be analyzed thoroughly along its design stages. Its aerodynamic contribution not only is related to the lift force created to compensate the weight of the helicopter but also to the required propulsion force to maneuver. The flow field which goes through the rotor is subjected to reaction forces along the blades which produce variations in its pattern both in direction and intensity. Thus, the flow under the influence of the rotating blades is characterized by its complexity and unsteadiness. A suitable prediction of the flow field about the rotor is essential to determine its effects on the fuselage and empennage as well as to determine its associated power requirements.

A complete simulation of the flow by means of CFD requires the use of overset grids around the geometry of the blades where the Navier-Stokes equations are applied numerically. Nonetheless, despite the high fidelity results that can be obtained, CFD simulations entail considerable computational expenses and the use of alternative simplified models for addressing the problem has been extended. One of these approaches consists of replacing the rotor by a zero thickness surface or actuator disk, where the need of modeling the individual blades with a body-fitted mesh is avoided. In addition, it enables the computation of the slipstream as a time-averaged solution, which gives an overview of the actual wake pattern. The unstructured CFD solver TAU developed at DLR includes among its tools a module based on the actuator disk principles. Nevertheless, this module requires the input of the aerodynamic loads acting on the actuator disk surface.

1.2. OBJECTIVE

The objective of the present project is the development of BEAT, a rotor analysis code that enables the computation of the rotor aerodynamic loads according to the blade element theory and that can be coupled with the actuator disk module implemented in TAU. This coupling involves an iterative process in which the flow velocities computed by TAU are used to calculate the blade loads that are subsequently transferred to the flow solver. By carrying out this feedback process until convergence is reached, the performance of a helicopter rotor both in hover and forward flight can be analyzed. Due to the assumptions related to the actuator disk approach and blade element theory, the accuracy of the com-

puted results is expected to be lower than for high fidelity CFD methods where the flow around each blade is simulated. On the other hand, the required computation time is foreseen to be reduced.

Since the initialization of the aforementioned coupling process needs the input of both the axial and tangential aerodynamic load distributions, BEAT enables their computation by either the use of static inflow models or the prescription of the velocity field over the rotor disk. Blade pitching and flapping degrees of freedom are considered while blade lagging and elastic deformation effects are not taken into account. The pitch control angles are adjusted in order to reach trimmed steady flight conditions whereas the flapping angle distribution is obtained by imposing equilibrium of moments about the flapping hinge.

Hereby, it can be stated that the aim of the thesis is the:

Development of a blade element method for CFD simulations of helicopter rotors using the actuator disk approach

The achievement of this purpose is subjected to the completion of three phases: development and verification of BEAT, coupling with TAU, and testing and validation. In addition, the proposed research questions can be formulated by:

- Can the coupling between BEAT and TAU be regarded as a feasible approach, in terms of convergence and stability, for the analysis of helicopter rotors in hovering and forward flight conditions?
- How does the made assumptions affect the accuracy of the obtained results?

1.3. OVERVIEW

A review of the existing methods used for the aerodynamic modeling of helicopter rotors is presented in Chapter 2. Subsequently, in Chapter 3 a description of both the structure and the basic theory behind BEAT is given. Chapter 4 addresses the analysis of the results computed by the rotor analysis tool and its verification. An overview of the CFD solver TAU with particular emphasis on the main functionalities employed during its coupling with BEAT is given in Chapter 5. The definition of the coupling approach and the analysis of the obtained results for isolated rotors in hovering and forward flight conditions is presented in Chapter 6. The evaluation of the accuracy of this method is covered in Chapter 7, where the obtained results are compared with those measured in a wind tunnel campaign. In addition, in this chapter, the advantages and limitations of the developed coupling approach with respect to other methods currently used at the DLR are assessed. Finally, the conclusion and recommendations for future work are drawn in Chapter 8.

2

STATE OF THE ART

This chapter addresses different approaches that can be followed for the aerodynamic modeling of helicopter rotors. Firstly, in section 2.1, a historical review of the development of rotor theories is presented. Then, different modeling methods are detailed in section 2.2, while in section 2.3 the tools used at DLR for analyzing the flow field subjected to the presence of a rotor are explained.

2.1. HISTORICAL REVIEW OF ROTOR THEORIES

The complexity associated with the analysis of the flow pattern about helicopter rotors can be reduced by means of the application of classical rotor theories, which were initially developed for propeller applications. The level of simplification related to each theory depends on the assumptions taken into account. The simplest approach for rotor modeling is the momentum theory, where the rotor is replaced by a zero-thickness surface uniformly loaded. Blade element theory accounts for blade geometry by dividing each blade into sectional elements where a two-dimensional aerodynamic analysis is carried out. Three-dimensional effects are taken into consideration by vortex theories, in which the rotor blades are represented by a bound vortex system. In this section, a review of the development of the three rotor theories is conducted.

2.1.1. MOMENTUM THEORY

The first steps taken towards the development of the momentum theory dates back to the second half of the nineteenth century. This first research stage was focused mainly on the analysis of ship propellers. Nevertheless, the principles of the momentum theory were later applied to any propeller. The foundations of the model are attributed to the work of Rankine and Froude.

In 1865, Rankine [1] advocated the idea that the action of the propeller was responsible for causing a change in pressure and an increase in flow velocity. Moreover, he modeled the flow through a propeller as a streamtube whose cross-sectional area immediately behind the propeller was very nearly or exactly equal to the area covered by it. As a consequence of the flow velocity increase provided by the rotor, the streamtube was narrowed along the slipstream and, thus, the effect of the flow acceleration was balanced.

Two decades later, Froude [2] introduced a new concept to analyze the performance of propellers. The propeller was replaced by a thin plate of finite area and same diameter,

where the flow which went through it dealt with a pressure discontinuity. Froude termed this surface of change of pressure as “actuator”. Furthermore, he stated that the acceleration imposed to the flow took place both in front and behind the propeller and in each region the increase in velocity was exactly the same, which meant that half of the acceleration was carried out before and the other half was carried out after the propeller.

According to the historical review of the momentum theories of van Kuik et al. [3], at the beginning of the twentieth century the theory developed by Froude was not totally accepted among the scientific community of that period. The main reason of disagreement was the lack of evidence which supported any connection of the actuator surface and the effects of the propeller blades on the studied flow. However, Froude’s theory was finally validated with the development of the vortex theory for rotors.

In 1935, Glauert [4] compiled the basis of the axial momentum theory, which considered that no rotational motion was communicated to the flow. The aforementioned theory was extended by means of including the contribution of the rotational velocity component in the so called “general momentum theory”. One of the assumptions on which the general momentum theory was founded was the consideration of irrotational motion in the slipstream except along the rotor axis. On the other hand, Glauert pointed that the main defect of the momentum theory was that it did not provide any clue of the required geometry of the propeller to present the obtained performance features.

2.1.2. BLADE ELEMENT THEORY

In contrast to the momentum theory, the geometry of the blade was taken into account by the blade element theory and it plays a fundamental role in its functioning. The starting point of the blade element theory is associated with the work presented by Froude in 1878 [5]. In this text, Froude analyzed a sectional element of a ship propeller blade. To do so, the sectional element was determined by the intersection of the propeller blade and a moving plane, which was carried round the propeller axis and was set obliquely to the plane of rotation.

In 1892, Drzewiecki [6] went into detail about the idea proposed by Froude. Thus, the blade of a propeller was divided into finite elements along its radius. Each element could be analysed separately by considering two existing velocity components. The axial velocity component was associated with the propeller velocity of translation, while the tangential velocity was a result of the rotation of the propeller. Therefore, by taking into account both components, the resultant velocity could be determined as well as the forces acting on each element that were subsequently integrated along the blade radius.

However, as it is indicated by Okulov et al. [7] and Johnson [8], the approach defended by Drzewiecki presented a significant problem due to the fact that it disregarded the influence of the rotor over the flow. Drzewiecki maintained the idea of the lack of relation between the axial velocity determined by the momentum theory and the axial velocity taken into account in his approach.

In 1919, de Bothezat [9] combined the theory developed by Drzewiecki with the momentum theory. The velocity increase determined by the momentum theory, both the axial and rotational components, were added to the contribution of the propeller velocity of translation and the tangential velocity of the propeller respectively. The relative velocity of the fluid in regard to the considered blade element could be computed by taking into account the aforementioned components.

2.1.3. VORTEX THEORY

The principles of vortex theory for propellers as well as helicopter rotors are based on the foundations of the aerodynamic theory for lifting surfaces proposed by Prandtl in 1918 [10]. The existence of vortices was admitted to address the problem of the motion of inviscid flow about a fixed span lifting surface. Prandtl replaced the lifting surface by a bound vortex system, which in a simplified form, could be regarded as a bound vortex line. Along the bound vortex system, trailing vortices were considered to be continuously shed. It was stated that vortex shedding entailed velocity induction over the lifting surface which could be computed by applying the Biot-Savart law.

Goldstein in 1929 [11], developed a method for the analysis of the vortex system about propellers with a finite number of blades. Taking into consideration that due to the trailing vortices part of the supplied work was lost, he computed the circulation along the propeller blades for maximum efficiency.

2.2. ROTOR MODELING

During the last decades researchers have developed several methods to handle the computation of the flow pattern under the influence of the rotating blades of the helicopter rotor. The accurate modeling of the physics behind the problem addressed by CFD simulations is associated with high computational expenses. The complexity of the study can be reduced by means of simplified methods such as wake models and the actuator disk approach.

2.2.1. CFD SIMULATIONS

In order to simulate the flow through the rotor and its wake, CFD codes discretize the domain. By means of computational grids about the helicopter geometry, the aerodynamic differential equations are applied to reach numerical solutions. Nevertheless, the rotational motion of the blades entails complex grid geometries and modeling. Chimera technique or overset grid method, described by Benek [12], is the most extended approach to handle effectively full rotor computations. It is based on the division of the physical domain into zones where local grids are generated. Hence, the computational domain can be decomposed into two regions. One region is associated with the rotor, the grid contained there models the blade geometry while it also rotates as the rotor does. On the other hand, the second region models the rest of the airframe with a stationary grid configuration. Between both regions an overlap zone is required in order to establish connectivity among the rotating and stationary grids. Thus, three dimensional interpolation of information is carried out at the overlapping region at each time step enabling a correct coupling between the numerical solution at the boundaries of each sub-domain. However, as it is pointed by Chaffin and Berry [13], the complexity associated with the information exchange by the overset interpolation can be a considerable source of numerical problems.

Chimera technique was used by Hariharan et al. [14] to compute the three-dimensional compressible unsteady flow around a rotor by solving the Reynolds Averaged Navier-Stokes (RANS) equations. Navier-Stokes equations in combination with overset grids were also computed for the flow field about a complete tiltrotor aircraft at low speed forward flight conditions by Meakin [15] and for helicopter rotors in hovering flight conditions by Pomin and Wagner [16] and Yang [17]. The viscous terms present in the Navier-Stokes equations are accountable for effects such as flow separation which typically occurs along retreating

blades in forward flight. Nevertheless, the assumption of inviscid flow about the rotor reduces considerably the computational expenses of each simulation. Park and Kwon [18] followed this approach by developing an Euler flow solver for the simulation of the unsteady inviscid flow field around the rotor blades.

2.2.2. WAKE MODELS

Classical vortex theories defend the idea that the rotor wake can be modeled as a rigid non-contracting helical vortex sheet. Jenney et al. [19] compared the predicted wake pattern by vortex theory with representative full scale test data for hovering flight conditions. Several discrepancies were found and were assigned as the main cause of the inadequacies associated with the conventional vortex methods. Wake contraction close to the helicopter rotor was highlighted as the main responsible for these discrepancies. In order to reduce the wake inconsistencies, rotor wake models were developed. According to Miller [20], wake models can be divided into two groups: prescribed wake models and free wake models. Wang et al. [21] have recently compiled the most relevant literature about the advance of both methods.

Prescribed wake models allow the vortex structure modeling of the wake in terms of location, strength, and size by using experimental observation results of the flow pattern. Landgrebe [22] developed a prescribed wake model for hovering rotors. The fundamental characteristics of his model were extracted from the interpretation of the three-dimensional wake pattern observed by carrying out smoke experiments through rotating blades. Beddoes [23] introduced an approach based on the idea that an adequate definition of the wake was a prerequisite for load calculations along the rotor blades. For a proper modelling, the most critical points in the wake were identified and their influence was analyzed. Having calculated the distorted flow pattern of the wake, the induced velocities were computed by applying the Biot-Savart law. The main drawback of prescribed wake models is their low flexibility. Empirical relations from experimental data are required for their application, hence, their use is restricted to similar geometries and flight conditions to those already measured.

Free wake models offer more flexible features than prescribed wake models. Their application is based on the wake discretization with a vortex structure subjected to the Navier-Stokes equations. The vortices are allowed to follow force-free paths under the assumptions of potential flow. Leisham et al. [24] discussed the numerical methods used to solve the vortex convection through the wake. Viscous contribution was pointed as a critical factor for accurate predictions of the vortex structure, concluding that research was required to integrate rigorously the wake pattern and viscous effects.

2.2.3. ACTUATOR DISK APPROACH

TIME-AVERAGED SOLUTION

An accurate modeling of the flow about the helicopter rotor blades requires instationary calculations and entails high computational effort. The actuator disk approach aims to reduce the complexity associated with the flow computation by assuming that the loads act on a surface instead of along each blade. The need of modelling the individual blades with a body-fitted grid is avoided, reducing the grid size. Moreover, no assumptions of wake patterns are required and the computed slipstream is a time-averaged solution, which despite not representing the flow unsteadiness, it gives an overview of the actual wake pattern.

Fejtek and Roberts [25] applied the actuator disk approach to analyze the wing/rotor interaction of a tiltrotor in hover, the blade loads were averaged over each cell of the discretized actuator disk which imparted a variation of pressure and swirl along both the azimuthal and radial directions. An isolated rotor configuration was analyzed by running CFD flow simulations about an actuator disk whose aerodynamic load distribution was computed by means of the blade element theory. A flow recirculation area was determined at the outer edge of the rotor disk, which entailed an increase in both the angle of attack and the lift coefficient at the rotor tip. Giovanetti et al. [26] analyzed the geometry of the vortex sheet near the outer boundary of a uniform loaded actuator disk by the application of a potential flow model. They concluded that the computed axial induced velocity distribution in hovering flight was not uniform, especially at the outer boundary, where flow recirculation was captured.

Rajagopalan and Mathur [27] modeled the rotor as an actuator disk for forward flight conditions. The loads were computed according to the blade element theory for each grid cell. The quality of the results were assessed by being compared to experimental data, concluding that they matched satisfactory the expectations and underlining the versatility of the method since no assumptions about the wake structure were required. Hariharan et al. [14] in an attempt to determine the minimum level of detail needed to compute the effects of the rotor on the flow field in forward flight, compared the performance of an actuator disk uniformly loaded with the results obtained by an unsteady compressible Navier-Stokes solver using overset grids. The discrepancies between both results, showed that more accurate performance could be reached by a non-uniform load distribution along the blade span. One of the main problems of the uniform load distribution is that if the rotor hub is not introduced and slipstream rotation is considered, it entails a singular force. Conway [28] developed a method to handle the simulation of the inviscid incompressible flow through a propeller modeled as an actuator disk with non-uniform load distribution by deriving the governing equations from a vortex wake model. Chaffin and Berry [13], coupled the actuator disk approach with the blade element theory to compute the blade loads for different forward flight speeds. A trim loop was also set up to compute the pitch distribution without taking into account flapping and lagging degrees of freedom. O'Brien and Smith [29] analyzed the accuracy of the CFD results obtained from different load distributions acting on an actuator disk by being compared with experimental data for forward flight conditions. Load distributions calculated by means of blade element theory were found to perform better than any uniform or linear load distribution. In addition, vortices shed from both the tip and the root were captured. It was observed that the strength of the vortices shed at the advancing side was higher than at the retreating side due to the larger lift produced at the advancing zone. Similar findings concerning the vorticity pattern about an actuator disk in forward flight were reported by Le Chuiton [30], who coupled a CFD solver with a rotor comprehensive code based on the blade element theory. Hence, the flow about the actuator disk was simulated for prescribed aerodynamic loads.

UNSTEADY AERODYNAMIC EFFECTS

Time-averaged solutions obtained by the application of the actuator disk approach do not account for unsteady aerodynamic effects. In real conditions, the helicopter rotor performance is subjected to unsteady conditions due to gusts, turbulence, deflection of the blades or control actions. The aforementioned actuator disk methods assume that changes in aerodynamic loads along the rotor blades produce an instantaneous response of the slip-

stream pattern. Nevertheless, a time lag is associated to those changes in rotor loads until a new equilibrium state is reached. Hence, to compute the transient behavior of the slipstream, the interactions between the flow dynamics and the blade motion have to be taken into account.

The use of dynamic inflow models allows the analysis of the effects that a load change has on the rotor performance. These models introduce perturbations in the rotor disk and can be incorporated in actuator disk algorithms. Extensive reviews of the development of dynamic inflow models along the last decades were compiled by Gaonkar and Peters [31] and van Hoydonck et al. [32]. Carpenter and Fridovich [33] proposed a method for predicting the effect of a rapid pitch increase in take-off on the thrust and induced velocity response of a helicopter rotor. The momentum theory was applied to compute the transient thrust by including an “apparent additional mass term” which accounted for the inertia of the accelerated flow. Pitt and Peters [34] developed a dynamic inflow model to relate the transient aerodynamic rotor loads to the unsteady response of the induced flow field through an actuator disk for both hover and forward flight conditions. An extension of the first harmonic Pitt-Peters dynamic inflow model was carried out by Peters and He [35] for higher harmonic solutions. Peters [36] stated that every dynamic inflow model consists of a set of ordinary differential equations in time that takes the form of (2.1), where $\{v_n\}$ are states that define the flow, $[M]$ is a mass matrix, $[C]$ includes the influence coefficients, and $\{F_m\}$ accounts for the loads along the blades.

$$[M] \left\{ \frac{dv_n}{dt} \right\} + [C] \{v_n\} = \{F_m\} \quad (2.1)$$

In an attempt to replace the use of dynamic inflow models when an axial velocity field is considered, Chattot [37] presented a method to extend the actuator disk to unsteady flow by modeling the slipstream as a succession of vortex rings with a variation in strength shed at the rotor and applying conservation laws. Subsequently, Yu et al. [38] deepened the steady vortex tube model to unsteady conditions for both uniform and non-uniform disk loading. The slipstream was modeled by means of a set of semi-infinite annulus vortex tubes. The results obtained following this approach were compared with the ones computed by dynamic inflow models such as the Pitt-Peters model, concluding that the vortex tube approach showed better predictions than dynamic inflow models and it also had the advantage of computing the radial velocity component.

IMPLEMENTATION

Le Chuiton [30] and O’Brien and Smith [29] discussed two different approaches to implement the actuator disk concept into a discretized solver code depending on whether it is considered as an obstacle for the flow or not: boundary condition and source term formulation. In the boundary condition approach, the actuator disk is treated as a solid body contained outside the control volume. Thus, the rotor model is contemplated as the common surface of two or more independent grid blocks (figure 2.1a) where the fluxes at both sides are different and related by proportionality relations imposed by the boundary conditions which define the influence that the solid has over the flow field. On the other hand, in the source term approach (figure 2.1b) the actuator disk lies inside the control volume and its effect on the flow is modeled by including source terms in the conservation equations. In this case, flow values are computed as for any other inter-block connection while a force

is applied on the cell-face on the lower side of the actuator disk and in case that the compressible conservation equations are taken into account, the associated work is also included in the lower side of the surface. An extensive explanation about rotor modeling by incorporating source terms in the conservation equations was given by Rajagopalan and Kim [39].

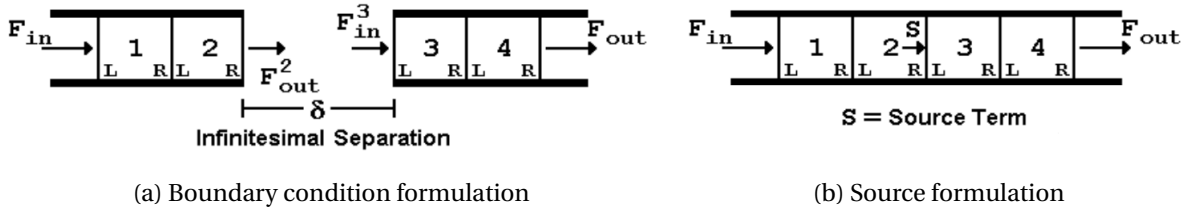


Figure 2.1: Actuator disk implementation into a numerical solver

A performance assessment of both formulations was carried out by Le Chuition [30] coming to the conclusion that source term approaches offered more robust solutions than boundary condition approaches. The source term implementation showed better convergence while fluctuations were observed in the close vicinity of the disk. It was also pointed that this distinction is flexible and both methods can be combined and share common points.

2.3. HELICOPTER ROTOR SIMULATIONS AT DLR

Simulations of the flow field subjected to the presence of a helicopter are performed at DLR following two different approaches. High quality results can be obtained by means of CFD codes while panel methods based on the potential theory allow for the calculation of lower fidelity results but at lower computational expenses than CFD methods.

2.3.1. CFD

High fidelity prediction of the flow about a rotorcraft can be computed by means of CFD methods. DLR flow solvers FLOWer [40] and TAU [41] solve the unsteady, compressible, three-dimensional Euler and RANS equations for multi-block meshes, where the Chimera technique approach for moving blades is applied. The neglected viscous effects in Euler equations are captured by RANS equations through the use of different available turbulence models. The main difference between both codes lies in the grid geometry used to discretize the domain. While FLOWer employs structured grids, TAU combines both structured and unstructured grids. The use of hybrid meshes enable TAU to resolve accurately the viscous effects at the vicinity of the walls by means of structured meshes (hexahedral elements) and to model complex geometries with unstructured grids (tetrahedral elements).

Due to their high aspect ratio and lightweight structure, rotor blades face considerable deformations and fluid-structure interactions are taken into account along the helicopter design process. Coupling between CFD codes FLOWer and TAU with comprehensive rotor simulation codes [42–44] allows to account for blade elastic deformations and to obtain trimmed solutions for the user-defined flight conditions. At DLR, two rotor simulation codes are generally used: S4 and HOST.

- DLR rotor simulation code S4 [45] performs an initial modal analysis to represent each blade by its mode shapes and natural frequencies in lead-lag, flap, and torsion. Applying the aerodynamic loads acting on each individual blade, the dynamic response of the blade modes is simulated. It includes a trim module which adjusts the collective and cyclic pitch control inputs and the rotor shaft angle of attack for the prescribed flight conditions.
- The comprehensive rotor code HOST [46] developed by Eurocopter models the blade as a quasi 1D-beam based on an extended Euler-Bernoulli formulation assuming moderate deformations in lead-lag, flap, and torsion. It features a basic aerodynamic module based on the blade element theory, which determines the aerodynamic coefficients from airfoil look-up tables for any local Mach number and angle of attack. Rotor trim is performed by means of an iterative Newton-Raphson method. On the other hand, HOST can also be used without being coupled with a CFD solver [47]. It features several inflow models, a prescribed wake model (METAR) and a free wake model (MESIR).

Due to the lack of detailed experimental data to assess the performance of CFD codes, DLR in a partnership with other European aerospace institutions has carried out in the last years wind tunnel test campaigns such as the HART II program [48] and the GOAHEAD project [49]. The objective of these projects was the creation of a experimental database for complete helicopter configurations by performing wind tunnel experiments for scaled models of generic helicopters. The generated results are used for the validation of unsteady viscous flow simulations of CFD solvers.

2.3.2. PANEL METHODS

UPM is a three-dimensional unsteady panel and free wake code developed at DLR [50, 51] based on the potential flow theory, which assumes incompressible, inviscid and irrotational flow. It enables the prediction of the unsteady loads and the wake interaction effects around helicopter rotors in arbitrary motion with theoretically less computational expenses than CFD methods. The domain is discretized by dividing the blades and wake into finite area surface elements (panels) and flow tangency condition is imposed at the control or collocation points of each panel. The rotor blades are modeled with a source/sink distribution to account for blade thickness and a prescribed weight function for the vortex strength along the chord to simulate the blade lift. In order to satisfy the Kutta condition, which maintains that the flow does not experience any velocity singularity at sharp trailing edges, a zero thickness elongation (about 2% of the local blade chord) of the trailing edge is modeled. The orientation of this elongation (Kutta panel) determines the direction of the shed vortex filaments. On the other hand, non-lifting bodies are modeled so as to only the displacement effect produced on the flow is taken into account while their lift and drag contribution is neglected.

Effects of flow compressibility are computed by means of Prandtl-Glauert correction and a Newton-Raphson procedure is included for rotor trimming. In addition, the coupling with S4 or HOST is possible [52] and enables the analysis of elastic blade deformation effects.

2.4. OVERVIEW

The aerodynamic modeling of helicopter rotors can be carried out by means of different approaches whose accuracy level and required computational cost (figure 2.2) depend on their associated assumptions (table 2.1). The blade element theory is regarded as a low-fidelity approach that is usually used during the initial stages in the rotor design process. The velocity that the rotor induces to the flow which goes through it can be accounted by means of the use of static inflow models based on the actuator disk approach. On the other hand, unsteady aerodynamic effects can be addressed by the application of dynamic inflow models. The two-dimensional aerodynamic coefficients of each blade sectional element are extracted from airfoil look-up tables where the effects of viscosity and compressibility are contained. Nevertheless, flow three-dimensional effects such as blade-vortex interaction effects can only be partially captured by means of correction factors. Panel methods enable the determination of these effects by either prescribing (prescribed wake models) or allowing the vortices to follow force-free paths (free wake models) along the rotor wake under the assumption of potential flow. High accurate solutions can be reached by CFD flow simulations which capture the unsteady three-dimensional pattern of the flow as well as the compressibility effects. The flow governing equations can be applied by either neglecting (Euler equations) or accounting for the viscous contribution (RANS).

Method	Advantages	Disadvantages
1. CFD	-Accurate flow solution -Unsteady effects -Compressibility effects -Three dimensional solution	-High computational cost -Numerical errors can arise from the use of overset grids
RANS	-Viscous effects	-More expensive than Euler methods
Euler	-Cheaper than RANS	-Inviscid flow solution
2. Wake models	-Unsteady effects -Compressible flow (correction factors)	-Inviscid flow solution
Free wake	-Good wake modeling -More flexible modeling than prescribed wake methods	-More complex and less stable than prescribed wake methods
Prescribed wake	-High stability	-Low flexibility -Reference data is required
3. Actuator Disk	-Simple approach -Low computational cost -Individual modeling of the blades is not required	-Viscosity and compressibility effects are contained in look-up tables -Time-averaged solution (unsteady effects can be included by means of dynamic inflow models)

Table 2.1: Characteristics of different rotor analysis approaches. [53]

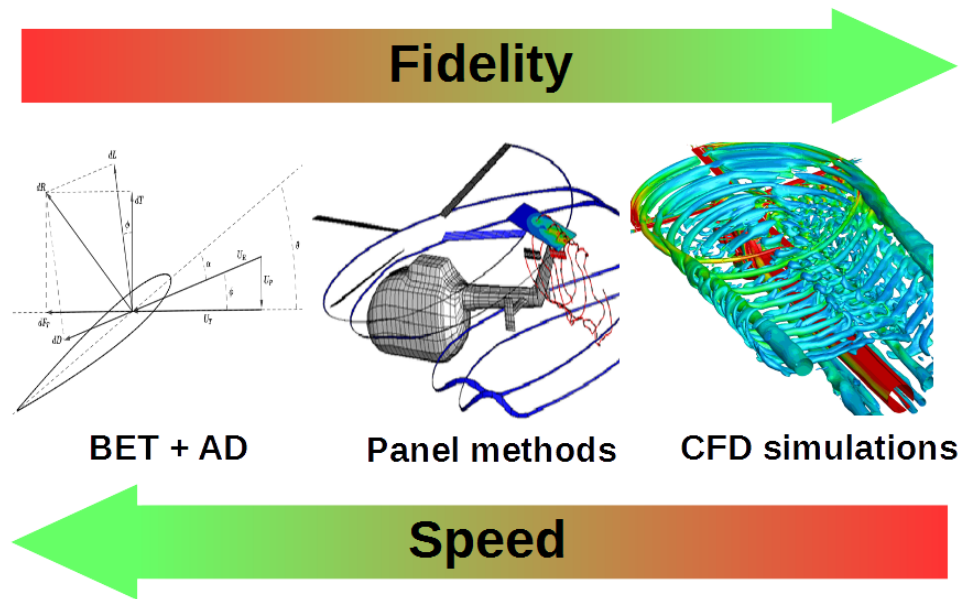


Figure 2.2: Different helicopter rotor modeling approaches depending on their associated fidelity and computational cost [52, 54]

3

BEAT: BLADE ELEMENT ANALYSIS TOOL

This chapter offers a description of both the structure and the basic theory behind BEAT, a tool which has been developed to compute the aerodynamic loads that act along the span of helicopter blades under either hover or forward flight conditions. This code entails the application and combination of two rotor theories: momentum and blade element theory. The calculation of the aerodynamic loads is carried out for a given velocity field over an actuator disk which models the helicopter rotor. BEAT enables the user to choose between two possible ways to obtain the velocity pattern through the rotor disk. It can be directly computed by taking into account the velocity components associated with the defined flight condition and implementing a static inflow model to account for the rotor induced velocities or it can be extracted by coupling BEAT with the actuator disk module included in the CFD solver TAU (section 5.7). This actuator disk module is based on the assumptions made by the momentum theory, which considers that the helicopter rotor can be modeled as a circular surface of zero thickness called actuator disk which imposes pressure and tangential velocity discontinuities to the flow which goes through it. The representation of the rotor as a surface is equivalent to suppose an infinite number of blades. On the other hand, the aerodynamic loads are computed by BEAT by means of the blade element theory. To do that, the blade is divided into sectional elements along its radius which are modeled as two-dimensional airfoils, totally independent of the analogous sectional elements, which means that interaction effects among them are neglected and each element can be examined separately. Since the problem is reduced to the aerodynamic analysis at the plane defined by each blade element, the flow velocity relative to the sectional element is determined by axial and tangential velocity components, while the influence of radial velocity along the blade is disregarded.

One key aspect in rotor analysis that is taken into consideration is the coupling of the blade motion with the aerodynamic load acting on it. Changes in the load distribution along the blades modify its trajectory and vice versa. Generally, the blade motion is defined by three degrees of freedom: pitching or feathering, flapping and leading-lagging as it is shown in figure 3.1. Each degree of freedom is associated with an axis or hinge located at the rotor hub about which the blade can rotate. BEAT only accounts for both pitching and flapping motion, while leading-lagging displacements are neglected. Due to the latter assumption, the lead-lag hinge does not need to be modelled and the complexity associated with the analysis of the blade motion is reduced. Nevertheless, in further versions of

BEAT, the modeling of leading-lagging displacements can be taken into account as a possible improvement. In addition, other effects such as blade elastic deformations are neither considered. Blade pitching motion is determined in order to achieve trimmed steady flight conditions, while the flapping motion is obtained by imposing equilibrium of moments about the flapping hinge.

BEAT is written in FORTRAN which is a widespread programming language among the scientific community. Despite the fact that it is one of the first developed programming languages, its use has not been reduced over the last decades and it is continuously improved. In addition, the three-dimensional unsteady panel and free wake code UPM developed by the Helicopter Department at the DLR is also written in FORTRAN. Thus, the use of the same language can facilitate a future coupling between both codes.

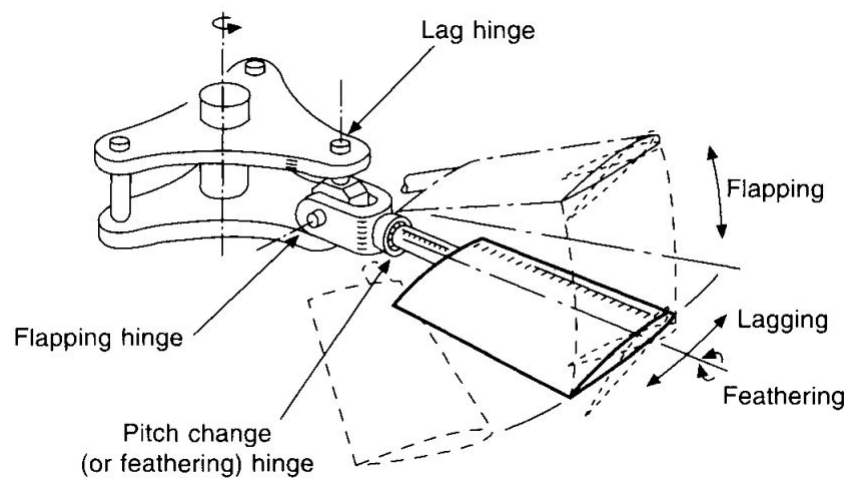


Figure 3.1: Rotor hub with hinges for pitching, flapping and lagging [55]

3.1. USER-DEFINED INPUT DATA

Before performing the rotor aerodynamic analysis certain information must be specified by the user. This data is required for the rotor modeling as well as for the definition of the flight conditions and analysis set-up. Some assumptions are made to decide the number and type of the needed inputs in such a way that the main rotor characteristics are modeled while the features whose contribution is not expected to have influence over the analysis results are disregarded in order to reduce the modeling complexity as much as possible. Hence, as a result of the differences between the model and the actual system to be modeled, BEAT, as any other rotor model is subjected to uncertainties.

The rotor is represented by N_b blades that can freely flap about a hinge radially offset from the shaft axis. The blade is an airfoil shaped body, whose section remains unaltered along the blade span and the two-dimensional aerodynamic coefficients of each cross-sectional element are extracted from a specified airfoil lookup table. The blade planform is rectangular which means that the chord length does not vary with the radius. The blades can be linearly twisted while both the sweep and anhedral angles are assumed to be zero. Uniform mass distribution along the blade span from a location r_p where the profiled part starts to the tip is considered. The blade moment of inertia does not need to be prescribed since it is computed from the blade mass distribution. The mass of the helicopter

linked to the rotor to be assessed has to be prescribed since it is required for trimming computations. The plane of rotation where the actuator disk is located is perpendicular to the rotor axis and, therefore, can be defined by the angle formed between the shaft axis and the vertical direction which is known as shaft angle α_s .

Parameter	Symbol	Units
Blade radius	R	m
Flapping hinge offset	e	m
Start of the profiled part	r_p	m
Rotor blade chord	c	m
Airfoil polar file	-	-
Number of blades	N_b	-
Blade mass	m_b	kg
Helicopter mass	m_h	kg
Linear blade twist rate	θ_{tw}	$^\circ/m$
Blade twist at $r = r_p$	θ_r	$^\circ$
Shaft angle	α_s	$^\circ$

Table 3.1: Geometry modeling input data

The inflow direction is determined by prescribing both the horizontal and axial velocity components. These two values enables the definition of hover, axial, forward, ascending and descending flight conditions. In addition, the rotational speed of the blades also has to be inputted.

Parameter	Symbol	Units
Helicopter axial velocity	v_a	m/s
Helicopter forward velocity	v_h	m/s
Rotational speed	Ω	rpm

Table 3.2: Flight conditions input data

Regarding the freestream properties, the values of both the air density and temperature have to be defined. The aerodynamic loads acting on the blade span are computed by BEAT under the incompressible flow assumption, so the prescribed density is employed for the aerodynamic analysis of any blade sectional element. Inflow temperature is also considered to be constant, which entails that the speed of sound also remains unaltered at any point of the considered domain.

Parameter	Symbol	Units
Air density	ρ_∞	kg/m^3
Temperature	T_∞	K

Table 3.3: Ambient conditions input data

The rotor disk to which the computed aerodynamic loads are projected and from which the velocities are extracted is discretized into n_r radial and n_a azimuthal stations uniformly distributed. The azimuthal discretization covers the 360° of the disk, however the radial component only represents the blade zone on which aerodynamic forces act. This zone ranges from the start of the profiled part at r_p to the blade tip at a distance R from the center of the disk. Hence, the discretized actuator disk area is equivalent to an annular surface. Regarding the velocity field to be considered for the aerodynamic loads computation, it can be directly calculated by the tool by means of the application of either a uniform or a linear static inflow model for the axial induced velocity distribution. On the other hand, the coupling between BEAT and the actuator disk module included in TAU enables the extraction of these velocities by performing CFD simulations of a rotor disk whose aerodynamic load distribution is previously computed by BEAT.

Parameter	Symbol	Units
Number of radial stations	n_r	-
Number of azimuthal station	n_a	-
Inflow model	-	-

Table 3.4: Analysis set-up input data

3.2. ROTOR AERODYNAMICS

This section addresses how the blade aerodynamic load distribution is obtained for a given velocity field (3.2.1) by applying the principles of the blade element theory (3.2.2) to two-dimensional elements whose associated aerodynamic coefficients are taken from look-up tables (3.2.3).

3.2.1. VELOCITY FIELD

In order to determine the aerodynamic load distribution acting on the blades, the velocity pattern about the rotor must be known in advance. Two different ways are regarded by BEAT to obtain this information. The first possibility is to calculate the velocity component over the rotor disk directly from the input data specified by the user. In this approach, the velocities induced by the rotor are computed by means of static inflow models. On the other hand, if BEAT is coupled with TAU, the velocity distribution is imported from the CFD solver output data. Nevertheless, in order to initialize the coupling of both tools, the first approach is required to be used at the first iterative step.

ROTOR DISK REFERENCE SYSTEM

In both cases the velocity field is computed at the rotor disk. This reference surface is assumed to be contained in the plane of rotation which is perpendicular to the rotor shaft axis. A local reference system for the helicopter main rotor (figure 3.2) is defined, where its origin is located at the rotor disk center, the x_d -axis is contained in the plane of rotation and is longitudinally oriented pointing to the helicopter rear part, and the z_d -axis represents the shaft axis direction. Thus, for zero shaft angle configurations the rotor reference system coincides with the global helicopter system. According to the local reference system definition, both the longitudinal v_{x_d} and axial v_{z_d} flow velocity components can be

determined by:

$$v_{x_d} = v_h \cos \alpha_s - v_a \sin \alpha_s \quad (3.1)$$

$$v_{z_d} = -v_h \sin \alpha_s - v_a \cos \alpha_s - v_i \quad (3.2)$$

where positive values of the axial induced velocity v_i corresponds to flow transport from the upper to the lower side of the rotor disk.

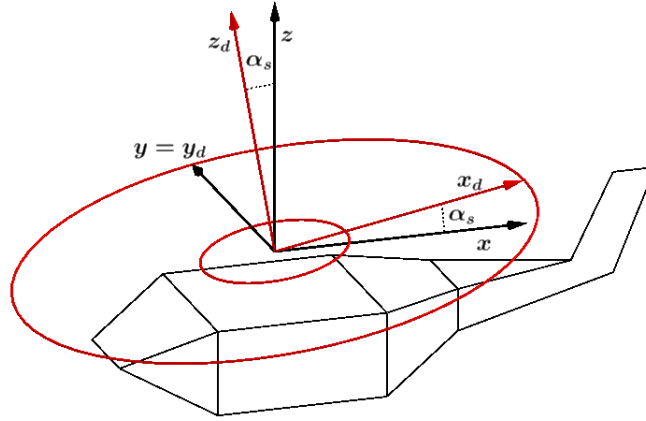


Figure 3.2: Rotor disk local reference system

INDUCED VELOCITY

The axial induced velocity distribution v_i at the rotor plane can be estimated by means of static inflow models. The use of these analytical methods offers an approximation of the time-averaged induced velocity pattern, whose physics can not be thoroughly modeled due to its strong dependence on aspects such as the blade motion along its degrees of freedom, aerodynamic load distribution and blade vortex interaction effects among others. BEAT enables the user to choose between two inflow models: uniform and linear induced velocity distribution.

The uniform induced velocity method is based on the momentum theory, that models the helicopter rotor as an actuator disk where the thrust is assumed to be uniformly distributed. Considering that the only force produced within the streamtube bounded by the disk is the thrust applied by the rotor, the application of the conservation of momentum equation in a direction perpendicular to the rotor disk yields:

$$v_i = \frac{T}{2\rho A \sqrt{v_{x_d}^2 + v_{z_d}^2}} \quad (3.3)$$

This approach is especially suited for hovering flight conditions, where in spite of the fact that the actual induced velocity pattern is not fully uniform, it can be considered axisymmetric. In this case, due to the absence of both forward and axial flight velocity components, (3.3) is reduced to:

$$v_i = \sqrt{\frac{T}{2\rho A}} \quad (3.4)$$

The use of a uniform static inflow model can be regarded as an inadequate approach in forward flight conditions. Linear inflow models are based on the idea that the induced velocity varies linearly along the longitudinal rotor disk direction. In the last decades, research has been conducted to determine the induced velocity longitudinal gradient depending on the flight conditions [56]. For high forward speeds, the static Pitt and Peters inflow model [34] is shown to be in good agreement with helicopter experimental data. According to the Pitt and Peters model, the axial induced velocity can be expressed by:

$$v_i = v_{i0} \left(1 + \frac{15\pi}{23} \frac{x_d}{R} \tan \frac{\chi}{2} \right) \quad (3.5)$$

where v_{i0} is the mean induced velocity at the center of the rotor disk and is computed by applying (3.3). The longitudinal gradient is assumed to be a function of the wake skew angle χ , that is defined by:

$$\chi = \tan^{-1} \left(-\frac{v_{x_d}}{v_{z_d}} \right) \quad (3.6)$$

where the axial velocity term v_{z_d} is computed by considering the average induced velocity v_{i0} .

The application of any of the two aforementioned static inflow models needs to solve the nonlinear equation (3.3). It can be done by means of a iterative process and taking the induced velocity at hover flight conditions for the prescribed thrust force (3.4) as the initial value of v_i .

BLADE REFERENCE SYSTEM

In order to perform a two-dimensional aerodynamic analysis along the cross-sectional elements that compose the rotor blades, the flow velocity field must be projected onto a local reference system linked to each blade. The location of any blade section can be defined by its radial distance from the rotor center r , and the azimuth angle ψ relative to the x_d -axis. The criteria which is used to define the orientation of the azimuth angle is the sense of rotation of the rotor about the shaft. Hence, for a counterclockwise rotational motion, the y_d -axis direction is equivalent to an azimuth angle of $\psi = 90^\circ$. As it is displayed in figure 3.3, the x_b -axis of the blade reference system represents the radial direction, while the the azimuthal component is covered by the y_b -axis.

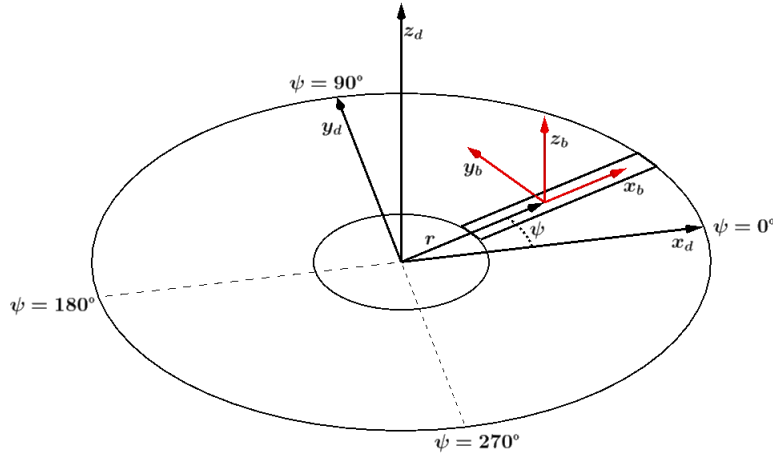


Figure 3.3: Blade local reference system

Therefore, the flow velocity relative to a sectional element defined by its radial coordinate r and azimuth angle ψ of a blade which is rotating with an angular velocity Ω and whose flapping motion along the azimuth angle is defined by β , can be computed by:

$$v_{x_b} = v_{x_d} \cos\psi \cos\beta \quad (3.7)$$

$$v_{y_b} = -v_{x_d} \sin\psi - \Omega r \quad (3.8)$$

$$v_{z_b} = v_{z_d} - v_{x_d} \cos\psi \sin\beta - \dot{\beta}(r - e) \quad (3.9)$$

3.2.2. BLADE ELEMENT ANALYSIS

The aerodynamic load distribution acting along the blade span is computed by performing a two-dimensional analysis based on the blade element theory principles. The blade is divided into sectional elements dr along its radius. These elements are modeled as two-dimensional airfoils totally independent of the adjacent sectional elements, which means that interactive effects among them are neglected and each element can be examined separately. Since the problem is reduced to the aerodynamic analysis at the plane defined by each blade element (figure 3.4), the flow velocity relative to the sectional element is determined by the axial and the tangential velocity components, while the influence of radial velocity is disregarded. One of the advantages of this theory with respect to the momentum theory is that it enables the computation of the aerodynamic load distribution along the blade radius through the integration of the forces acting on each sectional element.

The resultant flow velocity U_R at a blade sectional element located at radial distance r is defined by two components, one parallel, U_P , and the other perpendicular, U_T , to the rotor shaft axis. The axial component U_P , accounts for the perpendicular velocity computed at the blade as well as for the perturbation in velocity caused by the blade flapping motion $\beta(\psi)$. On the other hand, the tangential component U_T accounts for the azimuthal flow component relative to the blade section.

$$U_P = -v_{z_b}(r, \psi) \quad (3.10)$$

$$U_T = -v_{y_b}(r, \psi) \quad (3.11)$$

Applying the Pythagorean theorem to the aforementioned velocity components, the resultant flow velocity relative to the blade sectional element can be calculated. In addition, its associated Mach number can be obtained by dividing it by the speed of sound. To do that, variations in temperature are neglected, hence, the temperature defined by the user is used.

$$U_R = \sqrt{U_p^2 + U_T^2} \quad (3.12)$$

$$M_R = \frac{U_R}{\sqrt{\gamma RT_\infty}} \quad (3.13)$$

The effective angle of attack is determined by the pitch angle θ and the relative inflow angle ϕ defined by the axial and tangential velocity components. The pitch angle at the analyzed station is composed of the geometrical blade twist, which is assumed to be linear, and the control pitch inputs adjusted by the pilot.

$$\alpha = \theta - \phi = \theta - \tan^{-1}\left(\frac{U_p}{U_T}\right) \quad (3.14)$$

Once that both the sectional resultant velocity Mach number M_R and the local angle of attack α are known, the lift and drag two-dimensional coefficients can be extracted from the airfoil look-up tables. In this data files, the aerodynamic coefficients are given for some reference values of Mach number and incidence angle, therefore, an interpolation algorithm is used to determine the associated values with each sectional flow characteristics (3.2.3). These coefficients are required for the calculation of both lift and drag force acting on each sectional blade element of span length dr and local chord c .

$$dL = \frac{1}{2}\rho U_R^2 c c_l dr \quad (3.15)$$

$$dD = \frac{1}{2}\rho U_R^2 c c_d dr \quad (3.16)$$

The aerodynamic loads can be projected in the axial and tangential direction by:

$$dT = dL \cos\phi - dD \sin\phi \quad (3.17)$$

$$dF_T = dL \sin\phi + dD \cos\phi \quad (3.18)$$

which can also be expressed in the local blade reference system:

$$f_{y_b} = -dF_T \quad (3.19)$$

$$f_{z_b} = dT \quad (3.20)$$

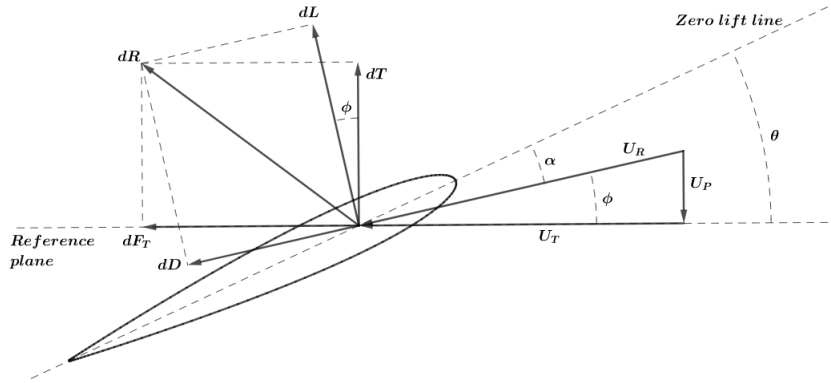


Figure 3.4: Aerodynamic forces acting on a blade section

Both the tangential (3.19) and the axial (3.20) load components at each rotor disk station expressed in the local blade reference system need to be transferred to the TAU actuator disk module before running any CFD simulation. If no load distribution is prescribed, the flow velocity will not experience any change in direction and intensity due to the presence of the actuator disk. Furthermore, once that the aerodynamic load distribution over the disk is obtained, some rotor performance characteristics such as the thrust T and the rotor hub rolling M_{x_d} and pitching M_{y_d} moments can be computed. The values assigned to the aforementioned variables represent the time-averaged solution. Since the actuator disk is discretized according to a uniform distribution of stations about the azimuth, each rotating blade is assumed to be contained the same amount of time at each azimuthal station. Hence, the thrust (3.21), rolling moment (3.22) and pitching moment (3.23) is determined as the average value of the contribution of each azimuthal station.

$$T = \frac{N_b \sum_{i=1}^{n_r} \sum_{j=1}^{n_a} f_{z_b}(r_i, \psi_j)}{n_a} \quad (3.21)$$

$$M_{x_d} = \frac{N_b \sum_{i=1}^{n_r} \sum_{j=1}^{n_a} f_{z_b}(r_i, \psi_j) r_i \sin \psi_j}{n_a} \quad (3.22)$$

$$M_{y_d} = - \frac{N_b \sum_{i=1}^{n_r} \sum_{j=1}^{n_a} f_{z_b}(r_i, \psi_j) r_i \cos \psi_j}{n_a} \quad (3.23)$$

These rotor performance variables can be also expressed by means of non-dimensional parameters: thrust, rolling moment and pitching moment coefficients. In this work, the reference area A is defined by the annular rotor disk surface and the tip speed velocity in hovering flight ΩR is taken as reference velocity.

$$c_T = \frac{T}{\rho A (\Omega R)^2} \quad (3.24)$$

$$c_{RM} = \frac{M_{x_d}}{\rho A \Omega^2 R^3} \quad (3.25)$$

$$c_{PM} = \frac{M_{y_d}}{\rho A \Omega^2 R^3} \quad (3.26)$$

3.2.3. AIRFOIL POLARS

The two-dimensional aerodynamic coefficients which correspond to each blade sectional element are extracted from airfoil look-up tables. These data files are taken from the DLR database that is used to perform analyses with the comprehensive rotor code HOST. The aerodynamic coefficients are given for different angles of attack between -180° and 180° and Mach numbers within a range from 0 to low supersonic regime. Depending on the selected airfoil, the aerodynamic characteristics associated with pre-stall conditions (i.e. low incidence angles) have been obtained from wind tunnel measurements, CFD analysis, or panel codes. On the other hand, for post-stall conditions (i.e. high incidences angles), the aerodynamic coefficients have been extrapolated by applying different techniques such as the Viterna and Montgomerie methods. In addition, it must be taken into consideration that while in pre-stall conditions both the angle of attack and Mach number are required to determine the airfoil aerodynamic data, the post-stall airfoil data is only defined by the angle of attack. The dependence of the lift and drag coefficients on the incidence angle and sectional Mach number is displayed in figure 3.5 for the rotorcraft OA213 airfoil designed by the French Aerospace Center (ONERA).

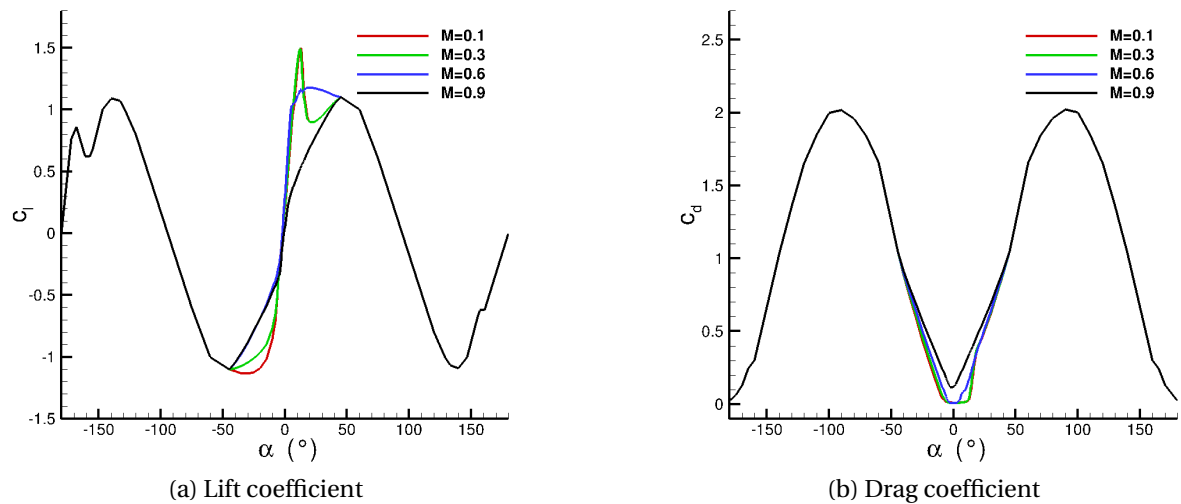


Figure 3.5: OA213 airfoil aerodynamic coefficients

Both the lift and drag two-dimensional coefficients are determined for prescribed values of angle of attack and Mach number by means of a linear interpolation algorithm [57]. Firstly, as it is shown in figure 3.6 given a pair of values α_p and M_p assigned to a blade sectional element, the endpoints of the intervals containing the considered values are found. Subsequently, for the lower M_j and upper M_{j+1} interval Mach number boundary values and the prescribed angle of attack α_p , the aerodynamic coefficients (f_{12} and f_{34} in figure

3.6) are computed. Finally, linear interpolation is applied between the coefficient values obtained at the previous step.

$$f_{12} \approx f_1 + \frac{\alpha_p - \alpha_i}{\alpha_{i+1} - \alpha_i} (f_2 - f_1) \quad (3.27)$$

$$f_{34} \approx f_3 + \frac{\alpha_p - \alpha_i}{\alpha_{i+1} - \alpha_i} (f_4 - f_3) \quad (3.28)$$

$$f_p \approx f_{12} + \frac{M_p - M_j}{M_{j+1} - M_j} (f_{34} - f_{12}) \quad (3.29)$$

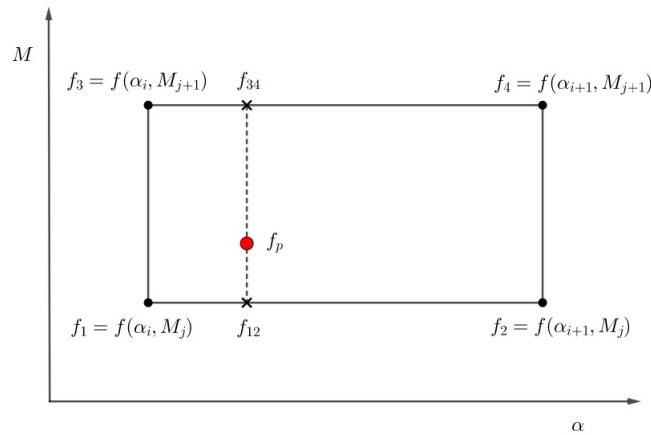


Figure 3.6: Interpolation scheme used to determine the airfoil aerodynamic coefficients

3.3. ROTOR AEROMECHANICS

The motion of the helicopter blades and the aerodynamic forces acting on them are coupled facts. A change in control inputs provided by the pilot modifies the distribution of the loads along the blades in each azimuthal position as well as the equilibrium trajectory pattern of the blades. The rotor hub is the responsible for inducing the blade pitching motion as well as for allowing the blades to flap and lead or lag. According to the type of attachment between the blades and the hub Leishman [58] divided the helicopter rotor configurations into four groups: teetering, articulated, hingeless, and bearingless. The teetering type is associated with two-bladed rotors with an independent feathering bearing on each blade and a common flapping hinge located at the rotational axis. Hence, its mechanics can be compared to a seesaw, while one blade flaps up the opposite flaps down. The articulated rotor presents feathering, flapping, and leading-lagging hinges which allow the blades to flap in order to alleviate the loads at the root and to lead-lag so as to reduce the influence of the Coriolis forces produced by the flapping motion of the blade. In the hingeless configuration flapping and leading-lagging motions are enabled by means of flexible materials which replace both hinges and pitch control is carried out by a feathering bearing. Bearingless designs also eliminates the feathering bearing and the blade motion is possible by twisting, flexing and bending. Due to the absence of hinges and bearings, the hub structure deals with high-cyclic loads, thus the use of materials with high fatigue resistance is required.

Pitching motion is applied to the rotor blades by the use of pilot sticks or actuators. It can be expressed in terms of a Fourier series, nonetheless, generally only the constant value and the first harmonic terms are considered (3.30). The use of higher harmonics enables the reduction of flow unsteadiness effects such as vibrations. Shaw et al. [59] analyzed the influence of including higher harmonic terms in the pitch angle distribution around the azimuth of a three-bladed articulated helicopter rotor (CH-47D Chinook) by performing wind tunnel experiments. Due to the low amplitude of these additional high harmonic terms small changes in rotor performance were noticed but it was checked that the vibration alleviation was considerable in unsteady flight conditions. Nevertheless, BEAT models the rotor pitching motion about the feathering hinge as a first-harmonic distribution function of the azimuth angle.

$$\theta(\psi) = \theta_0 + \theta_{1c} \cos\psi + \theta_{1s} \sin\psi \quad (3.30)$$

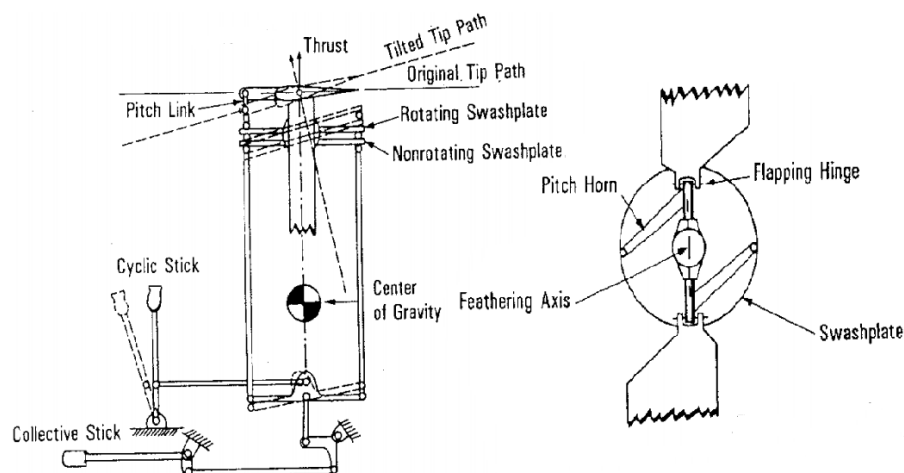


Figure 3.7: Basic helicopter control system[60]

The pitch inputs are defined by the pilot by the use of actuators: collective lever and cyclic stick. The deflection of the actuators is transferred to the feathering bearing on each blade by means of the swashplate (Figure 3.7). It consists of two concentric disks around the rotor axis one above the other, the one which is placed below is non-rotating and the other rotates with the same rotational speed as the rotor does. Between both disks, a set of bearings are located which enable the rotation of the upper disk. A pitch link and a pitch horn connects the rotating swashplate with the feathering bearing of each blade. The action of the collective lever controls the collective pitch (θ_0) by moving the swashplate vertically while it is maintained perpendicular to the rotor shaft. This vertical displacement turns into constant pitch around the azimuth, positive when it is moved upwards and vice versa. On the other hand, the swashplate is tilted by operating the cyclic stick, which by means of actuators can be inclined both longitudinally and laterally inducing a cyclic blade pitch distribution whose period is equal to one revolution. As a consequence of change in aerodynamic loads along the blades induced by the pitch control, the blades flap about their flapping hinges and, thus, the rotor is tilted. Since rotor thrust vector is perpendicular to the plane defined by the blade tips, tilting the rotor produces pitching and rolling moments. Prouty and Curtiss [60] reviewed the development of helicopter systems, ranging from the first mechanical systems to the modern “fly-by-wire” configurations.

3.3.1. ROTOR TRIM

The asymmetrical load distribution about the helicopter rotor can lead to undesirable moments with respect to the hub. The objective of rotor trim is to adjust the control input parameters required to reach a desired steady flight condition. Thus, a control vector \mathbf{X} (3.31) which contains the input parameters is adjusted until the rotor achieves prescribed performance conditions which are contained in a response vector \mathbf{Y} (3.32). The control vector collects the pitch inputs defined by the use of actuators which determine the blade pitch angle distribution around the azimuth (3.30). On the other hand, the response vector stores the properties that define the desired state such as the coefficients of thrust, pitching moment, and rolling moment.

$$\mathbf{X} = (\theta_0, \theta_{1c}, \theta_{1s}) \quad (3.31)$$

$$\mathbf{Y} = (c_T, c_{PM}, c_{RM}) \quad (3.32)$$

The value of the thrust coefficient c_T is assigned so as to the lift force generated by the rotor blades balances the weight of the helicopter. The lift force is obtained by projecting the thrust vector onto the vertical direction. Since the aerodynamic loads are assumed to act on a rotor disk contained in the plane of rotation which is perpendicular to the shaft axis, the thrust vector direction is defined by the shaft axis orientation. Thus, the rotor longitudinal shaft angle α_s must be taken into account to determine the thrust vertical component or lift force:

$$T \cos \alpha_s = W \quad (3.33)$$

and applying the definition of thrust coefficient given in (3.24):

$$c_T = \frac{W / \cos \alpha_s}{\rho S (\Omega R)^2} \quad (3.34)$$

Concerning the other two components of the response vector \mathbf{Y} , both are defined in order to accomplish equilibrium of moments about the rotor hub. Therefore, the values assigned to the pitching and rolling moment coefficients are equal to zero.

$$c_{PM} = 0 \quad (3.35)$$

$$c_{RM} = 0 \quad (3.36)$$

Since the relation between the control variables and the response state is nonlinear an iterative technique is needed to reach convergent solutions. With this aim in view, a Newton-Raphson algorithm has been implemented. The roots of the nonlinear system of equations are found by computing the tangent line through the estimated point at each iterative step and taking the point where the tangent line intersects to zero as the estimated value of the next iterative step [57]. Initial values of \mathbf{X} are guessed to initialize the iterative process. The coupling equations between control and response vector are linearized by using a first-order Taylor series expansion.

$$\mathbf{Y}(\mathbf{X} + \Delta \mathbf{X}) = \mathbf{Y}(\mathbf{X}) + \mathbf{J} \Delta \mathbf{X} \quad (3.37)$$

The term \mathbf{J} in (3.37) represents the Jacobian matrix, which is a square matrix of order 3 that is updated at each iterative step. It contains the first-order partial derivatives of the response vector with respect to the control vector. Hence, it can be defined according to:

$$\mathbf{J} = \frac{\partial (c_T, c_{PM}, c_{RM})}{\partial (\theta_0, \theta_{1c}, \theta_{1s})} \quad (3.38)$$

$$\mathbf{J} = \begin{pmatrix} \frac{\partial c_T}{\partial \theta_0} & \frac{\partial c_T}{\partial \theta_{1c}} & \frac{\partial c_T}{\partial \theta_{1s}} \\ \frac{\partial c_{PM}}{\partial \theta_0} & \frac{\partial c_{PM}}{\partial \theta_{1c}} & \frac{\partial c_{PM}}{\partial \theta_{1s}} \\ \frac{\partial c_{RM}}{\partial \theta_0} & \frac{\partial c_{RM}}{\partial \theta_{1c}} & \frac{\partial c_{RM}}{\partial \theta_{1s}} \end{pmatrix} \quad (3.39)$$

The partial derivatives compiled into the Jacobian matrix are numerically computed by means of a first-order finite differences approach. Each term of the response vector \mathbf{Y} is perturbed separately by imposing a variation η in one of the three control inputs contained in the vector \mathbf{X} [61]. Hence, for instance, the term located at the first row and second column of \mathbf{J} , which indicates the partial derivative of the thrust coefficient c_T with respect to the lateral cyclic angle θ_{1c} is determined by:

$$\frac{\partial c_T}{\partial \theta_{1c}} = \frac{c_T(\theta_0, \theta_{1c} + \eta, \theta_{1s}) - c_T(\theta_0, \theta_{1c}, \theta_{1s})}{\eta} \quad (3.40)$$

Rearranging (3.37) into (3.41), at each iterative step i the control values can be computed until the difference between the desired and calculated response vector is lower than a user-defined threshold. The inverse of the Jacobian matrix is computed by means of a LU decomposition method which is included in the DGETRF and DGTRI subroutines of the numerical linear algebra software library LAPACK.

$$\begin{pmatrix} \theta_0 \\ \theta_{1c} \\ \theta_{1s} \end{pmatrix}_{i+1} = \begin{pmatrix} \theta_0 \\ \theta_{1c} \\ \theta_{1s} \end{pmatrix}_i + \mathbf{J}^{-1} \left\{ \begin{pmatrix} c_T \\ c_{PM} \\ c_{RM} \end{pmatrix}_{desired} - \begin{pmatrix} c_T \\ c_{PM} \\ c_{RM} \end{pmatrix}_i \right\} \quad (3.41)$$

It must be noted that while in this module the values of the control pitch inputs varies until the flight conditions stated by the prescribed objective vector are achieved, the flapping motion remains unaltered. Therefore, changes in pitch angle distribution only affect the blade sectional angles of attack. In addition, the initial guess of the control vector \mathbf{X} required to run the iterative algorithm is composed by the trimmed control values that were obtained from the previous blade flap angle distribution.

3.3.2. BLADE FLAPPING MOTION

Changes in control pitch inputs produce variations in aerodynamic loads acting on the blades, which flap up or down about the flapping hinge to reach a new equilibrium state. The implemented algorithm to determine the blade flapping motion is based on the method described by Gessow [62, 63] at which equilibrium of moments about the blade flapping hinge, radially offset from the shaft axis is applied. The forces acting on a differential length blade element, dr , with a mass distribution m per unit length are indicated in Figure 3.8.

Hence, the differential equation of blade flapping motion can be derived by imposing that the moments about the flapping hinge (M_β) due to aerodynamic (M_T), centrifugal (M_{CF}), inertia (M_I), and gravitational forces (M_W) are balanced (3.42). It has to be noted that no lead-lag motion is considered in the present work.

$$\sum M_\beta = M_{CF} + M_I + M_T + M_W = 0 \quad (3.42)$$

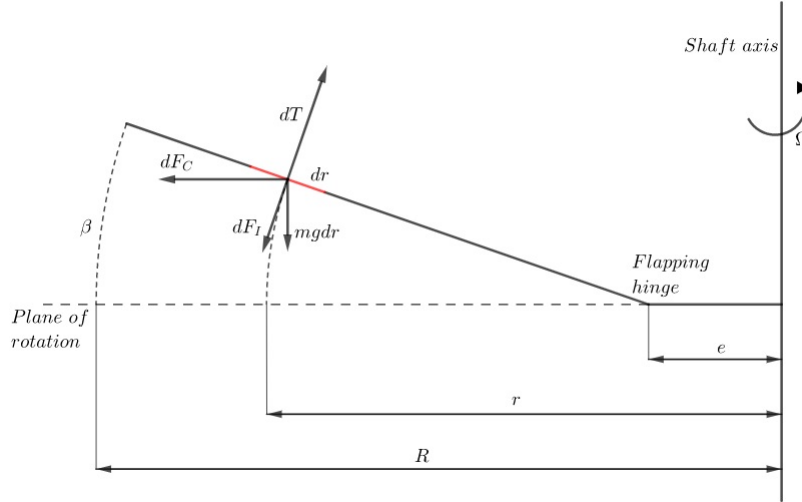


Figure 3.8: Flapping hinge equilibrium

FLAPPING MOMENT COMPUTATION

As it is expressed in (3.42), the moment about the flapping hinge is defined by the contribution of the centrifugal, inertia, aerodynamic, and gravitational loads. The influence that each term has on the total flapping moment is computed separately.

Since the analysis of forces and flapping moments acting on the blade is carried out by using a rotating reference system, the effect of the centrifugal force must be taken into account. The rotational motion with constant angular velocity Ω of each rotor blade and its associated local reference system induces a centrifugal force dF_C acting on a differential blade element of mass $m dr$ which is perpendicular to the shaft axis and points outwards (3.43). The moment about the flapping hinge produced by the centrifugal force can be obtained by integrating the product of the perpendicular component of the centrifugal force to the blade and the distance to the flapping hinge along the blade element (3.44). It has to be noted that the negative sign in (3.44) is due to the fact that the centrifugal force moment about the flapping hinge has a flapping-down orientation for positive flap angles.

$$dF_C = m\Omega^2 [e + (r - e) \cos\beta] dr \quad (3.43)$$

$$M_{CF} = - \int_{r_p}^R m\Omega^2 (r - e) [e + (r - e) \cos\beta] \sin\beta dr \quad (3.44)$$

Inertia force generates a flapping-down moment expressed in (3.46), where I_β represents the blade moment of inertia about the flapping hinge. Since the blade mass distribution m along its radius is assumed to be a continuous function, the blade moment of inertia can be computed according to (3.45).

$$I_\beta = \int_{r_p}^R m(r-e)^2 dr \quad (3.45)$$

$$M_I = -I_\beta \ddot{\beta} \quad (3.46)$$

The angular acceleration about the flapping hinge is given by the second derivative of the flap angle with respect to time $\ddot{\beta}$. The independent variable can be modified from the time t to the azimuth angle ψ by means of the chain rule. Hence, the first derivative of the flap angle with respect to the azimuth location $\dot{\beta}$ is determined by applying the chain rule once (3.47), while the second derivative $\ddot{\beta}$ is computed by applying the aforementioned approach twice (3.48).

$$\dot{\beta} = \frac{\partial \psi}{\partial t} \frac{\partial \beta}{\partial \psi} = \Omega \bar{\beta} \quad (3.47)$$

$$\ddot{\beta} = \Omega \frac{\partial^2 \beta}{\partial \psi \partial t} = \Omega^2 \bar{\bar{\beta}} \quad (3.48)$$

Combining (3.46) and (3.48), the moment about the blade flapping hinge produced by the action of inertia loads can be expressed as :

$$M_I = -I_\beta \Omega^2 \bar{\bar{\beta}} \quad (3.49)$$

The aerodynamic force component normal to the blade determined in (3.17) has a flapping-up contribution to the equilibrium equation about the flapping hinge (3.50). As it has been previously explained both the flap angle and its first derivative are taken into account to compute the relative inflow angle to each two-dimensional blade sectional element. It has to be noted, that flapping motion modifies the angle of attack of a blade element with respect to the flow, flap-up motion reduces the angle of attack and vice versa. This fact is represented by including a vertical velocity component relative to the blade element equal to $\dot{\beta}(r-e)$.

$$M_T = \int_{r_p}^R (r-e) dT \quad (3.50)$$

And the contribution of gravitational effects produces a moment which tends to flap-down the blade (3.51).

$$M_W = - \int_{r_p}^R mg(r-e) \cos \beta dr \quad (3.51)$$

DIFFERENTIAL EQUATION SOLUTION

The flapping motion distribution as a function of the azimuth angle ψ can be computed by solving the second-order ordinary differential equation (3.42). Numerical methods are used to determine the solution of this equation while the trimmed values of the control inputs are assumed to remain constant. The developed algorithm which is responsible for its calculation determines the flap angle β as well as its first $\dot{\beta}$ and second $\ddot{\beta}$ derivative with respect to the azimuth angle at each of the azimuthal stations at which the rotor disk is

discretized. Elastic deformations of the rotor blades are neglected, which means that the flapping characteristics at any azimuth angle do not vary along the blade span.

Initial guess of both the flap angle β and its first derivative $\bar{\beta}$ at $\psi = 0$ is required to initialize the numerical strategy. Values equal to zero for both variables are taken as the starting point at the first loop of the tool, while at the successive ones the values at this azimuth angle computed at the previous loop are employed. The rotor disk is divided into n_a azimuthal stations uniformly distributed which are numbered according to the rotation direction (i.e. counterclockwise) starting at $\psi = 0$. The subscripts of the expressions given in this section denotes the order assigned to each station.

Firstly, at $\psi = 0$ for the considered values of β_1 and $\bar{\beta}_1$, the second derivative of the flap angle with respect to the azimuth angle can be calculated by applying:

$$\bar{\bar{\beta}}_1 = \frac{M_{CF_1} + M_{T_1} + M_{W_1}}{I_\beta \Omega^2} \quad (3.52)$$

Once $\bar{\bar{\beta}}_1$ is known, the corresponding values of β and $\bar{\beta}$ at the next stations can obtained by means of a second-order and a first-order forward Euler method respectively. In these explicit schemes the variation in azimuth angle $\Delta\psi$ between two consecutive stations is used as the step size. Thus, the flap angle and its first derivative are obtained by:

$$\beta_{i+1} = \beta_i + \bar{\beta}_i \Delta\psi + \bar{\bar{\beta}}_i \frac{\Delta\psi^2}{2} \quad (3.53)$$

$$\bar{\beta}_{i+1} = \bar{\beta}_i + \bar{\bar{\beta}}_i \Delta\psi \quad (3.54)$$

After computing β_{i+1} and $\bar{\beta}_{i+1}$, the aerodynamic load distribution acting on the rotor blade at the considered azimuthal station is calculated. Subsequently, the second derivative $\bar{\bar{\beta}}_{i+1}$ is determined by imposing equilibrium of moments about the flapping hinge:

$$\bar{\bar{\beta}}_{i+1} = \frac{M_{CF_{i+1}} + M_{T_{i+1}} + M_{W_{i+1}}}{I_\beta \Omega^2} \quad (3.55)$$

This procedure is repeated until the values of β_{n_a+1} and $\bar{\beta}_{n_a+1}$ are obtained. If the difference between them and the ones associated with the first station is lower than a predefined tolerance value ε , convergence is assumed to be reached and the iterative process is stopped.

$$|\beta_{n_a+1} - \beta_1| < \varepsilon \quad |\bar{\beta}_{n_a+1} - \bar{\beta}_1| < \varepsilon \quad (3.56)$$

On the other hand, if the convergence criteria is not satisfied, the assigned values at the first station are updated and a new iteration is carried out. The flowchart of the numerical scheme described in this section is displayed in figure 3.9.

$$\beta_1 = \beta_{n_a+1} \quad (3.57)$$

$$\bar{\beta}_1 = \bar{\beta}_{n_a+1} \quad (3.58)$$

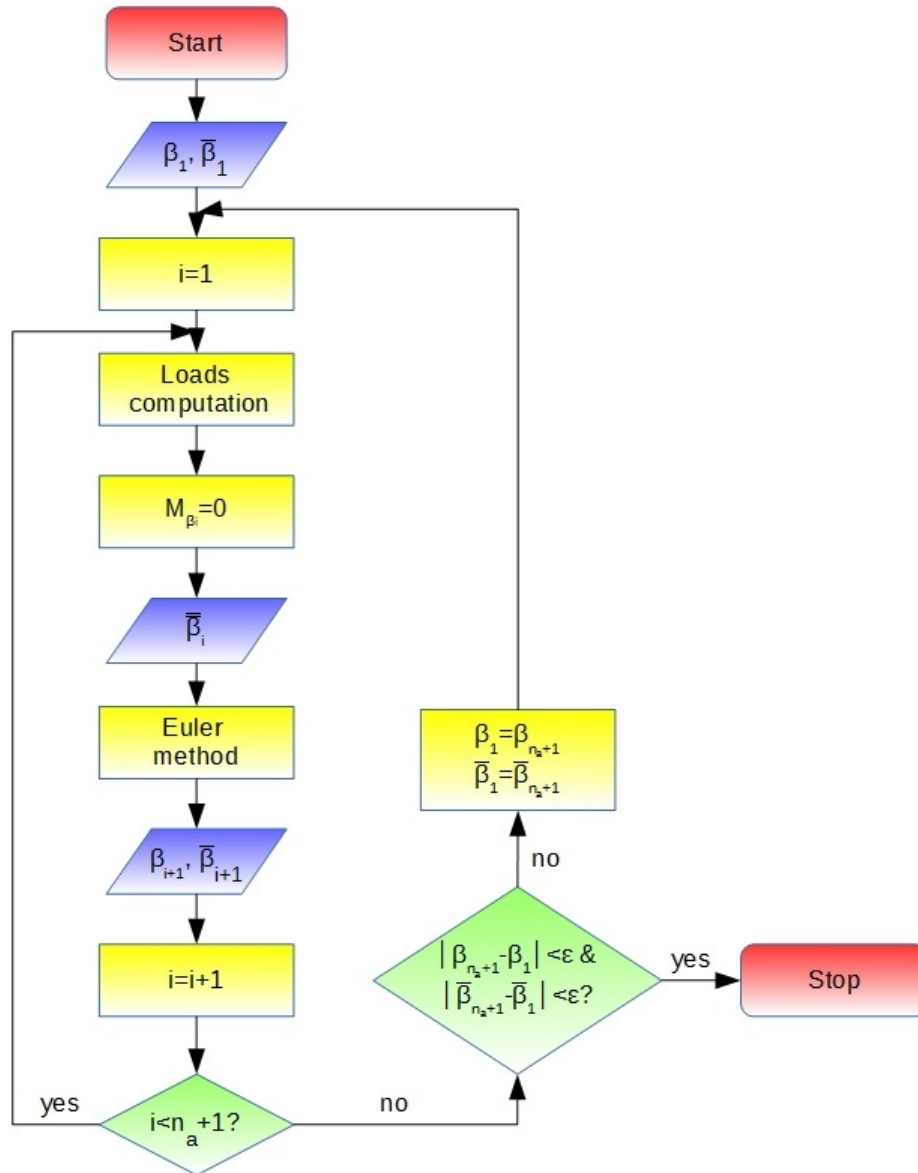


Figure 3.9: Blade flapping motion algorithm

3.4. BEAT STRUCTURE OVERVIEW

A simplified scheme of the developed code structure is shown in figure 3.10. The velocity field over the rotor disk can be computed by either the coupling with the actuator disk module included in TAU or the use of static inflow models. The coupling between BEAT and TAU consists of an iterative process (Chapter 6) in which the forces computed by the tool are subjected to the flow velocities provided by TAU. The velocity vector obtained at each station of the discretized disk is used to determine the effective angle of attack of each section with respect to the inflow direction as well as its associated Mach number. The two-dimensional aerodynamic coefficients along the blade are taken from look-up tables and are used to compute both the axial and tangential force distributions which are transmitted

to TAU in case that the coupling is defined. Furthermore, pitching and flapping degrees of freedom are considered and contribute to the calculation of the blade angle of attack. Thus, an internal iterative process is defined to compute the blade motion along each azimuthal position. Firstly, for constant collective and cyclic pitch control inputs, the application of the equilibrium of moments about the flapping hinge enables the calculation of the flap angles. Subsequently, an iterative Newton-Raphson technique is employed to adjust the pitch angles for the steady flight condition prescribed by the user.

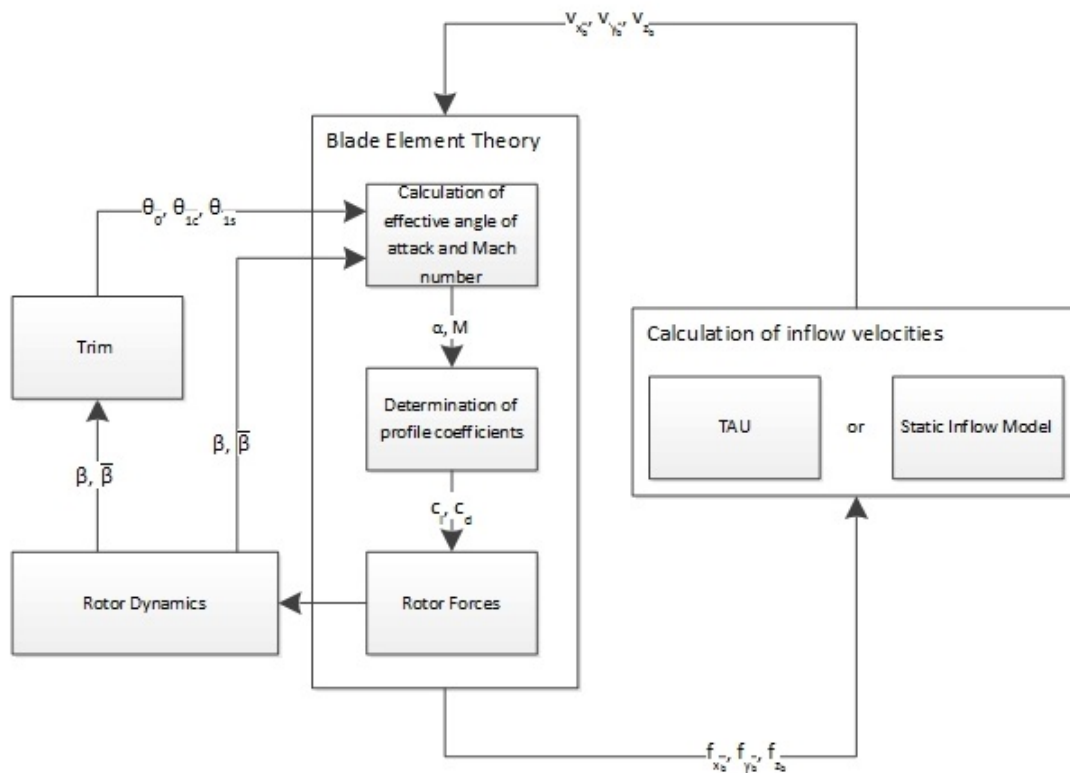


Figure 3.10: BEAT structure scheme

4

ANALYSIS OF THE RESULTS AND VERIFICATION OF BEAT

This chapter covers the analysis of the results computed by BEAT for an isolated rotor in hover and forward flight. The objective of this analysis is the verification of the tool, which is the assessment of whether or not the code gives the correct results for the set up equations and assumptions. Hence, the study carried out in the next sections aims to answer the question: Does BEAT work correctly? With this objective in mind, two approaches have been followed. Firstly, an evaluation of the influence of the input variables on the obtained results is carried out. Secondly, the result outcomes are compared with those determined by the comprehensive rotor code HOST developed by Eurocopter [46]. HOST also models the blade by means of the blade element theory, nevertheless, it can account for elastic deformations and blade motion along the three degrees of freedom. In order to arrange proper comparisons, in the computations performed by HOST the same airfoil lookup tables are used and both elastic deformations and leading-lagging blade motion are nullified.

4.1. REFERENCE HELICOPTER ROTOR

The results discussed in this chapter are computed by taking into consideration the geometrical characteristics of the rotor tested during the HART II campaign [48] which is described in more detail in Chapter 7. The analyzed rotor is a scale version of the Bo 105 helicopter (figure 4.1a) which is used at DLR for research purposes. One of the main features of this helicopter is the hingeless configuration of its main rotor (figure 4.1b). The pitch control is carried out by a system of actuators that define the blade pitching motion about the feathering bearing. On the other hand, due to the absence of flapping and lagging hinges, flapping and leading-lagging motions are enabled by means of flexible materials. The main advantage of this rotor configuration lies in the associated reduction of mechanical complexity and maintenance requirements compared to fully articulated rotor systems [64]. In addition, the absence of a blade flapping hinge results in an enhancement of the helicopter agility due to the high moments that are transmitted to the rotor hub.

The reason why the aforementioned rotor is chosen to carry out the analysis of the results and the verification process of BEAT resides in its simple blade geometry. The rotor is composed of four equally spaced blades of identical geometry. The blades are unswept and rectangular, which means that the chord distribution along its radius is constant. Fur-



(a) DLR research Bo 105. Source: DLR



(b) Bo 105 main rotor hub. Source: American Helicopter Society (AHS)

Figure 4.1: Bo 105 helicopter

thermore, the twist angle linearly decreases from the root to the tip and the blade section does not vary with the radius. The used airfoil is the NACA 23012, a cambered airfoil with a maximum thickness equal to 12% of its chord. With the objective of accounting for blade flapping motion, an effective flapping hinge radially offset from the shaft axis is modeled. It is located at 13% of the rotor radius by assuming that the rotor hub is remarkably stiffer than the blade structure [65].

The baseline rotor geometric data considered for the subsequent analysis is summarized in table 4.1. The values of the air density and temperature are determined according to the International Standard Atmosphere at sea level, $\rho_\infty = 1.225 \text{ kg/m}^3$ and $T_\infty = 288.15 \text{ K}$. Both hovering and forward flight conditions are addressed for a counterclockwise shaft rotational speed of $\Omega = 1042 \text{ rpm}$ and zero shaft angle. The thrust produced by the rotor has to balance a prescribed weight of 3300 N and the control angles are computed by imposing the condition that the pitching and rolling moments about the rotor hub have to be equal to zero.

Parameter	Symbol	Value
Blade radius	R	2 m
Flapping hinge offset	e	0.26 m
Start of the profiled part	r_p	0.44 m
Rotor blade chord	c	0.121 m
Airfoil	-	NACA 23012
Number of blades	N_b	4
Blade mass	m_b	2.24 kg
Linear blade twist rate	θ_{tw}	$-4^\circ/\text{m}$
Blade twist at $r = r_p$	θ_r	4.24°
Shaft angle	α_s	0°

Table 4.1: Rotor blade geometric data

4.2. HOVER

Hovering flight is characterized by the axisymmetric distribution of the aerodynamic loads generated by the rotor blades. This fact reduces significantly the complexity of the rotor aerodynamic analysis compared to forward flight conditions. Since the flow velocity relative to each blade sectional element is independent of the azimuth angle and it only varies with the radial component, the generated aerodynamic forces also show this pattern. The axisymmetric load distribution entails that both the pitching and the rolling moments measured at the helicopter hub are equal to zero. Therefore, the thrust force needed to balance the weight of the associated helicopter is adjusted by modifying the collective pitch control θ_0 , while the lateral θ_{1c} and longitudinal θ_{1s} cyclic pitch controls tend to zero. On the other hand, the blade flapping motion is also affected by this axisymmetric pattern, hence, it remains constant around the azimuth. BEAT assumes fully rigid blade structures which means that elastic deformations in flap angle along the radius are neglected. Thus, the flap angle at any radial and azimuthal position is constant in the modeled steady hovering flight conditions.

4.2.1. EFFECT OF THE INPUT VARIABLES

SPATIAL DISCRETIZATION

The rotor disk is modeled by BEAT as an annular surface whose inner radius is defined by the start of the profiled part of the blade while the outer radius is equivalent to the helicopter rotor radius. This surface is discretized uniformly into a user-defined number of partitions in radial and azimuthal directions. At each station, the flow velocity relative to the blade sectional element is measured at its geometric center and, hence, both the axial and tangential aerodynamic load components are computed at the same location. Due to the axisymmetric flow pattern associated with hovering flight, the use of one azimuthal station is enough for a proper rotor disk discretization. The use of more than one azimuthal stations in this case would entail redundant calculations. On the other hand, this simplification in the rotor discretization can not be applied to the radial direction due to the non-uniform load distribution along the blade span. While the chosen number of elements into which the radial distance is decomposed has little effect on the computation time required by BEAT to reach a convergent solution, which is of the order of a few seconds, it affects its accuracy.

The influence that the number of elements used for the radial discretization has on the computed solution is displayed in figure 4.2. The collective pitch control (figure 4.2a) and flap angle (figure 4.2b) are plotted against the number of radial partitions within a range from one to twenty. It is appreciated for both variables that a large number of radial elements is not required to achieve a convergent solution. The use of twenty radial stations offers a relative variation of about 0.01% in collective pitch control and flap angle with respect to the values that are obtained with ten stations. It must be taken into account that this finding can not be extended to any case since the convergence pattern can vary with the chosen blade geometry and rotational speed. In this case, the cause of the weak dependence that the solution has on the discretization radial point density can be the linear pattern of the aerodynamic load distribution along the blade (figure 4.7).

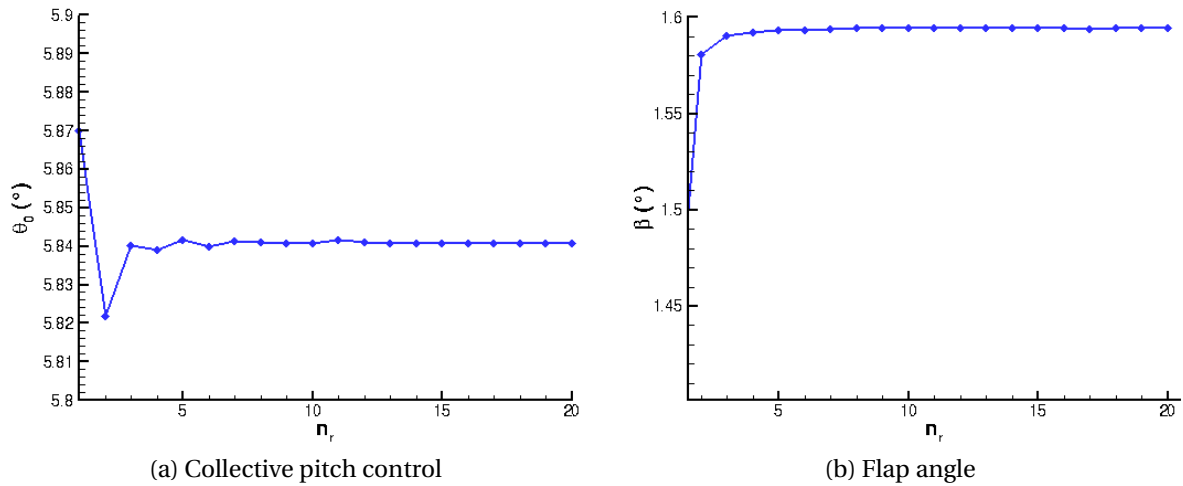


Figure 4.2: Effect of the radial discretization in hover

ROTOR RADIUS

The rotor disk area can be modified by means of changes in its radius. A decrease of the rotor radius is associated with a reduction of the disk area, hence higher collective angles are required to increase the sectional angle of attack. On the other hand, a rise in rotor radius entails a greater rotor area and higher tip velocities which reduce the required collective angle (figure 4.3).

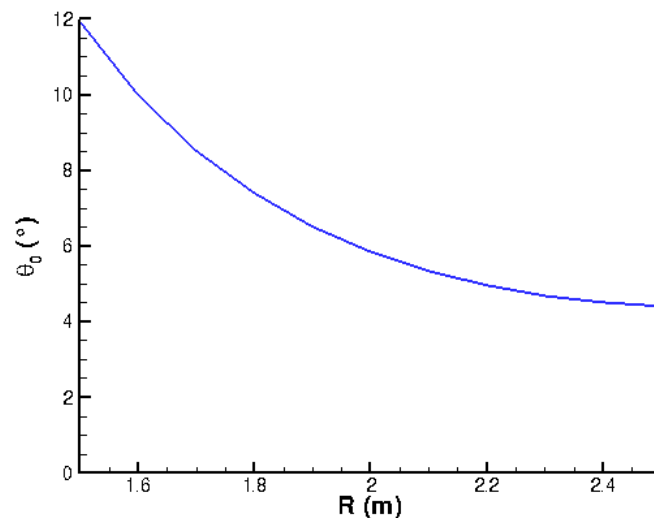


Figure 4.3: Effect of the rotor radius on the collective pitch control

PRESCRIBED THRUST

The trimming module included in BEAT aims to adjust the pitch controls to reach a prescribed steady flight condition. The thrust force generated by the blades has to balance the weight of the helicopter. As it is displayed in figure 4.4, increases in thrust requirements result in a rise of the collective pitch control in order to augment the blade sectional angle of attack. The imposition of steady flight conditions in the analysis of isolated helicopter rotors requires that both the pitching and the rolling moments about the hub have to be equal to zero. If this condition is not fulfilled the rotor will not be at an equilibrium state.

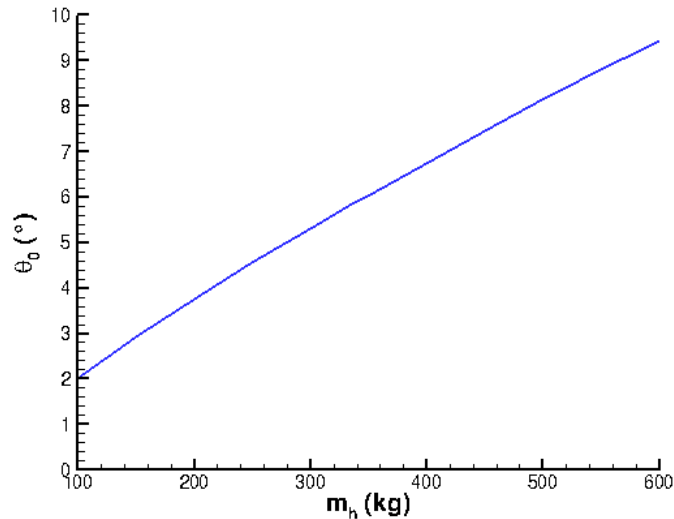


Figure 4.4: Effect of the helicopter mass on the adjusted collective control

BLADE MASS

Changes in blade mass have a noticeable influence on the flap angle distribution. The moments about the flapping hinge produced by the action of inertia, centrifugal and gravitational loads acting on the blade are proportional to its mass. Due to the axisymmetric flow pattern in hovering flight, the flap angle does not experience variations with the azimuth angle, thus, inertia loads does not contribute to the total moment about the flapping hinge. Nevertheless, for positive flap angles the moment generated by the centrifugal forces and the blade weight has a flapping-down orientation. On the other hand, for a prescribed thrust force the effect of the blade mass on the collective pitch control is practically negligible, which means that the aerodynamic load distribution along the blade span is unaltered by modifications in the value of this parameter. Therefore, as it is displayed in figure 4.5, an increase in blade mass entails that, for a given aerodynamic load distribution, the equilibrium of moments about the flapping hinge is reached at lower flap angles.

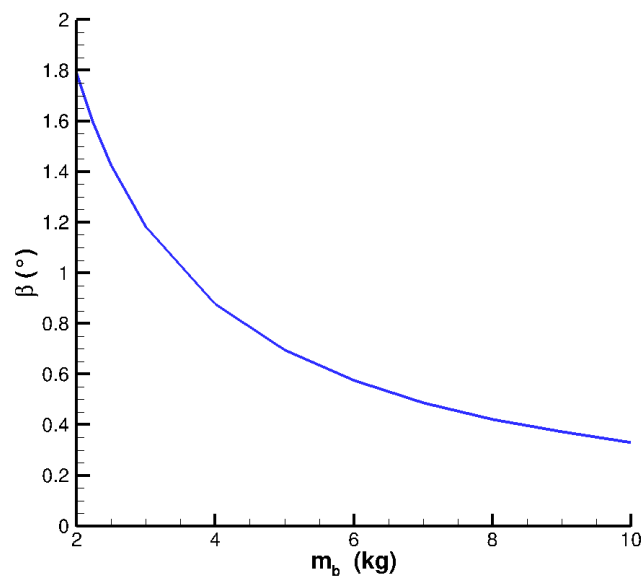


Figure 4.5: Effect of the blade mass on the flap angle

ROTATIONAL SPEED

Variations in shaft rotational speed have a strong influence on the rotor performance. An increase in rotational speed entails a rise in the flow velocity relative to each blade sectional element which magnifies the aerodynamic loads acting on it. Furthermore, the angle of attack at each two-dimensional blade element becomes larger as the rotational velocity increases. These two facts result in a decrease in the collective pitch control required to produce the prescribed thrust. Regarding the blade flap angle, as it is shown in figure 4.6, a rise in rotational speed is also associated with a lowering of the flap angle. Centrifugal forces induced by the rotational motion of the blades generate a flapping-down moment about the flapping hinge whose intensity increases with the rotational speed. Therefore, a rise in shaft angular velocity entails that the equilibrium of moments about the flapping hinge is reached at lower flap angles for a prescribed rotor thrust force.

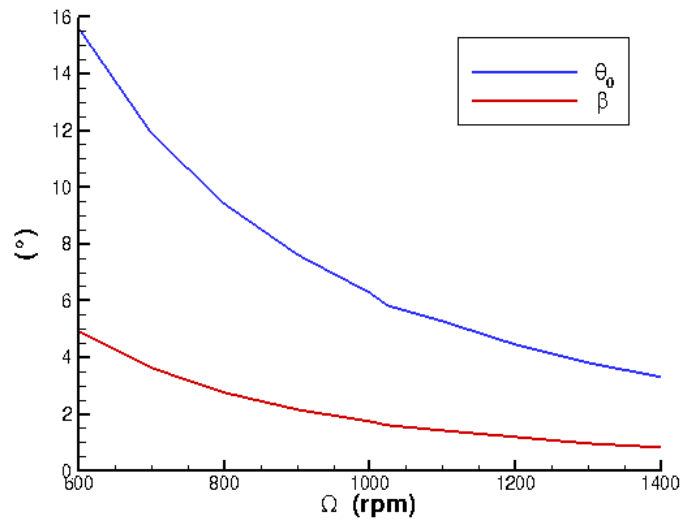


Figure 4.6: Effect of the shaft rotational speed on the collective pitch control and flap angle

4.2.2. COMPARISON WITH HOST RESULTS

The hovering flight results obtained by BEAT for the reference rotor configuration can be compared to the ones computed by HOST for the same flight case and isolated rotor configuration. Table 4.2 contains the computed values for the pitch controls and flap angle determined by both rotor analysis codes. The collective angle calculated by BEAT is 6% lower with respect to the one obtained by HOST. Moreover, a significant difference in flap angle is observed. In this case, BEAT offers a flap angle value that is 37.6% smaller than the one computed by HOST.

Variable	BEAT	HOST
θ_0	5.84°	6.19°
θ_{1c}	0	0
θ_{1s}	0	0
β	1.59°	2.55°

Table 4.2: Pitch control inputs and flap angle at hovering flight

Both the tangential f_{y_b} and the axial f_{z_b} aerodynamic load distributions along the blade span are displayed in figure 4.7. The observed increase in axial and tangential loads with respect to the radius is associated with the rise of the relative flow velocity due to the rotation of the blades. Despite the aforementioned differences in collective control and flap angle, the load curves computed by BEAT and HOST show a similar pattern.

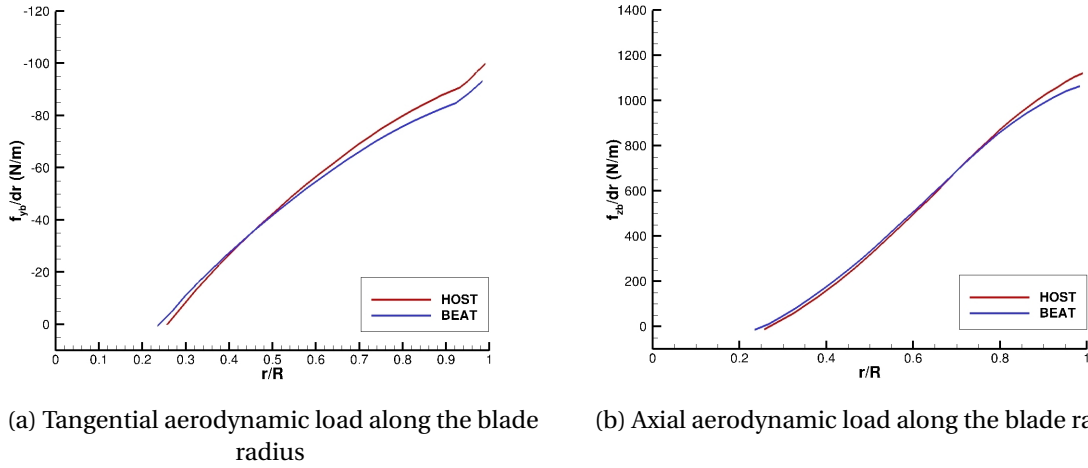


Figure 4.7: Aerodynamic load distribution in hover

The calculations performed by both tools are carried out by considering a uniform axial induced velocity distribution at the rotor plane. The constant value of the induced velocity can be determined by the application of the conservation of momentum in a direction perpendicular to the rotor. Nevertheless, it has been noticed that there is a considerable difference in this estimated value between these two rotor analysis codes. While the axial induced velocity computed by BEAT is $v_i = 10.6 \text{ m/s}$, HOST considers it equal to $v_i = 11.4 \text{ m/s}$, which is 7.55% higher than the one calculated by BEAT. The reason of this increase in axial induced velocity is that HOST accounts for the shed vorticity at the root and the tip of the rotor blade, effects that are not addressed by the pure blade element theory. Due to the difference in pressure between the upper and lower sides of the blade, there is a flow at the tip and the root from the pressure side to the suction side which reduces the aerodynamic loads acting on these regions. HOST models the vorticity effects by assuming that the loads act over an effective area lower than the actual rotor disk area. Hence, applying the momentum theory, a higher value of induced velocity is required to produce the prescribed thrust force.

As it can be seen in figure 4.7, the blade tip is a highly-loaded region. Hence, the effect of a correct modeling of the shed vorticity on the load curves would be the reduction of the loads at this zone. In spite of the availability of approaches to address these effects, such as the Prandtl tip loss factor that is commonly used in propeller analysis [66], BEAT does not include any of them.

In order to assess the influence that the found discrepancies in the computed axial induced velocity has on the results, the value computed by HOST ($v_i = 11.4 \text{ m/s}$) has been directly prescribed to BEAT. The difference in collective pitch is reduced from 6% to 1% relative to the value computed by HOST. In addition both the tangential and axial aero-

Variable	BEAT	HOST
θ_0	6.13°	6.19°
θ_{1c}	0	0
θ_{1s}	0	0
β	1.61°	2.55°

Table 4.3: Pitch control inputs and flap angle at hovering flight considering the same axial induced velocity $v_i = 11.4 \text{ m/s}$

dynamic load distributions obtained by these two rotor analysis codes are represented by nearly identical curves (figure 4.8). On the other hand, the change in axial induced velocity does not have a strong effect on the flap angle computed by BEAT, which is considerably lower than the one computed by HOST. One of the possible causes of this difference is the fact that BEAT does not consider a blade precone angle. This means that when the helicopter is not operating, the absence of aerodynamic loads would entail that the blade drops due to the action of gravity. HOST assign a stiffness value to the flapping hinge in order to define an equilibrium state in this case (precone angle).

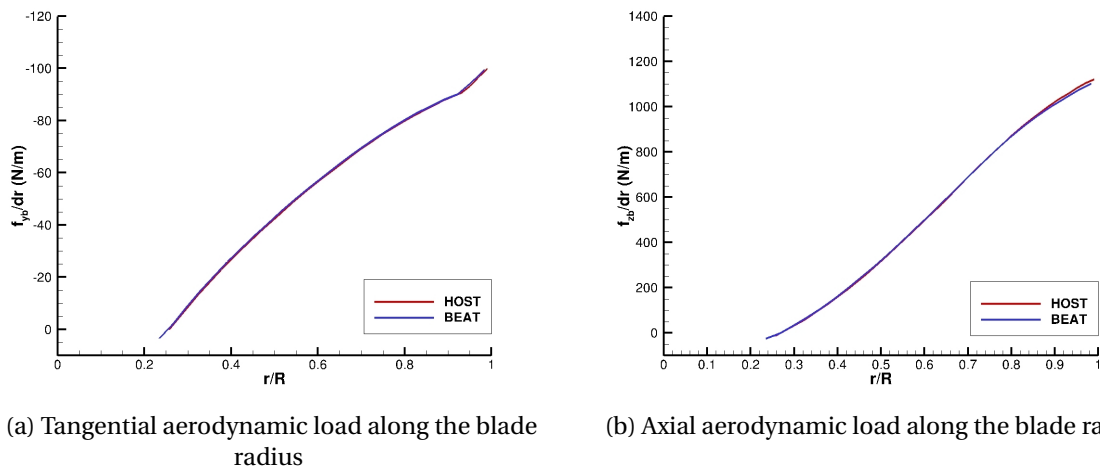


Figure 4.8: Aerodynamic load distribution in hover

4.3. FORWARD FLIGHT

In contrast to hovering flight, the flow velocity vector relative to each blade sectional element depends on the azimuth angle as well as on its radial position. The velocity that is experienced by the blade at the advancing side is higher than at the retreating blades. This difference increases with the flight speed and entails a dissymmetry of aerodynamic loads. In addition, BEAT computes the induced axial velocity at the rotor disk by means of a longitudinal linear static inflow model which accentuates the non-symmetrical flow pattern. In order to balance this dissymmetry and reach steady flight conditions, the swashplate has to be tilted by the pilot by the use of actuators. Therefore, both the lateral and the longitudinal cyclic pitch control angles have non-zero values.

4.3.1. EFFECT OF THE INPUT VARIABLES

SPATIAL DISCRETIZATION

In order to account for the non-symmetric flow pattern, not only the radial direction has to be discretized into n_r stations, but also the azimuthal direction into n_a elements. The influence that the number of elements used for both the radial and the azimuthal discretizations has on the computed pitch controls is displayed in figure 4.9a and figure 4.9b respectively for a forward flight speed of 40 m/s. Considering a relatively high number of azimuthal stations ($n_a=100$), BEAT does not require a minimum number of radial divisions to compute convergent solutions. Nevertheless, the accuracy of the solution is affected by the radial discretization. Hence, variations of 4% in collective control, 16% in lateral cyclic control and 46% in longitudinal cyclic control are noticed between the use of 1 and 25 radial stations. Regarding the azimuthal discretization, it is found that at least 6 stations are required to reach a convergent solution for 25 radial stations. While the collective pitch control remains practically unaffected, a variation of 13.6% in the lateral cyclic control and 2.4% in the longitudinal pitch control is observed between the use 6 and 100 azimuthal stations. Since the computation time required by BEAT is of the order of a few seconds, the subsequent analysis is carried out by discretizing the rotor disk into 25 radial stations and 100 azimuthal stations which, as it has been proven, are enough to obtain a convergent solution.

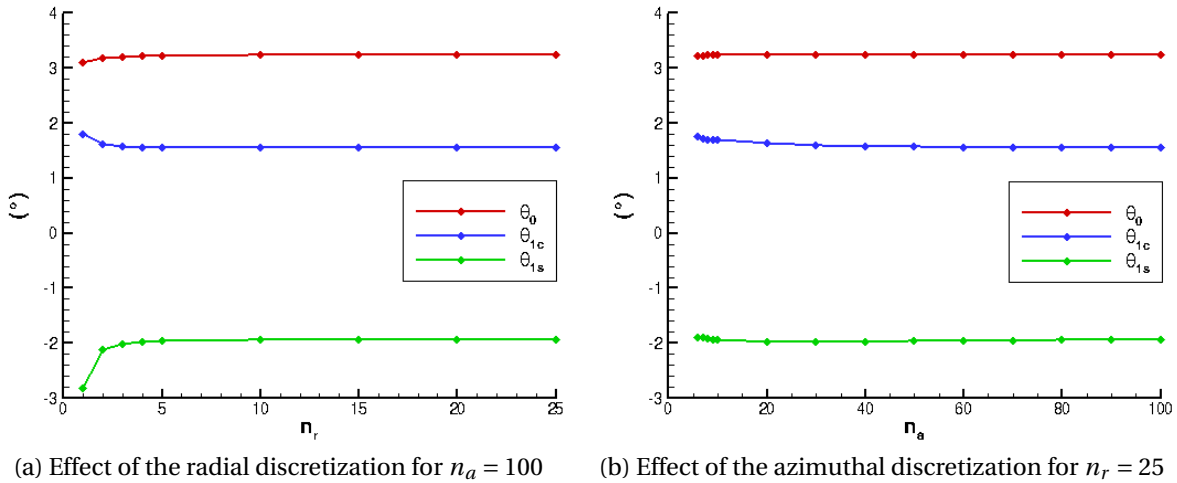


Figure 4.9: Effect of the spatial discretization in forward flight ($v_h = 40 \text{ m/s}$)

FORWARD FLIGHT VELOCITY

In forward flight, the flow velocity relative to the blade at the advancing side is higher than at the retreating side, reaching its maximum close to the tip at $\psi = 90^\circ$ and minimum in the vicinity to the blade root at $\psi = 270^\circ$ for a counterclockwise rotor. This fact entails an asymmetry in lift production over the rotor disk that increases as the flight velocity rises. In order to avoid the rotor to become uncontrollable, the swashplate is tilted by the pilot to trim the rotor. As it is displayed in figure 4.10, the longitudinal cyclic control value θ_{1s} becomes more negative with higher velocities. Thus, the effect that the high flow velocity at the advancing side has on the generated lift is balanced by means of reducing the blade pitch angle in this zone. In addition, the pitch angle (i.e. angle of attack) is increased at the retreating side. On the other hand, due to the longitudinal inflow model implemented

in BEAT, the axial induced velocity at $\psi = 0^\circ$ is higher than at $\psi = 180^\circ$, which results in lower sectional angles of attack in the rear part of the rotor. This difference in angles of attack between the front and the back parts of the rotor can cause undesirable pitching moments, hence a positive value of the lateral cyclic control θ_{1c} is required.

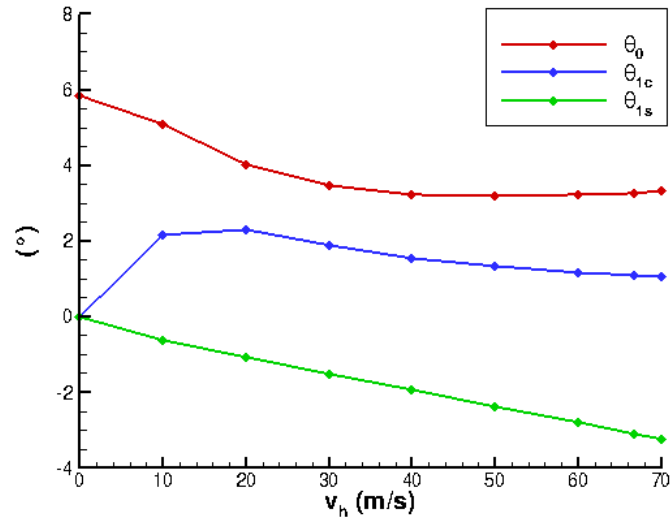


Figure 4.10: Pitch control angles for different flight velocities

4.3.2. COMPARISON WITH HOST RESULTS

The forward flight results obtained by BEAT and HOST are compared for three different flight speeds: low ($v_h = 20 \text{ m/s}$), intermediate ($v_h = 40 \text{ m/s}$) and maximum operational velocity $v_h = 66.7 \text{ m/s}$. The pitch control angles for the aforementioned flight configurations are displayed in table 4.4. The pitch controls determined by BEAT are in good agreement with those computed by HOST, where the relative error between them does not exceed 8% with respect to the HOST values. As it has been mentioned in the analysis of the hovering flight results, differences in the used inflow static model and the consideration of the rotor precone angle can be sources of discrepancies in the results computed by both rotor analysis codes.

	$v_h = 20 \text{ m/s}$		$v_h = 40 \text{ m/s}$		$v_h = 66.7 \text{ m/s}$	
	BEAT	HOST	BEAT	HOST	BEAT	HOST
θ_0 (°)	4.01	4.30	3.24	3.39	3.28	3.34
θ_{1c} (°)	2.31	2.18	1.55	1.57	1.12	1.21
θ_{1s} (°)	-1.07	-1.06	-1.93	-1.92	-3.07	-3.07

Table 4.4: Comparison of the pitch control angles computed by BEAT and HOST

The absence of the precone angle modeling in BEAT is noticeable in figure 4.11 where the blade flapping motion along the azimuthal position is plotted. It is observed that the flap angle distributions for each forward flight velocity obtained by BEAT and HOST show a nearly identical pattern but an offset is identified between both curves. As it has been found

for hovering flight, the flap angles computed by HOST are higher than the ones determined by BEAT as a consequence of the precone angle modeling.

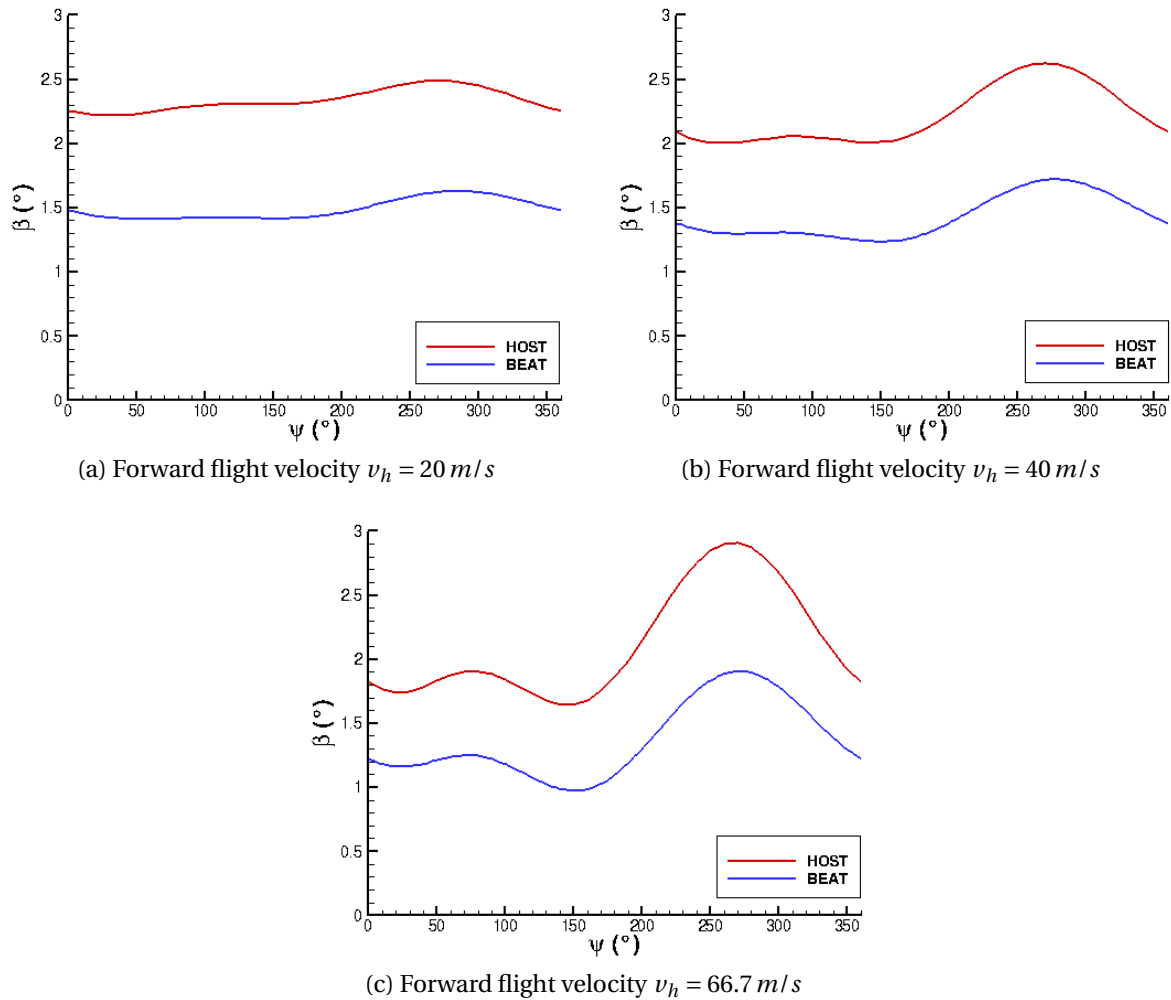
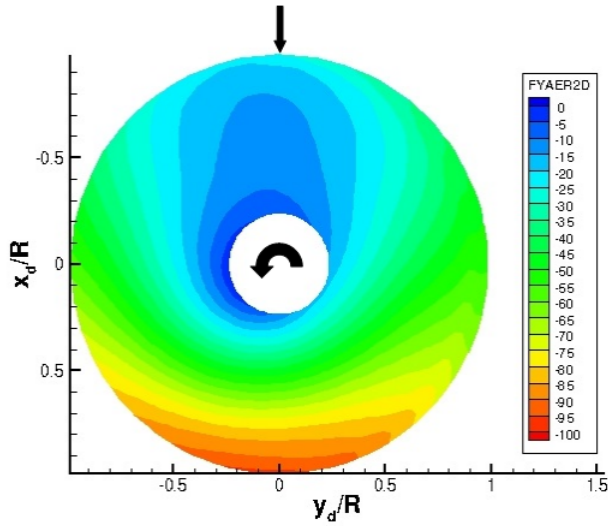
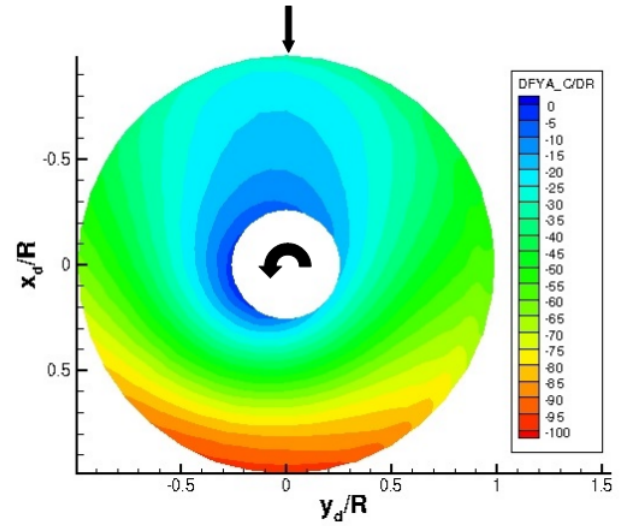


Figure 4.11: Comparison of the blade flapping distribution computed by BEAT and HOST

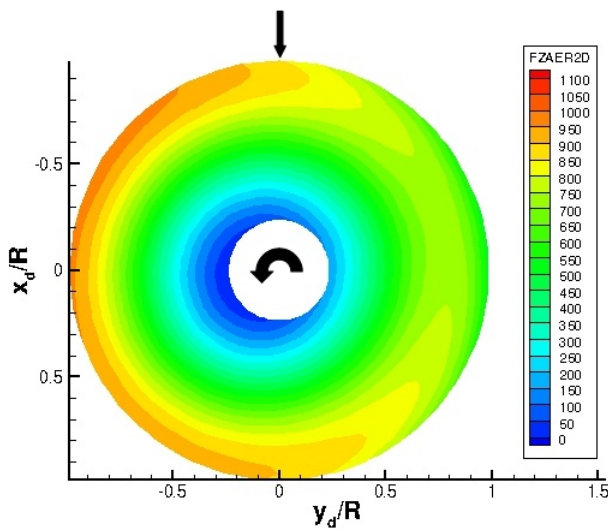
Finally, the plots of the tangential and axial aerodynamic load distributions over the rotor surface are presented in figures 4.12, 4.13 and 4.14 where the similarity of the output of BEAT and HOST can be observed. It can be seen that as the flight velocity increases, the reduction of the longitudinal cyclic control entail a noticeable decrease in lift at tip of the advancing blades which can even reach negative values (i.e. downward force).



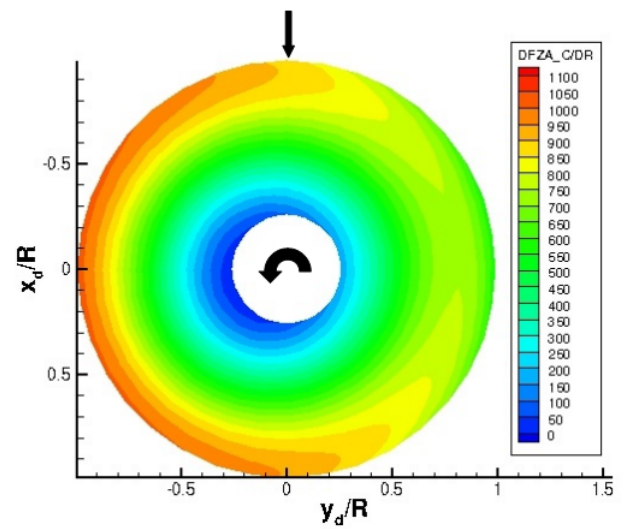
(a) Tangential aerodynamic load distribution f_{y_b}/dr (N/m) computed by BEAT



(b) Tangential aerodynamic load distribution f_{y_b}/dr (N/m) computed by HOST

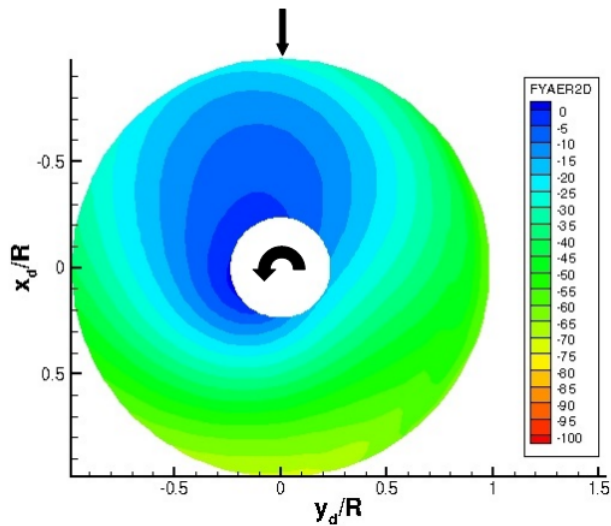


(c) Axial aerodynamic load distribution f_{z_b}/dr (N/m) computed by BEAT

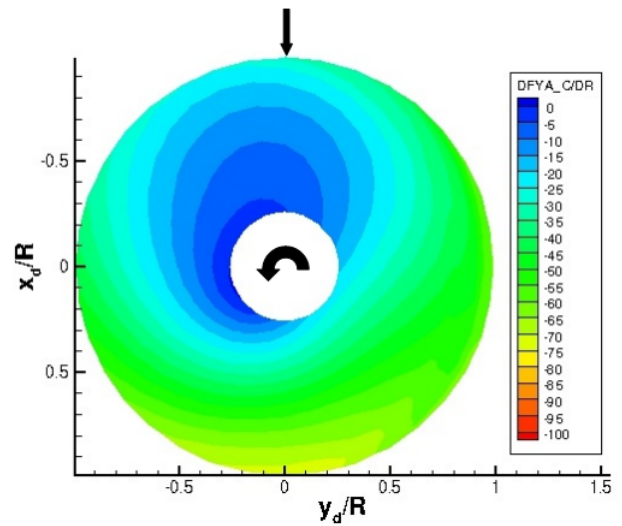


(d) Axial aerodynamic load distribution f_{z_b}/dr (N/m) computed by HOST

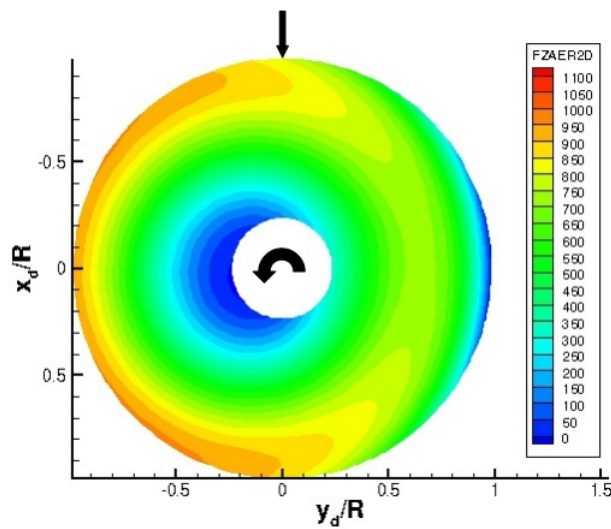
Figure 4.12: Comparison of the aerodynamic load distribution computed by BEAT and HOST for $v_h = 20$ m/s



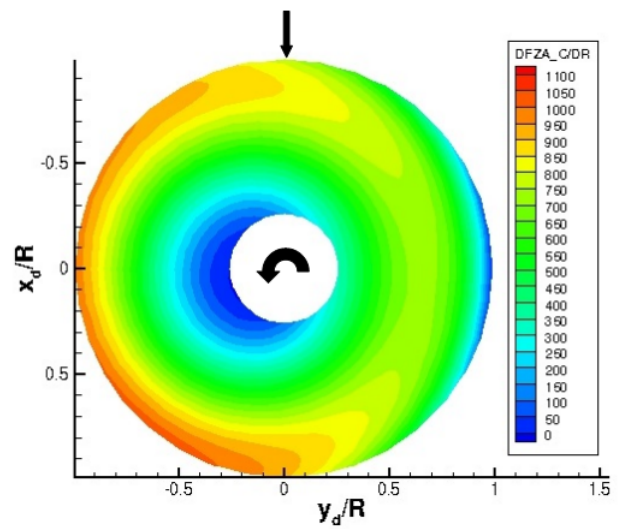
(a) Tangential aerodynamic load distribution f_{y_b}/dr (N/m) computed by BEAT



(b) Tangential aerodynamic load distribution f_{y_b}/dr (N/m) computed by HOST



(c) Axial aerodynamic load distribution f_{z_b}/dr (N/m) computed by BEAT



(d) Axial aerodynamic load distribution f_{z_b}/dr (N/m) computed by HOST

Figure 4.13: Comparison of the aerodynamic load distribution computed by BEAT and HOST for $v_h = 40$ m/s

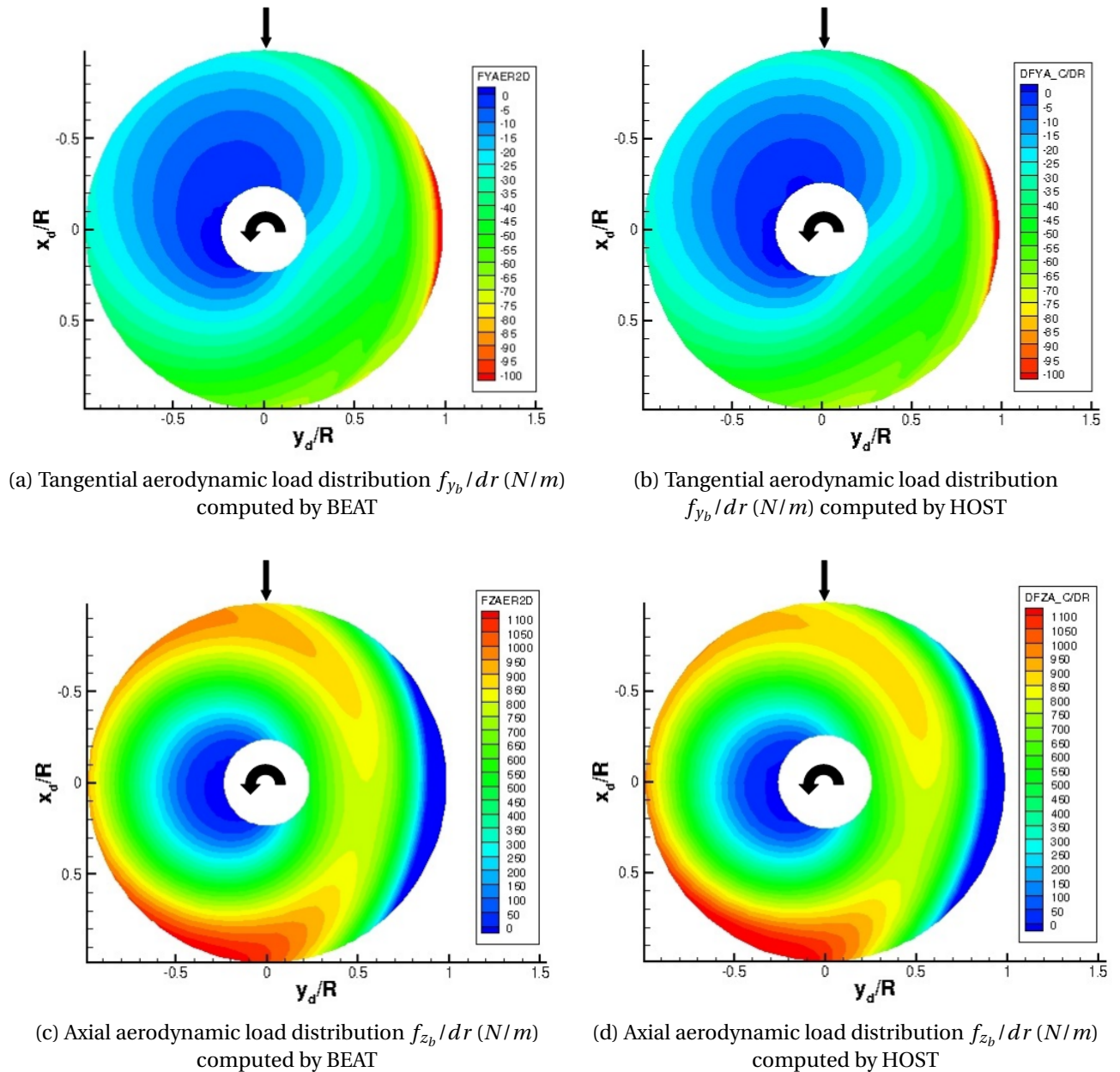


Figure 4.14: Comparison of the aerodynamic load distribution computed by BEAT and HOST for $v_h = 66.7$ m/s

4.4. ANALYSIS OVERVIEW

The verification analysis carried out in this chapter shows that the results computed by BEAT are coherent and consistent with its associated modeling assumptions. In addition, it has been shown that the outcomes determined by BEAT are in good agreement with those obtained by HOST. Differences in the used static inflow model and the precone angle modeling are regarded as possible sources of the slight discrepancies of the results computed by both rotor analysis codes.

Despite the successful verification of the tool, the degree to which the actual performance of helicopter rotors is captured by BEAT is unknown yet. Hence, the results ob-

tained after each aerodynamic analysis can be quite accurate according to the equations which model the reality, but however it may not be very similar to the data which is obtained experimentally.

5

THE CFD FLOW SOLVER TAU

This chapter gives an overview of the CFD solver TAU [41] with particular emphasis on the main functionalities employed during its coupling with BEAT addressed in the subsequent chapters. The TAU code is optimized to be run in parallel computers and solves the three dimensional Reynolds-averaged Navier-Stokes equations on unstructured grids. The physical domain can be discretized by means of hybrid meshes, which enable the combination of structured and unstructured grid blocks. Spatial discretization of both complex geometries and bodies in motion is facilitated by the use of overset grids and convergence acceleration techniques such as multigrid methods are implemented. A correct definition of the boundary conditions is required for an accurate modeling of the case in which the flow pattern is simulated. Among them, special attention is paid to the actuator disk boundary which is developed for propellers and helicopter rotors modeling.

5.1. SPATIAL DISCRETIZATION

The physical domain of the flow which needs to be computed by applying the governing equations must be discretized. To do so, the domain is divided into geometrical elements called grid cells, whose distribution has to fulfill the following requirements [67]:

- The computational domain is entirely covered by the grid.
- There is no gap between grid cells.
- There is no overlapping between grid cells.

In addition, regularity should be a factor to be taken into consideration at the grid generation stage. Abrupt changes in volume and shape of the elements should be avoided as much as possible.

TAU does not contain a grid generator, thus, to set up the grid configuration the use of third-party software such as Pointwise or Centaur is necessary. The input grid can be composed of polyhedral elements with both triangular and quadrilateral surfaces. In the case of a quadrilateral surface, the corner points defining its geometry do not have to be contained in the same plane. The use of hexahedral and prismatic elements is suited for the modeling of the close vicinity of walls for accurate resolution of boundary layers. These elements can be highly stretched and allow the computation of the flow pattern in the three space

directions according to the different length scales in the boundary layer, so gradients are efficiently determined [68]. Tetrahedral elements are used in regions where the flow needs to be isentropically computed and, in addition, they add the advantage of a more flexible modeling of complex geometries compared to hexahedra and prisms. In the transition region between tetrahedral and hexahedral elements, pyramidal elements are employed.

The Navier-Stokes equations are computed over the discretized domain by TAU, which is a finite volume solver. At the preprocessing stage, the control volumes at which the conservation equations are evaluated are defined. These control volumes compose the so-called secondary grid which is computed from the primary grid data. TAU includes two different approaches to define the arrangement of the secondary grid control volumes:

- **Cell Vertex grid metric:** the flow variables are associated with the vertices or nodes of the primary grid, around which the control volumes are defined. These elements are constructed by linking the centers of the primary grid elements with the midpoints of the adjacent faces.
- **Cell Centered grid metric:** the flow variables are associated with the centers of each primary grid cell which are assumed to be located at the barycenter. Therefore, both primary and secondary grids share identical volumes in the physical domain.

Despite both schemes are available, the Cell Vertex approach is typically the preferred option due to its higher robustness and accuracy [69]. In addition, this scheme has been implemented in TAU from its early development stages, while the Cell Centered strategy was included in the last years and is not fully developed yet. In the present work, the Cell Vertex approach is applied by the preprocessor to define the control volumes contained in the secondary grid which is dual to the primary grid. The preprocessor needs to be run once for the input primary grid and it computes all grid information required by the flow solver. Figure 5.1 displays both the primary (black lines) and secondary (red lines) two-dimensional grids about an airfoil geometry.

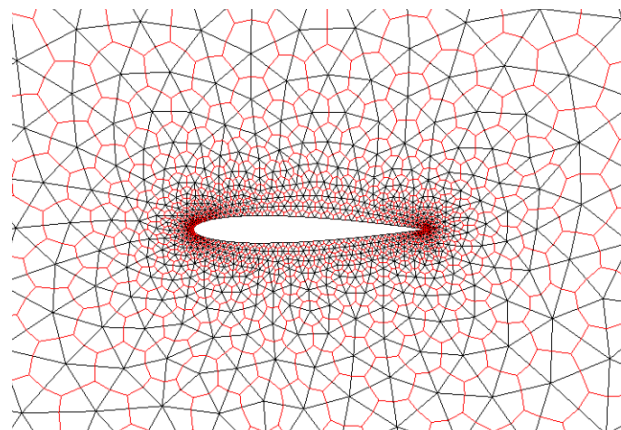


Figure 5.1: Primary and secondary grids about a NACA 0012 airfoil [70]

5.2. PARTITIONING/PARALLELIZATION

Parallel computing [71–73] enables the reduction of the wall-clock time associated with a numerical simulation by means of executing the TAU flow solver in multiple processors.

For a given number of N processors, the computational grid is partitioned into N subgrids. Each of the processors carry out the calculations on one of the subdomains and information is continuously exchanged between neighboring subdomains since the solution on those depends on each other. The way that the domain is decomposed determines the performance of the parallelization scheme, hence, in order to use effectively a parallel system the data must be equally distributed among the processors so the assigned computations can be completed at the same time in subdomain.

Along the partitioning process each point of the computational grid is assigned exclusively to one subdomain. On the other hand, the data associated with the grid points of neighboring subdomains connected by edges which are cut along the partitioning stage are also stored by each subdomain. These additional points, also known as ghost points, are not owned by the subdomain but are assigned to it. Due to the fact that part of the connectivity data is stored in more than one subdomain, the memory requirement rises compared to a single domain approach. The relative memory overhead depends on the ratio of the additional points located at the subdomain interfaces to the total grid points. Therefore, the decomposition of a small grid (low number of points) into a number of N subgrids entails a greater relative memory overhead than if a large grid is divided into the same number of partitions.

During the flow integration on the computational grid, data must be exchanged among the subdomains. By using Message Passing Interface (MPI), communication between owned and additional points at each partition is established.

Partitioning can be performed by TAU by using any of the three available grid partitioners. The user can choose between the self-coded partitioner TAU private and the open-source software packages Zoltan and Chaco. The resulting memory overhead and, thus, the quality of the partition, depends on the used algorithm. For massive parallel computations both Zoltan and Chaco offer better performance, while when the computational domain is decomposed into a low number of partitions, the greater memory overhead associated with the self-coded partitioner TAU private is compensated by the fact that the partitioning itself is considerably faster.

The TAU private partitioner is a recursive coordinate bisection algorithm, which computes the subdomain interfaces according to coordinates. If the computational domain needs to be divided into two parts, three different planes are analyzed $x = constant$, $y = constant$, and $z = constant$, where the constant value denotes the mean value between x_{min} and x_{max} , y_{min} and y_{max} , and z_{min} and z_{max} respectively. The domain is partitioned by the plane which cut the lowest number of grid edges in order to reduce the number of additional points and its associated memory overhead. On the other hand, if the computational domain needs to be divided in three parts, initially it is decomposed into two subdomains weighted with $1/3$ and $2/3$, and subsequently the second domain is partitioned into two partitions with equal weights. Thus, following the two aforementioned algorithms any grid can be partitioned into a number of N subdomains. For example, 5 subdomains can be defined by dividing the domain into two parts weighted with $2/5$ and $3/5$, where the first one is decomposed into two partitions and the second one into three partitions.

5.3. CHIMERA METHOD

The use of overset grids, commonly denominated as the Chimera technique [12] is also available in TAU. This approach is considered as a domain decomposition method, which

enables the modeling of the computational domain by two or more grids independently generated. Among each grid structure, an overlap region where the spatial domain is discretized by both grids is required for the information transfer and interpolation of the flow solution. By means of this domain decomposition technique, complex geometries can be modeled thoroughly by grids that are embedded within a background grid. Moreover, one of the main advantages associated with the Chimera method is the fact that it enables the relative motion of a grid with respect to the others without the need of remeshing. Thus, for rotorcraft simulations it is a very powerful strategy. Fuselage and rotor grids can be individually defined and the rotor grid can rotate as the blades do with respect to the fuselage grid [74].

The implementation of overset grids can be divided into three main steps: grid generation, hole cutting and solution interpolation [75].

- Initially, a background grid and the particular grid associated with the body geometry that needs to be modeled differently must be created. Usually, the spatial domain covered by the latter one is fully contained in the background grid.
- Subsequently, as the small grid is embedded within the background grid, the points of the background grid located inside the smaller grid are deleted in order to avoid unnecessary calculations, this action is defined as hole cutting. Nevertheless, not all the points of the background mesh covered by the smaller one must be eliminated since an overlap region between both grids is required for the exchange of information. In order to enable an efficient transfer between the aforementioned subdomains the cells of both grids in the overlap region should have similar dimensions. In addition, as a rule of thumb for the correct definition of the overlap region dimensions, a minimum space of three cells should be respected to confine the width of this region. Thus, the overlap zone is delimited by an inner and an outer boundary.
- Finally, the solution at both boundaries is interpolated between each subdomain.

Nevertheless, some disadvantages are also linked to the use of the Chimera approach. Numerical errors can arise from the interpolation of the information to be transferred. Furthermore, the fact that an overlap region must exist between grids entails that the flow equations solution is computed twice, which increases the required computational time.

A two-dimensional case where the Chimera method is applied is shown in figure 5.2. Figure 5.2a displays the two-dimensional Cartesian grids that define the spatial discretization of the problem. The small grid, colored in red, is fully contained in a background grid, colored in black. As it can be seen in figure 5.2b, after performing the hole cutting stage, the overlap region is delimited by two boundaries, an inner boundary defined by the hole made at the background grid and a outer boundary confined by the small grid limits. If the discretization is extended to a three-dimensional case, the Chimera technique can be used by conducting the same procedure as for two-dimensional cases.

5.4. FLOW SOLVER

The flow solution is computed by means of the application of the three-dimensional RANS equations over the dual grid cells whose arrangement is determined by the preprocessor from the initial primary grid (section 5.1). The Navier-Stokes equations addresses the flow

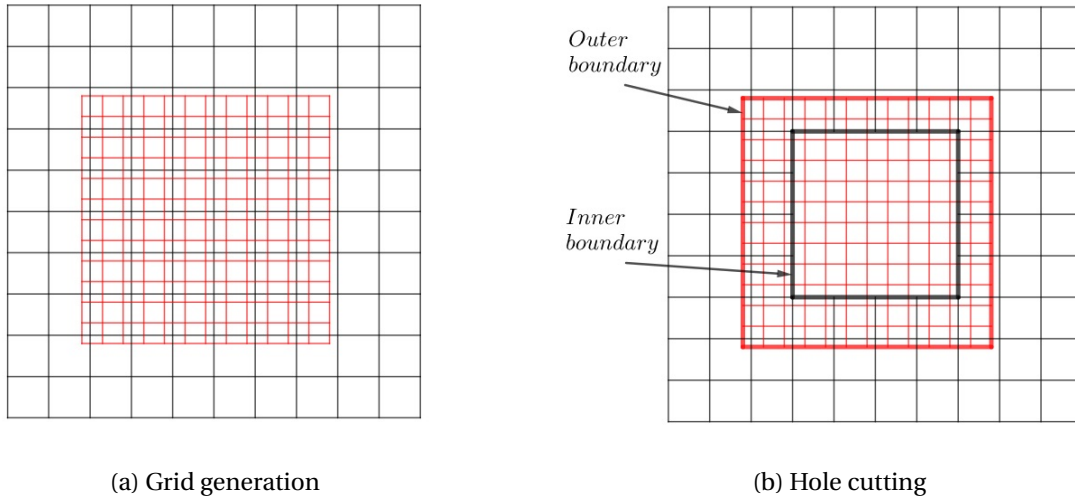


Figure 5.2: Chimera technique scheme

motion by imposing the conservation of mass, momentum along the three physical directions, and energy in a control volume V_c . These governing equations can be written as:

$$\frac{\partial}{\partial t} \int_{V_c} \mathbf{W} dV_c = - \int_{\partial V_c} \mathbf{F} \cdot \mathbf{n} dS \quad (5.1)$$

where \mathbf{W} is a vector of five components which stores the conservative flow variables and \mathbf{F} represents the fluxes through the control volume boundaries ∂V_c whose outer normal vector is defined by \mathbf{n} . Therefore, changes in the flow conservative variables can be assessed by evaluating the fluxes over the considered control volume boundaries. The computation of fluxes can be carried out by TAU by the use of either upwind or central schemes, at which artificial dissipation models are implemented in order to improve its stability.

The flow governing equations are evaluated in time towards the steady state solution. Two time-stepping algorithms can be chosen by the user: an explicit Runge-Kutta method and an implicit backward Euler method. Since the spatial discretization of the computational domain is not affected by this decision, the use of one or the other time-stepping scheme has an effect on the convergence of the solution while the converged solution remains unaltered. The temporal variation of the conservative flow variables in a control volume can be expressed as:

$$\frac{\partial(\mathbf{W}V_c)}{\partial t} + \mathbf{R} = 0 \quad (5.2)$$

where \mathbf{R} denotes the residual which must tend to zero for steady state simulations. In order to speed up the convergence towards the steady state solution some acceleration techniques are implemented in TAU such as multigrid methods (section 5.5), residual smoothing and local time-stepping schemes.

The turbulent behavior of the flow is modeled by the use of turbulence models. Several turbulence models are available in TAU ranging from one (Spalart and Allmaras) and two ($k - \omega$) transport equations eddy viscosity models to the more advanced Reynolds stress transport models.

5.5. MULTIGRID METHODS

The convergence of the numerical simulations can be accelerated by means of the use of multigrid methods which are implemented in TAU. The computational time required to reach a steady state solution can be reduced by solving the flow governing equations on coarser grid elements that are defined from the secondary or dual grid arrangement. According to Blazek [67], the improvement of the convergence performance associated with this strategy is mainly subjected to two ideas:

- Due to the larger volume of the coarser grid elements, the local time step can be increased. In addition, the numerical complexity of the algebraic system is reduced compared to the fine grid case. Both facts enable the solver to enhance the convergence speed and reduce the computational time.
- While the high-frequency (i.e. small wave length) solution errors are rapidly reduced by the iterative solver, the low-frequency (i.e. large wave length) errors are damped at slower rates. This entails that when the high-frequency errors are neutralized along the initial iteration steps, the convergence speed slows down remarkably. Nevertheless, at coarser grid levels the low-frequency errors at finer grid levels are seen as high-frequency components. Therefore, wave lengths errors can be damped quicker by projecting them on coarser grid levels and the solver convergence is speed up.

The coarser multigrid levels are generated from the dual grid structure by the application of agglomeration algorithms [76, 77]. The fine grid control volumes are fused together forming the elements which define the next coarser multigrid level. Each grid contains all the information required by the solver to perform the computations of the governing equations on it. It must be taken into account that the agglomeration approach can entail the formation of irregularly shaped control volumes at the coarser multigrid levels, thus, these algorithms are modified in order to preserve some topological aspects of the dual grid at the coarser levels.

After defining the grid levels, the information obtained by applying the flow conservation equations on each level is exchanged among them. The transfer from a finer to a coarser level is called restriction, while prolongation refers to the transfer from coarser to finer levels. The number of grid levels and the multigrid cycle to be used by the solver are specified by the user before running the simulation. The chosen cycle defines the sequence of restriction and prolongation operations between levels. Two multigrid cycles are implemented in TAU, the V-cycle and W-cycle, whose schemes for four grid levels are displayed in figure 5.3, where h denotes the finest grid in reference to its grid spacing.

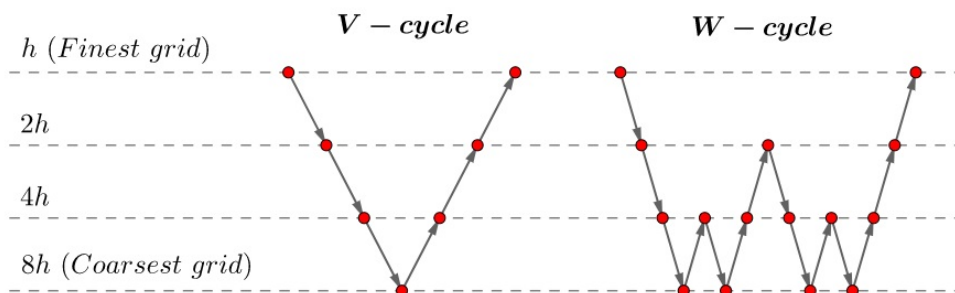


Figure 5.3: Multigrid cycles implemented in TAU

Regarding the V-cycle (figure 5.4), the solution \mathbf{W}_h and residual \mathbf{R}_h of the flow governing equations is computed initially on the finest grid. It has to be pointed that in case that the starting grid is not the finest one, the solution is interpolated to the successive finer grid levels until the finest level. Subsequently, the solution is transferred to the following coarser level \mathbf{W}_{2h} (restriction) by applying interpolation. In addition, the residual is also interpolated to the coarser level \mathbf{R}_{2h} in order to reduce the low-frequency residual component. The solution is computed on each grid level following the same iterative procedure as on the finest grid. Once that both the solution \mathbf{W}_{8h} and residual \mathbf{R}_{8h} are obtained at the coarsest level, the solution is corrected from the coarser to the finer levels (prolongation) by means of interpolation until reaching the improved solution \mathbf{W}_h^+ and residual \mathbf{R}_h^+ on the secondary or dual grid.

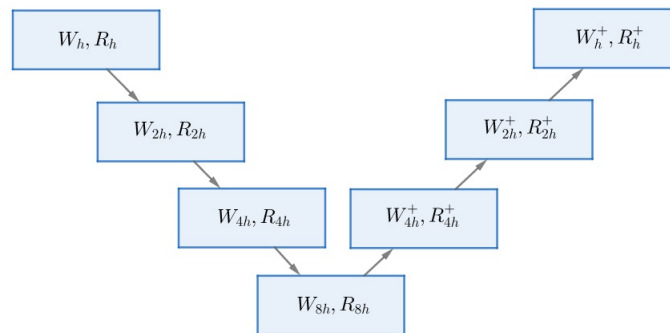


Figure 5.4: V-cycle scheme

5.6. BOUNDARY CONDITIONS

An accurate modeling of the physical domain to be analyzed requires a correct use of boundary conditions which can affect significantly both the quality and stability of the solution. A wrong definition of the boundary conditions can yield to nonphysical flow patterns and can entail either overdetermined or underdetermined equation systems to be solved. All the information concerning the definition of the boundary conditions required by the flow solver must be specified by the user in a boundary mapping file before running any simulation. In this section, only the boundary conditions applied in the subsequent simulations are addressed: farfield, viscous wall (helicopter fuselage), and actuator disk (helicopter rotor).

- The farfield boundary condition can be regarded as an artificial boundary condition. When the flow about a body is simulated the infinite physical domain can not fully modeled, thus, the computational domain represents a truncated region of it. The definition of the external boundaries of the computational domain must be defined with the aim of avoiding as much as possible the disturbance effects on the solution that arise from the aforementioned truncation.
- The viscous wall boundary condition imposes that over a surface viscous effects are considered. Besides the fact that the flow can not go through the wall, the viscous wall condition considers that the flow velocity along the surface is equal to zero (no-slip condition).

$$\mathbf{v} \cdot \mathbf{n}|_{wall} = 0 \quad (5.3)$$

$$\mathbf{v}|_{viscous\ wall} = 0 \quad (5.4)$$

- The modeling of rotors is simplified by the use of the actuator disk boundary condition. From a prescribed load distribution over its surface, a jump in both pressure and tangential velocity is imposed to the flow which goes through it. Due to its great importance in this project, a more thorough description is offered in section 5.7.

5.7. ACTUATOR DISK MODULE

TAU has a module based on the actuator disk principles which allows to replace the helicopter rotor by a stationary geometrical simpler model. The actuator disk is responsible for applying equivalent stationary forces to the fluid while producing a discontinuity in pressure and tangential velocity across it.

The fact that the helicopter rotor is modeled as an actuator disk of zero thickness has to be taken into account for its discretization as it is explained by Schweikhard [78]. Since the flow deals with a jump both in pressure and tangential velocity through the actuator disk, the grid points on both sides of the disk store different information in spite of being at the same location as it can be seen in figure 5.5. This means that each pair of points are geometrical identical but topological different, with the exception of the border points which are both geometrical and topological identical. Therefore, the flow is simulated by applying the equations of conservation of mass, momentum and energy to a control volume which contains the discretized disk where the loads are applied as source terms.

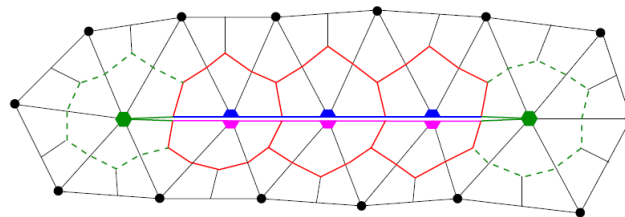


Figure 5.5: Grid section through the disk [79]

The blades of a helicopter rotor generate forces which vary along the radius and azimuth angle. Consequently, reaction forces act on the flow which goes through the rotor and increase its momentum and energy. Hence, the rotor is modeled as an equivalent stationary load surface distribution obtained by integrating the forces produced by each blade element and time averaging. To do so, Axel Reichle [80], the developer of the module at DLR, assuming that the circumferential extension of the blade is considerably smaller than the radial extension, indicates that the rotor geometry can be simplified by replacing each blade with a rotating line. Thus, the actuator disk is defined by rotating lines. The values of the force along each rotating line have to be computed previously, in this thesis, the blade element theory is chosen to carry out this task. If no forces along the rotating lines are specified, the actuator disk tool will not produce any force acting on the flow and the flow will not experience any change when goes through the modeled surface.

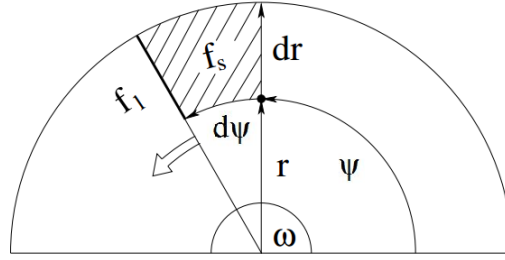


Figure 5.6: Force distribution over the actuator disk [80]

The force distribution surface is obtained by integrating the forces associated with the rotating lines. Figure 5.6, represents a rotating line whose rotational velocity ω is equal to the rotor angular velocity. At the position defined by the azimuth angle ψ and the radial component r , the normal force f_r acts along dr during an infinitesimal amount of time dt . Therefore, during the period dt , the rotating line covers an angle $d\psi = \omega dt$, which means that the aforementioned force f_r acts over a surface $dS = r dr d\psi$. Taking into account that the helicopter rotor has a number of n blades, it can be stated that f_r acts on a surface dS during a period of time of ndt while during $T - ndt$ nothing happens, where T is the rotation period of the rotor and it is equal to $2\pi/\omega$. The line force f_r produces a momentum equal to $f_r dr dt$, and hence, the equivalent surface force f_s can be computed according to (5.5) and (5.6).

$$f_s dS = n \frac{f_r dr dt}{T} = f_r n \frac{r dr d\psi}{2\pi r} = f_r \frac{n}{2\pi r} dS \quad (5.5)$$

$$f_s = f_r \frac{n}{2\pi} \int_S \frac{1}{r} dS \quad (5.6)$$

The fact that the force distribution surface or actuator disk has no thickness is the cause of the pressure jump between both sides of the disk. This difference in pressure produces an axial force obtained by the application of conservation of momentum over a control volume which contains the modeled rotor. Therefore, due to the effect of the axial force on the flow, the axial velocity rises continuously. Nevertheless, there is no influence of the resultant axial force over the swirl or tangential velocity of the flow. Since the tangential velocity component is so significant that it should not be avoided, a discontinuity in rotational velocity through the disk is modeled. The computation of the variation of tangential velocity is carried out by the application of the conservation of momentum equation in tangential direction in each cell as it is indicated by (5.7). Hence the jump in flow tangential velocity imposed by the actuator disk is computed from the prescribed tangential load on each grid element of its surface.

$$f_t = \dot{m} \Delta v_t \quad (5.7)$$

5.8. OVERVIEW

In the following chapters, CFD simulations in TAU are performed to analyze the performance of helicopter rotors modeled by means of the actuator disk approach. The domain is decomposed in multiple subdomains and the computations are carried out in a parallel computer.

6

COUPLING BETWEEN BEAT AND TAU

This chapter focuses on the iterative coupling process that is carried out between BEAT and TAU. The helicopter rotor is modeled in TAU by means of an actuator disk which accounts for the prescribed axial and tangential aerodynamic load distributions by imposing to the flow that goes through it both pressure and tangential velocity jumps. The main idea of this coupling strategy is that the velocities captured at the grid points of the actuator disk after each simulation performed by TAU are transferred to BEAT, which computes an updated aerodynamic load distribution. The performance and the limitations of this approach are analyzed for hovering and forward flight conditions. The considered helicopter rotor is the scaled version of the Bo 105 described in Chapter 4 with zero shaft angle. In order to assess exclusively the proper functioning of the coupling, the rotor is simulated in isolated conditions, hence, possible interference effects between other helicopter components are not addressed.

6.1. COUPLING DEFINITION

The coupling between BEAT and TAU aims to establish dependency relations among both codes. The TAU actuator disk boundary is employed to model the helicopter rotor geometry and is responsible for the application of the aerodynamic loads that act on it to the fluid. On the other hand, BEAT computes the aerodynamic loads on the rotor blades by means of the blade element theory from the velocity field extracted over the actuator disk surface of TAU. The transfer of loads from BEAT to TAU and velocities from TAU to BEAT define a feedback process whose scheme is displayed in figure 6.1. One of the limitations of this approach is the fact that despite the flapping motion of the rotor blades, the helicopter rotor is modeled by a porous planar surface in TAU. Therefore, the orientation of the actuator disk is determined by the rotor shaft angle. Further research is carried out at DLR to enable the deformation of the actuator disk in order to account for the blade flapping motion.

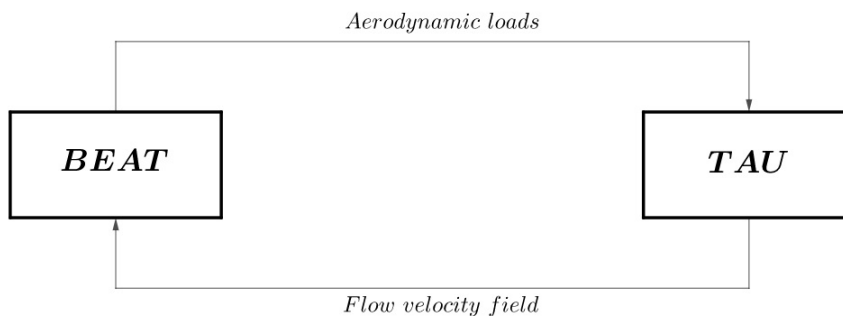


Figure 6.1: Coupling diagram

The tangential and axial aerodynamic loads are computed by BEAT at the center point of each of discretized rotor disk stations. In order to ease the transfer of information and to avoid interpolation errors, it is convenient to extract the velocities obtained at the end of each TAU simulation at the same geometrical points. As it is described in the previous chapter, TAU includes two different approaches to define the arrangement of the secondary grid and, thus, the locations at which the flow variables are determined: Cell Vertex and Cell Centered grid metrics. Due to its better performance features, in this work the Cell Vertex strategy is used, which means that the flow variables are associated with the nodes of the input or primary grid. Therefore, the actuator disk grid is defined in a way that its vertices are located at the points where BEAT computes the blade aerodynamic loads. This discretization approach is displayed in figure 6.2, where the primary grid is colored in black while the secondary grid is colored in red. In this case, the primary grid is adapted to perform the aerodynamic analysis in BEAT at three radial and four azimuthal stations (i.e. twelve stations). It has to be noted that the inner and outer grid points are not located at the radial position of the start of the profiled part r_p and the tip R respectively. The location of the inner r_i and outer r_o grid vertices is defined by:

$$r_i = r_p + \frac{\Delta r}{2} \quad (6.1)$$

$$r_o = R - \frac{\Delta r}{2} \quad (6.2)$$

where Δr denotes the distance between two consecutive radial stations which is a constant due to the uniform spatial discretization technique implemented in BEAT.

After carrying out each flow simulation in TAU, the three-dimensional velocity components are extracted at the actuator disk primary grid points and are transferred to BEAT to initialize a next coupling step. The extracted velocity values are expressed in the rotor disk reference system and can be projected onto a local blade reference system by:

$$v_{x_b TAU} = v_{x_d TAU} \cos \psi + v_{y_d TAU} \sin \psi \quad (6.3)$$

$$v_{y_b TAU} = -v_{x_d TAU} \sin \psi + v_{y_d TAU} \cos \psi \quad (6.4)$$

$$v_{z_b TAU} = v_{z_d TAU} \quad (6.5)$$

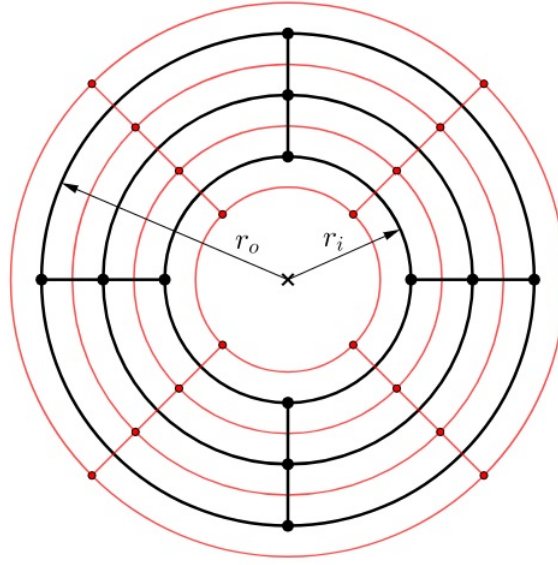


Figure 6.2: Rotor disk discretization

where v_{x_bTAU} , v_{y_bTAU} and v_{z_bTAU} represent the radial, tangential and axial flow velocity components respectively with respect to a non-rotating blade. It has to be taken into account that despite of being at the same location, the grid points on both sides of the disk store different information. Thus, the tangential velocity component transferred to BEAT is computed as the mean value of the upper and the lower sides, while the axial and radial velocity components are taken directly from the upper side. In practice, the axial and radial velocity components can also be extracted at the lower side without altering their value. This is due to the fact that the actuator disk boundary is implemented in TAU by following a source term formulation.

The actuator disk can be regarded as a porous surface which imposes steady loads to the flow that goes through it. Hence, the blades are not modeled and the effect of their motion is only contained in the prescribed aerodynamic loads. Once that the velocity components are extracted and transferred to BEAT, the tangential and axial components are corrected in order to account for the blade motion according to:

$$v_{y_bBEAT} = v_{y_bTAU} - \Omega r \quad (6.6)$$

$$v_{z_bBEAT} = v_{z_bTAU} - v_{x_bTAU} \sin \beta - \dot{\beta}(r - e) \quad (6.7)$$

while the radial velocity component does not need to be computed to perform the two-dimensional aerodynamic analysis at each blade sectional element.

From the corrected tangential and axial flow velocity components relative to the blade, the corresponding aerodynamic forces are computed by BEAT. The load distribution is written into an output file with the format shown in table 6.1 that is subsequently read by TAU which prescribes the tangential and axial load components to the associated primary grid points.

ψ	r/R	f_{y_b}/dr	f_{z_b}/dr
ψ_1	r_1/R	$f_{y_b1,1}/dr$	$f_{z_b1,1}/dr$
ψ_1	r_2/R	$f_{y_b1,2}/dr$	$f_{z_b1,2}/dr$
.....			
ψ_1	r_{n_r}/R	$f_{y_b1,n_r}/dr$	$f_{z_b1,n_r}/dr$
ψ_2	r_1/R	$f_{y_b2,1}/dr$	$f_{z_b2,1}/dr$
ψ_2	r_2/R	$f_{y_b2,2}/dr$	$f_{z_b2,2}/dr$
.....			
ψ_{n_a}	r_{n_r}/R	$f_{y_b n_a, n_r}/dr$	$f_{z_b n_a, n_r}/dr$

Table 6.1: Aerodynamic loads prescription output file

6.2. GRID

The spatial discretization of the physical domain is carried out by means of a hybrid grid for hover analysis, while an unstructured grid is used for forward flight simulations of the isolated rotor. Since TAU does not contain a grid generator, both grids are created with Pointwise. The farfield boundary is modeled as a sphere with a radius 100 times the rotor radius. The selected rotor disk spatial discretization in BEAT consists of 25 radial and 100 azimuthal uniformly distributed stations, which in TAU is represented by 2400 quadrilateral elements at both sides of the actuator disk. In the unstructured grid used for forward flight computations, the actuator disk is surrounded by tetrahedral elements whose size becomes larger with the distance to the disk. Pyramidal elements are employed to transition from the quadrilateral surfaces which model the actuator disk to the triangular faces of the tetrahedral elements. On the other hand, in the hybrid grid used for hovering flight analysis, the spatial domain located just behind the actuator disk is discretized by means of hexahedral elements whose size also increases with the distance to the disk. The structured grid is chosen to enable a better resolution of the rotor wake, whose influence on the rotor aerodynamics is higher than in forward flight due to the small velocities. In addition, this difference in grid arrangement between both cases allows for a better capture of flow recirculation zones.

	Hovering flight	Forward flight
Number of points	5,234,220	807,539
Number of elements	11,174,720	4,809,269
Number of tetrahedra	7,010,320	4,804,469
Number of pyramids	174,400	4,800
Number of hexahedra	3,990,000	0

Table 6.2: Grid characteristics

6.3. SIMULATION SET UP

The simulations of the present work are run on the DLR $C^2A^2S^2E-2$ cluster which is a 560 nodes parallel computer where each node has two Intel Ivy-Bridge (12-Core) processors. The computational grid is partitioned into 48 subdomains by the use of the TAU private grid

partitioner. A central scheme with a matrix artificial dissipation model is employed for the computation of the fluxes. An implicit backward Euler time-stepping method is selected to evaluate the governing equations in time. The use of implicit time-stepping schemes enables the use of larger time step sizes than in explicit algorithms, which can increase the convergence speed although its stability can be worsened. Since implicit time-stepping methods do not have to fulfill the Courant-Friedrichs-Lewy (CFL) condition, which states that the chosen time step should be equal or lower than the time at which flow information travels between neighboring grid elements, a CFL number equal to 5 is chosen to perform all the computations. The flow turbulence is modeled by means of a $k - \omega$ eddy viscosity model.

In the hovering flight TAU simulations, the initial velocity at the farfield boundaries is set to zero. However, due to the effect that the prescribed loads at the actuator disk surface have on the flow, air motion is induced. Preconditioning algorithms [81] are implemented in TAU with the aim of improve the solution convergence at low flow speed cases where the Mach number tends to zero. However, the multigrid acceleration algorithms included in TAU are not robust at this flight conditions. Thus, the flow governing equations are evaluated uniquely on the fine secondary grid cells.

On the other hand, the forward flight simulations are initialized with a prescribed non-zero velocity field at the farfield boundaries. In this case, the use of multigrid techniques is a suitable and robust strategy to improve the convergence rate. A V-cycle with three multigrid levels is used for this purpose.

6.4. ANALYSIS OF RESULTS

In this section the analysis of the performance and limitations of the coupling strategy are addressed. The scaled version of the Bo 105 rotor is tested in isolated conditions for hovering and forward flight cases.

6.4.1. HOVER

Initially, the first hovering flight coupling simulation is run for a large number of time steps in order to assess its convergence and estimate how it would be in the next coupling steps. As it is displayed in figure 6.3, for a total number of time steps equal to 25000, which requires a wall-clock time of 12639 seconds (~ 3.5 hours), the density residual oscillates about a value of 10^{-3} during the second half of the computation. Considering that for steady state simulations, the residual must tend to zero, it can be stated that the reached value is not completely satisfactory. This bad convergence behavior is caused, on the one hand, by the stiffness of the compressible Navier-Stokes equation system at low Mach numbers, which is partially improved by the use of preconditioning algorithms. On the other hand, it is also due to the inability to use multigrid methods, which besides accelerate the convergence rate, they also damp both the high and the low-frequency errors. Regarding the mass flow rate through the actuator disk surface, at the starting point of the simulation the flow is at standstill conditions, which entails the absence of flow through the rotor. Due to the effect that the prescribed loads have on the flow, velocity is induced and flow motion across the actuator disk is observed that is stabilized after 13000 time steps. According to the described convergence history, the subsequent TAU simulations are run for a number of time steps within a range from 15000 to 25000.

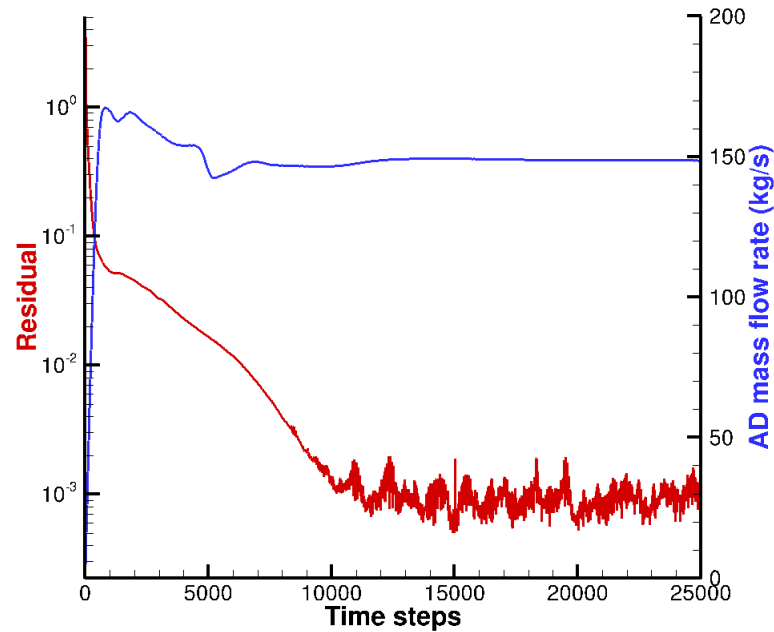


Figure 6.3: Convergence history of the density residual and mass flow rate through the actuator disk for the first hovering flight simulation

The initial standstill of the flow is altered by the action of the prescribed loads over the actuator disk. Since a positive (i.e. upward) thrust force must be generated, the actuator disk induces the flow to move from its upper to its lower surface as it can be seen in figure 6.4 where the streamlines obtained after the first coupling cycle are displayed. The induced velocity distribution along the radial direction of the actuator disk is not uniform due to the fact that the prescribed axial loads also vary with the radius (figure 6.5). The induced velocity reaches its maximum value (downwards) at approximately 77% of the rotor radius. Nevertheless, at the root and especially at the tip, flow recirculation zones are detected. The difference in pressure between the upper and lower sides of the actuator disk entails the recirculation of the flow at the inner and the outer actuator disk boundaries, where the flow goes from the pressure (i.e. lower) side to the suction (i.e. upper) side. These recirculation effects are more severe at the outer boundary of the disk where the highest axial loads are prescribed by BEAT and, thus, the strongest is the pressure gradient.

The reverse flow region that takes place at the edges of the actuator disk alters considerably the aerodynamic load distribution computed by BEAT between two consecutive coupling cycles. Initially, BEAT computes the hovering flight aerodynamic loads along the blades span by assuming a uniform static inflow model which entails that the lift production at each blade sectional element increases with the radius. On the other hand, after performing the simulation of the flow about the actuator disk for the initial prescribed loads, due to the flow recirculation, the induced velocity at the disk boundaries is reduced, observing at the tip even upward flow motion (figure 6.5a). This velocity field is transferred to BEAT and an updated aerodynamic load distribution is computed (figure 6.5b). Due to the lower induced velocities registered at the edges, the sectional angle of attack computed by BEAT at these zones is increased which result in a rise in lift production, while the opposite pattern is observed at the regions where the axial induced velocity reaches its peak.

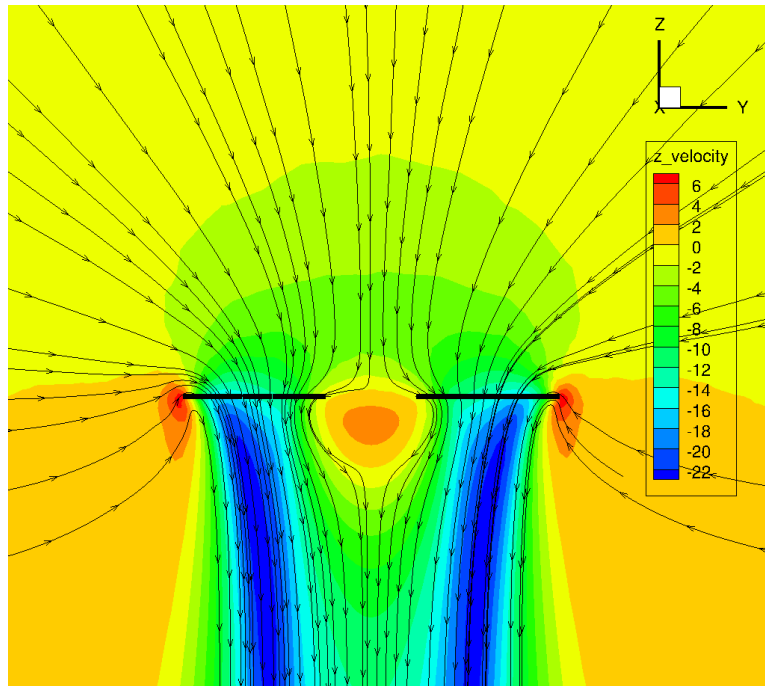


Figure 6.4: Velocity field about the actuator disk in hover computed at the first coupling cycle

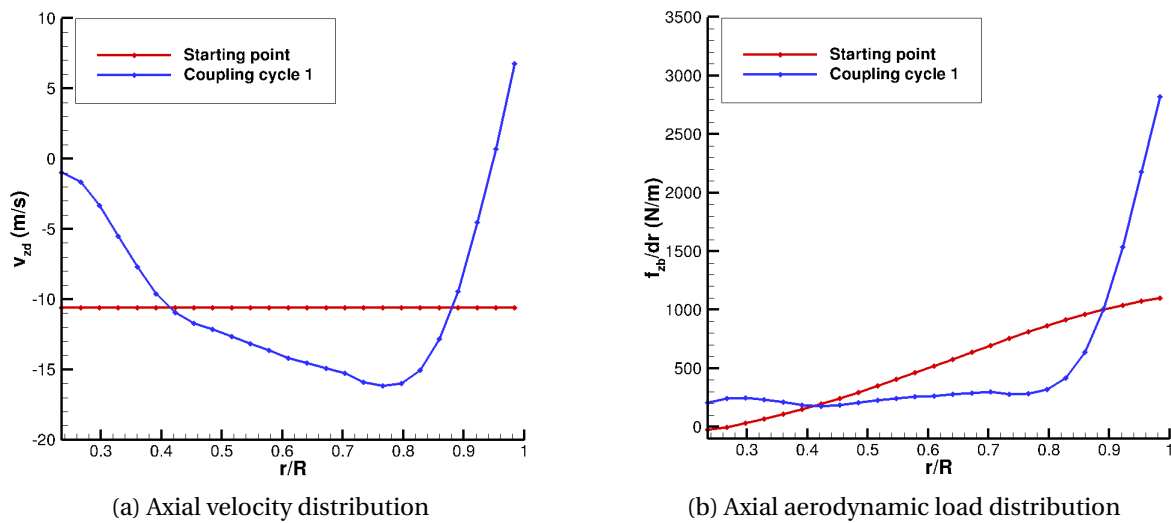


Figure 6.5: Comparison of the initial and first coupling cycle axial velocity and load distributions about the actuator disk in hover

During the subsequent coupling cycles the reversed flow pattern is modified as the prescribed actuator disk loads are updated. At the regions where the axial induced velocity (downward) is higher the sectional lift decreases and can even reach at some point negative values. In this case the pressure jump imposed by the TAU actuator disk is reversed causing new flow recirculation zones. In figure 6.6, the impact of this behavior on the stability of the BEAT/TAU coupling can be observed. As the number of performed coupling cycles is increased, the reversed flow effect is aggravated, resulting in an unstable behavior in hovering flight conditions.

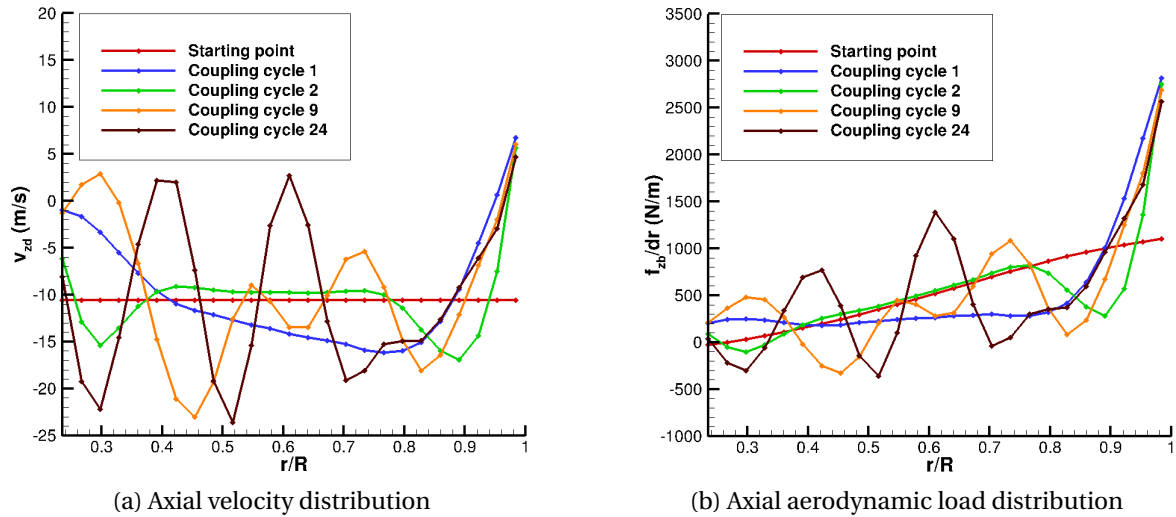


Figure 6.6: Comparison of the axial velocity and load distributions about the actuator disk in hover along the coupling cycles

The propagation of the flow recirculation over the actuator disk surface can be also observed in the vorticity maps shown in figure 6.7. At the first coupling cycle the reversed flow region is located at the edges of the disk. The strength of the vortices shed at the rotor outer boundary is higher compared to the inner boundary where the gradient in pressure is smaller. Nevertheless, after performing several coupling cycles due to the aforementioned effects the vortices are expanded throughout the entire disk.

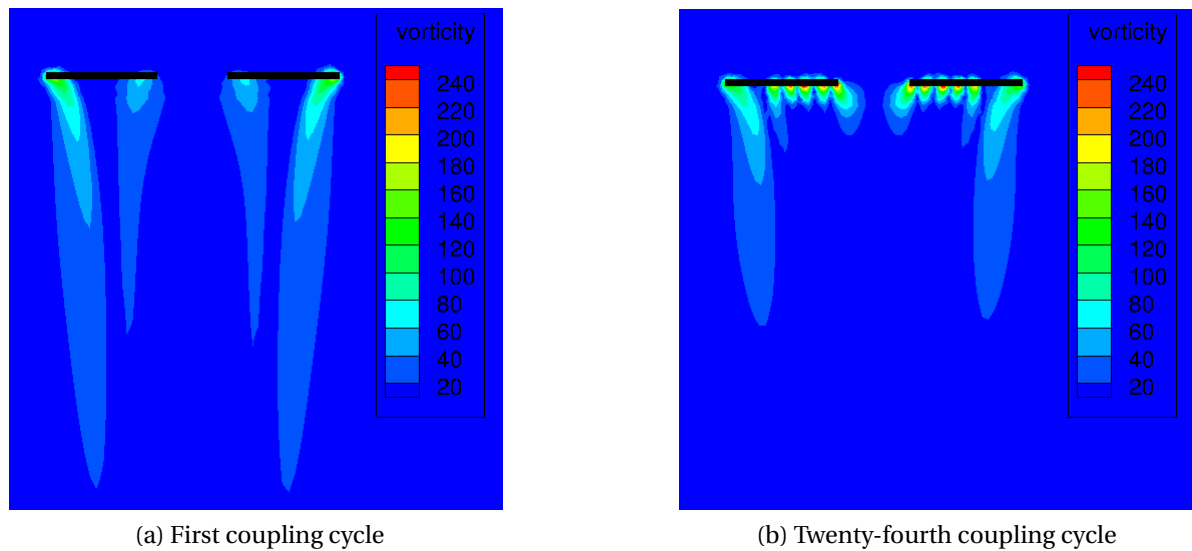


Figure 6.7: Comparison of the shed vorticity pattern about the actuator disk in hover

As it can be deduced from the previous description, the collective pitch control angle required to trim the rotor does not fully converge as the number of coupling cycles increases (figure 6.8). The propagation of vortices along the rotor disk entails changes in both the velocity field and load distribution between consecutive coupling cycles.

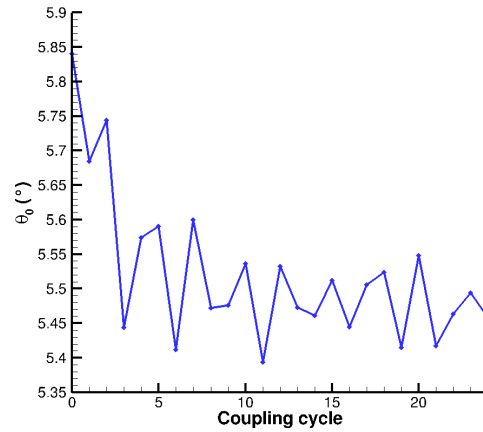


Figure 6.8: Computed collective control angle at different coupling cycles for hovering flight

A correct modeling of the flow recirculation pattern would require an axial induced velocity distribution that nullifies the lift produced at the tip and the root of the blades. With a future implementation of correction models such as the Prandtl tip loss function [66] in BEAT, the axial induced velocity distribution can be corrected in order to reach zero lift at these sections. However, the use of these methods to initialize the coupling between BEAT and TAU does not guarantee the stability of the coupling. Correction methods assume high axial induced velocities at the tip that reduce its sectional angle of attack and, thus, also its associated lift. On the other hand, the reverse flow pattern captured by TAU at the tip has the opposite effect, it increases the angle of attack and hence, also the lift at the tip. Fejtek and Roberts [25] performed CFD flow simulations about an actuator disk in hovering flight whose aerodynamic load distribution was computed by means of the blade element theory. A flow recirculation area was also determined at the outer edge of the rotor disk, which entailed an increase in both the angle of attack and the lift coefficient at the rotor tip. Giovanetti et al. [26] analyzed the geometry of the vortex sheet near the outer boundary of a uniform loaded actuator disk by the application of a potential flow model. They concluded that the computed axial induced velocity distribution in hovering flight was not uniform, especially at the outer boundary, where flow recirculation was captured (figure 6.9a) and this effect was mitigated as the axial flight velocity increased (figure 6.9b).

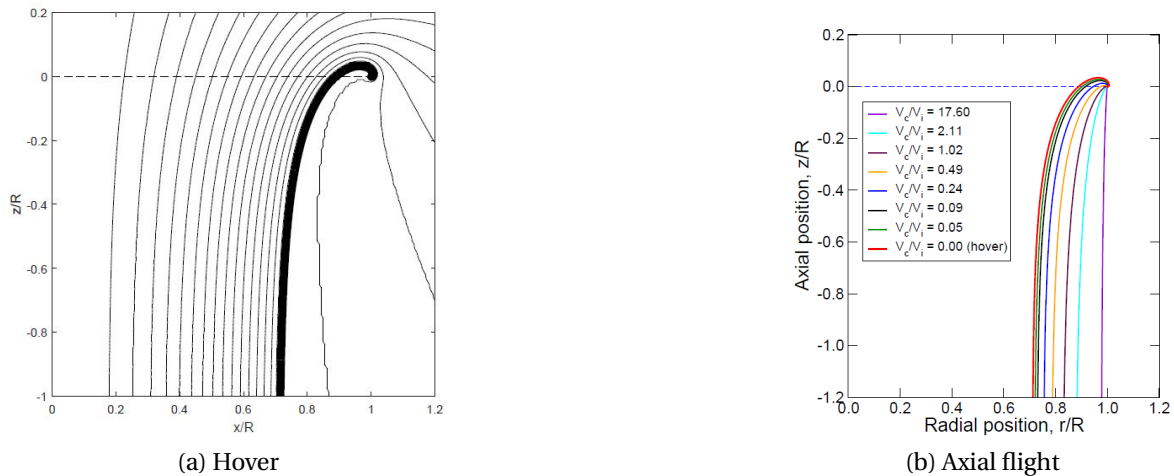


Figure 6.9: Streamlines for hovering and axial flight conditions [26]

6.4.2. FORWARD FLIGHT

The isolated rotor is simulated for both low speed ($v_h = 20 \text{ m/s}$) and high speed ($v_h = 66.7 \text{ m/s}$) forward flight conditions. After running the first coupling cycle simulation, an assessment of the convergence history is carried out in order to estimate its pattern along the successive cycles. According to the conclusion drawn from this initial analysis the user can decide to change partially the setup of the simulation as well as the allocated time slot in the cluster. As it can be observed in figure 6.10, the convergence of the density residual when the flow about an isolated rotor is computed for forward flight conditions is considerably better than for hovering flight (figure 6.3). For a total number of time steps equal to 3000, which requires a wall-clock time of 2224 seconds (~ 0.6 hours), the residual oscillates about a value of 10^{-9} during the last third of the flow computation. The use of a multigrid algorithm contributes to the acceleration of the convergence rate and to the neutralization of both high and low frequency errors. Concerning the mass flow rate through the actuator disk, it can be observed that its convergence is rapidly reached. With this in mind, the subsequent coupling cycle simulations are performed for 3000 time steps.

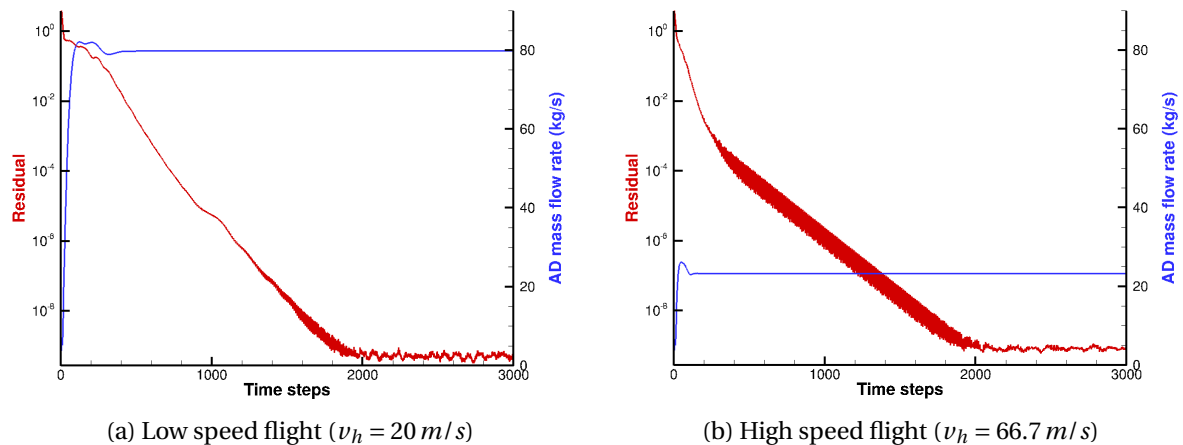


Figure 6.10: Convergence history of the density residual and mass flow rate through the actuator disk for the first forward flight simulation

After performing several coupling cycles between BEAT and TAU significant changes in the flow pattern through the helicopter rotor determined by TAU and thus, in the aerodynamic load distribution computed by BEAT are observed in figures 6.11 and 6.12. At low speed forward flight (figure 6.11 and section A.1), the flow recirculation effects are stronger than at high speeds (figure 6.12 and section A.2) and show an unstable pattern, similar to the one captured in hovering flight, especially at the rear part of the advancing side (between $\psi = 0$ and $\psi = 90^\circ$). The determination of flow vorticity at this region is due to the strong gradient in pressure at the advancing side of the disk root that is computed from the initially prescribed axial load distribution. Nevertheless, despite the fact that low values of axial load are prescribed at the root of the retreating side to initialize the coupling process, vorticity is also developed at this side. This can be caused by the upward velocity components extracted by TAU at the inner boundary due to the captured flow recirculation from the pressure to the suction side of the actuator disk. On the other hand, at high forward speeds the impact of the vorticity on the obtained solutions is lower since the vortices are transported quicker outside the actuator disk. Similar findings concerning the vorticity

pattern were reported by O'Brien and Smith [29] and Le Chuiton [30], who performed CFD flow simulations about an actuator disk in forward flight whose aerodynamic load distribution was computed by means of the blade element theory. In these simulations, vortices shed from both the tip and the root were captured. In addition, it was observed that the strength of the vortices shed at the advancing side was higher than at the retreating side.

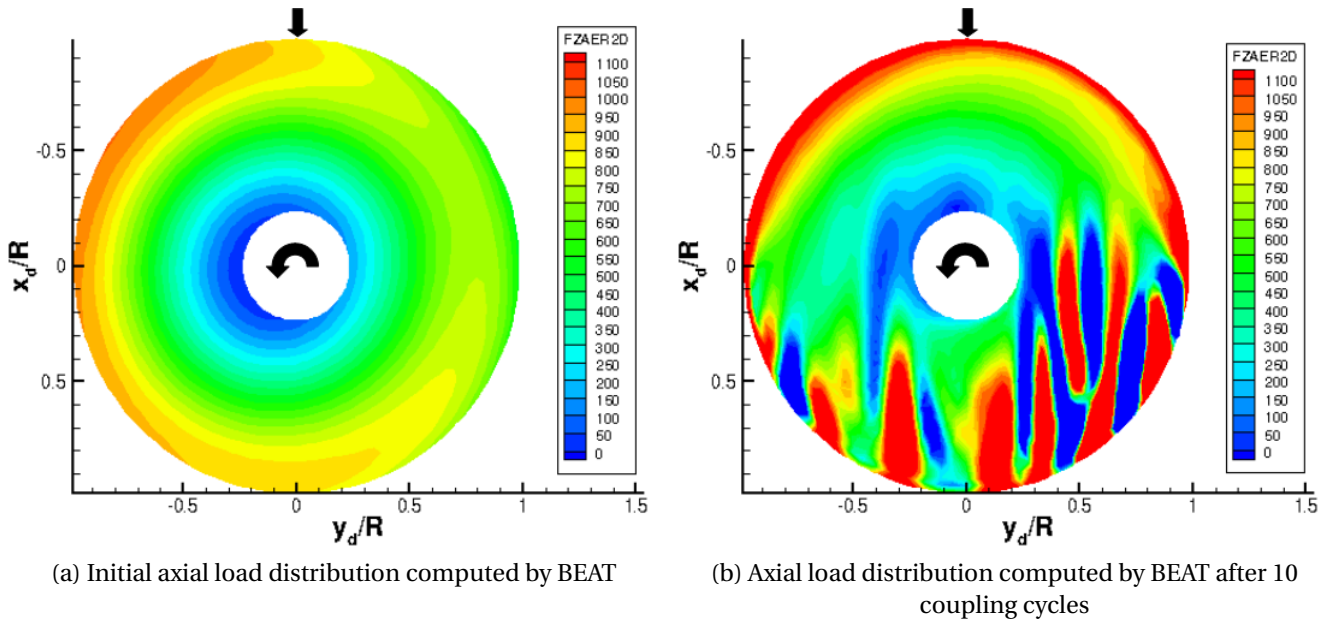


Figure 6.11: Aerodynamic axial load distribution for low speed forward flight conditions ($v_h = 20 \text{ m/s}$)

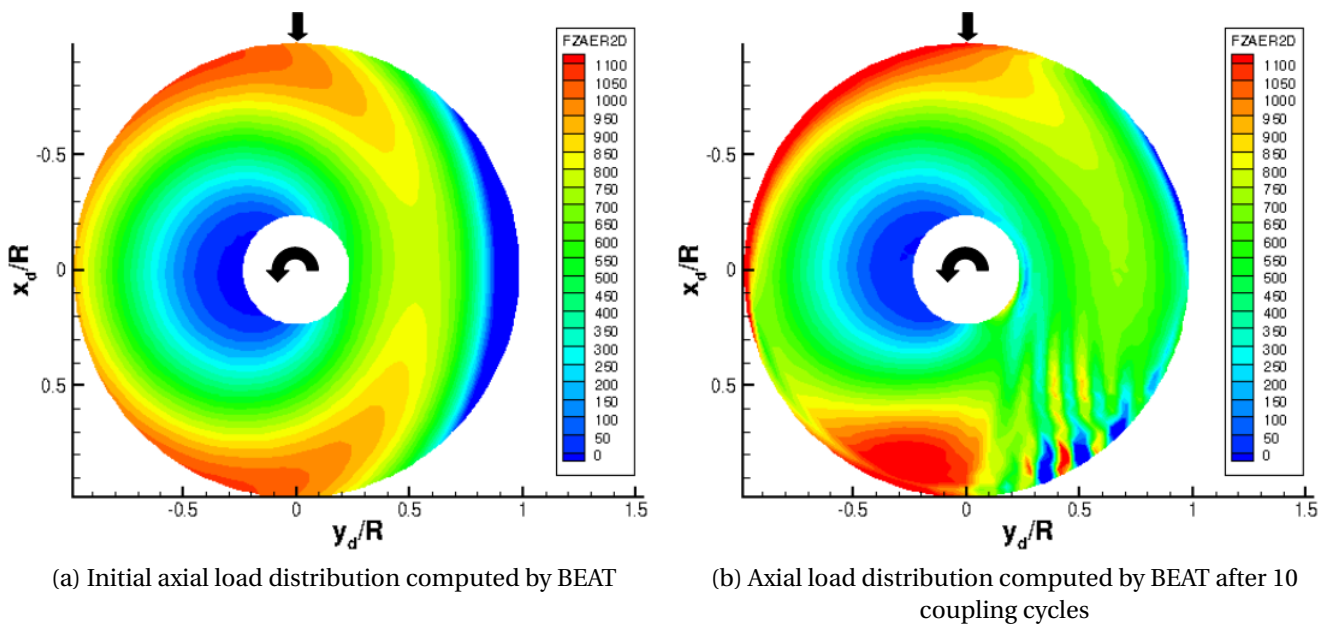


Figure 6.12: Aerodynamic axial load distribution for high speed forward flight conditions ($v_h = 66.7 \text{ m/s}$)

The pattern of the aerodynamic load distribution over the rotor disk shown in figures 6.11 and 6.12 is also addressed by the vorticity maps displayed in figure 6.13. Since zero

shaft angle is considered the inflow velocity is parallel to the plane at which the actuator disk is located. For both low and high speed flight cases, vortices are shed at the rotor inner and outer boundaries at $\psi = 90^\circ$ and $\psi = 270^\circ$. Nevertheless, at high speed flight the shed vortices are displaced faster outside the rotor disk [82]. It has to be taken into account the fact that modeling of a helicopter rotor by means of an actuator disk is equivalent to assume an infinite number of blades. Thus, all the disturbances caused by the computed vorticity over the actuator disk surface have an effect on the aerodynamic load distribution calculated by BEAT that can differ significantly if it is compared to experimental data. Not only the rotor is regarded as a source of vorticity but also the fuselage, the engine exhaust, and the tail rotor, which increases the complexity of the analysis and the impact that the vortices have on the helicopter performance. Figure 6.14 shows the vorticity captured by means of a background-oriented schlieren (BOS) measurement technique about a Bo 105 during a swinging maneuver [83].

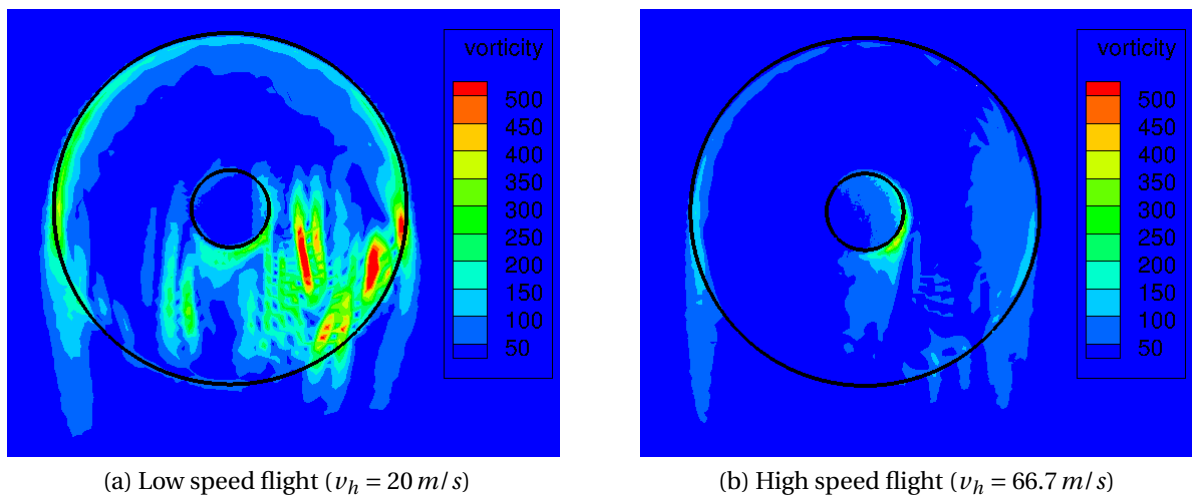


Figure 6.13: Comparison of the the shed vorticity pattern about the actuator disk in forward flight after 10 coupling cycles



Figure 6.14: Vorticity pattern about a Bo 105 during a swinging maneuver [83]

Finally the trimmed collective and cyclic pitch control angles for the two analyzed forward flight conditions are displayed in figure 6.15. It can be observed that after 10 coupling

cycles convergent values can be obtained. Despite the captured vorticity, step changes in control angles are not determined, which can be due to the fact that the vortices induce upward and downward axial velocity components at close regions, thus, their effects in lift distribution are nearly neutralized.

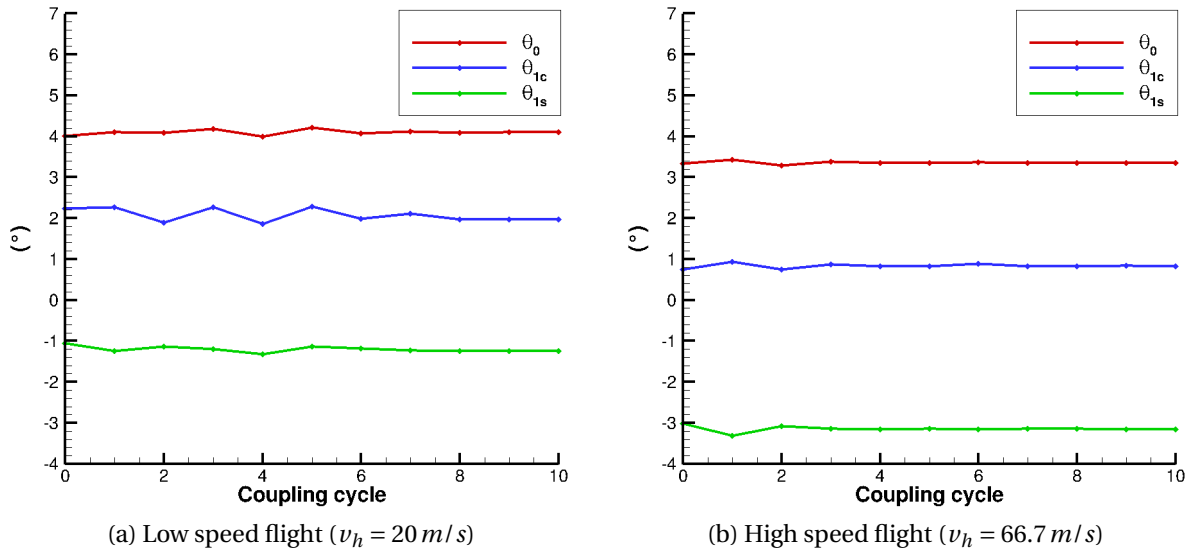


Figure 6.15: Computed pitch control angles at different coupling cycles for forward flight conditions

6.5. COUPLING OVERVIEW

The coupling between TAU and BEAT has been defined as well as an analysis of the results has been carried out for an isolated rotor configuration. In hovering flight conditions, flow recirculation regions are captured by TAU at the edges of the actuator disk. The effect of the reverse flow entails large gradients in lift production between neighboring blade sectional elements that can result in the formation of new flow recirculation zones. The influence of the reverse flow on the computed aerodynamic loads is reduced as the forward flight speed increases, which entails that the shed vortices at the inner and outer boundaries of the actuator disk are displaced more quickly outside the rotor area. Despite the unstable pattern of the flow vorticity captured at low flight velocities, the described coupling approach between TAU and BEAT gives coherent solutions that match the assumptions associated with the modeling of helicopter rotors by means of an actuator disk where the prescribed loads are computed according to the blade element theory.

7

VALIDATION OF THE COUPLING

This chapter covers the analysis and validation of the results computed by performing the iterative coupling simulations between BEAT and the TAU actuator disk. The accuracy of this approach is validated by comparing the obtained results with those measured during the HART II wind tunnel test campaign. The causes of the found discrepancies between the numerical and the experimental data are assessed and taken into consideration to constitute the baseline to be developed for future work as well as to streamline the methodology to be followed. In addition, a comparison of the accuracy and the performance of the developed coupling strategy with other methods currently used at the DLR is carried out in order to evaluate the advantages and disadvantages of its implementation.

7.1. HART II TEST

The HART II program [84, 85] was conducted in October 2001 in cooperation with researchers from DLR, NASA, ONERA, US Army, and DNW. The aim of the project was to create a database of accurate rotor wake measurements by performing wind tunnel experiments of a 40% scaled version of the Bo 105 main rotor. The model was tested for descending flight conditions and an advance ratio of $\mu = 0.1508$ at which Blade Vortex Interaction (BVI) effects have a significant influence on the rotor performance. Concerning the rotor setting, three different cases were analyzed: a baseline case, a minimum noise case and a minimum vibration case. The baseline case was carried out with first-harmonic control inputs, while Higher Harmonic Control inputs (HHC) were employed in the other cases to reduce the noise and vibrations respectively. Since the use of HHC inputs is not included in the scope of the the present work, only the baseline configuration results are taken into consideration for its validation.

7.1.1. WIND TUNNEL FACILITY

The experiments were conducted in the Large Low-speed Facility (LLF) of the DNW (figure 7.1), which is a subsonic closed wind tunnel located at Marknesse (the Netherlands). The HART II test was performed in the open-jet configuration of 8 m x 6 m cross-sectional dimensions surrounded by anechoic test hall with a volume slightly higher than 30,000 m^3 . The rotor wake pattern was measured by using the Particle Image Velocimetry (PIV) technique [48].



Figure 7.1: Large Low-speed Facility of the DNW [84]

The wind tunnel operating conditions (table 7.1) were defined by three variables: temperature T_∞ , static pressure p_∞ , and freestream jet velocity V_∞ . Both the static temperature and the static pressure depend on the weather conditions which during the test period were quite stable [84]. From these variables, the flow density ρ_∞ , the speed of sound a_∞ and the freestream jet Mach number M_∞ can be computed according to:

$$\rho_\infty = \frac{p_\infty}{RT_\infty} \quad (7.1)$$

$$a_\infty = \sqrt{\gamma RT_\infty} \quad (7.2)$$

$$M_\infty = \frac{V_\infty}{a_\infty} \quad (7.3)$$

Variable	Symbol	Value
Air temperature	T_∞	290.45 K
Air static pressure	p_∞	100.97 kPa
Jet velocity	V_∞	32.9
Air density	ρ_∞	1.2055 kg/m ³
Speed of sound	a_∞	341.7 m/s
Mach number	M_∞	0.0963

Table 7.1: Wind tunnel flow data

7.1.2. ROTOR MODEL AND TEST RIG

The analysed rotor of the HART II program was a 40% scaled model of the Bo 105 hingeless four-bladed main rotor. The blade planform was rectangular with an airfoil chord of 0.121 m and 2 m radius. The profiled part was extended from a distance of 0.44 m to the tip and the NACA 23012 airfoil was employed. The blade was linearly twisted and a pre-cone angle

of 2.5° was imposed, which is the same as in the full-scale configuration. Both the spar and blade skin were made of glass-reinforced plastic.

The rotor was mounted over a generic fuselage-like fairing which stored the test rig. The test rig contained the hydraulic drive system and the rotor control system and was supported by a computer controlled sting support mechanism. The hydraulic engine induced a shaft rotational speed of 1042 rpm.

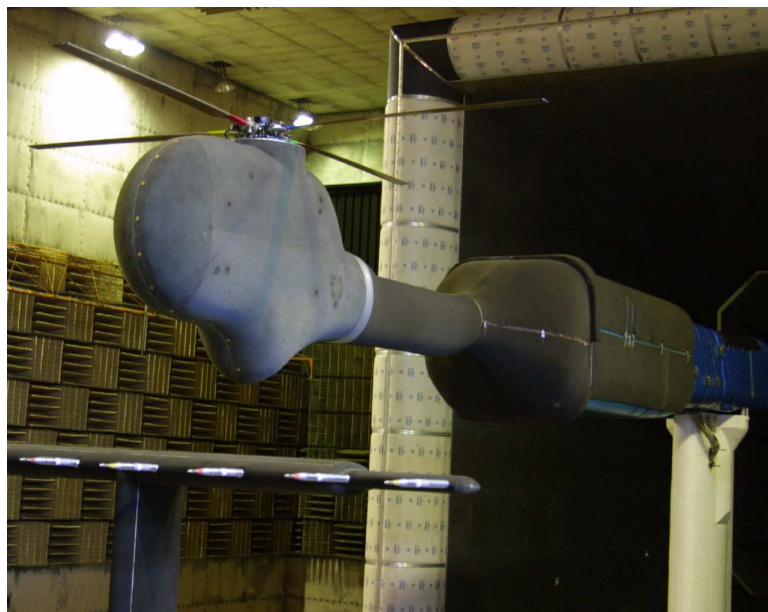


Figure 7.2: HART II test configuration [84]

7.1.3. ROTOR TRIM

In order to account for descending flight conditions a rotor shaft angle of 5.4° was imposed. Nevertheless, due to the wind tunnel interference effects, the rotor shaft angle must be correlated, which results in an effective shaft angle of 4.5° . An electrical actuator was responsible for the transmission of the conventional control inputs (collective, lateral and longitudinal cyclic control) to the rotor blades. The rotor was trimmed for a prescribed vertical lift force of 3300 N which for the given effective shaft angle α_{eff} , it is equivalent to a thrust force of $T = 3310.2\text{ N}$ parallel to the rotor shaft. Furthermore, both the prescribed pitching and rolling moments had values equal to zero.

The blade pitch angles were determined by measuring the displacement that the electrical actuator induced to the nonrotating disk of the swashplate. For the baseline case the obtained control angles are displayed in table 7.2. However, as it is pointed in the test documentation [84], it has to be taken into consideration that errors are subjected to the measured rotor forces and moments, which may have an effect on the accuracy of the results. A scatter of the thrust force of 150 N was determined, while the pitching and rolling moments had disturbances of 15 Nm and 20 Nm respectively.

θ_0	θ_{1C}	θ_{1S}
3.8°	1.92°	-1.34°

Table 7.2: Control inputs of the baseline case

7.2. GRID

The spatial discretization of the physical domain is carried out by means of overset grids. The physical domain is defined as a rectangular prism whose boundaries are located considerably far away from the rotor (340 m x 180 m x 240 m) in order to avoid that the computations can be negatively affected by the domain truncation. A structured background grid covers the complete physical domain and the size of its elements increases towards the farfield boundaries. Another possible approach would be to model the wind tunnel walls as well as the geometry of the flow measurement setup, which have interference effects on the rotor performance. The fuselage surface and its vicinity is discretized by means of a structured grid which has been previously used in FLOWer simulations [54]. A hybrid grid is employed for the discretization of the rotor region and the actuator disk surface is represented by 2400 quadrilateral elements at both sides. The three overlapping meshes displayed in figure 7.3 are combined by using the Chimera technique implemented in TAU. The grid points penetrating the fuselage and the actuator disk structure are blanked, by employing hole cut geometries. Thereby, all grids remain with a sufficient overlapping region to enable proper information transfer by means of numerical interpolation.

	Background grid	Fuselage grid	Actuator Disk grid	Total
Number of points	8,641,806	1,195,886	598,437	10,436,129
Number of elements	8,603,852	1,179,648	3,113,516	12,897,016
Number of tetrahedra	0	0	3,009,156	3,009,156
Number of prisms	0	576	49,560	50,136
Number of pyramids	0	0	6,800	6,800
Number of hexahedra	8,603,852	1,179,072	48,000	9,830,924

Table 7.3: Grid characteristics

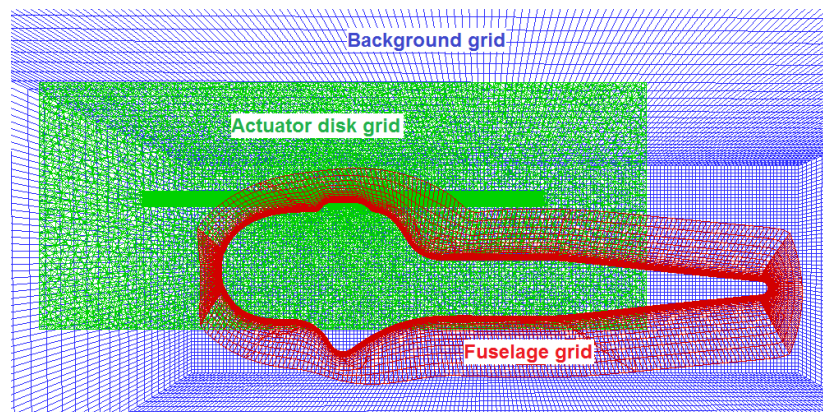


Figure 7.3: HART II grid structure

7.3. SIMULATION SET UP

The TAU simulations of the flow about the described configuration are run on the DLR $C^2A^2S^2E-2$ cluster. The grid is partitioned into 48 subdomains by means of the TAU private partitioner. Hence, the flow governing equations are evaluated on 48 cluster processors (2 nodes). A central scheme with a artificial matrix dissipation model is employed for the computation of the fluxes. The flow governing equations are evaluated in time by means of an implicit backward Euler time-stepping method and the selected CFL number is equal to 5. A $k-\omega$ eddy viscosity model is considered for the flow turbulence modeling. In addition, a v -cycle for three multigrid levels is employed to accelerate the convergence towards the steady state solution.

The flow velocity at the farfield boundaries is set to 32.9 m/s with a zero angle of attack with respect to the the fuselage whose surface is modeled as a viscous wall. The descend flight conditions are represented by tilting backwards the actuator disk at an angle of 4.5° .

7.4. ANALYSIS OF THE RESULTS

In this section the analysis of the obtained results as well as the validation of the coupling between BEAT and the TAU actuator disk are addressed. Firstly, the effect that the fuselage has on the rotor performance is assessed. Subsequently, the computed numerical results are compared with the the wind tunnel measurements and the possible sources of the found discrepancies are analysed. Finally, the performance of the developed approach is evaluated with respect to other rotor analysis CFD methods currently used at DLR.

7.4.1. EFFECT OF FUSELAGE

An assessment of the influence of the fuselage on the rotor trim controls is carried out by performing TAU simulations of the complete HART II case configuration (fuselage and rotor) and the isolated rotor. As it can be seen in figure 7.4, after running 8 coupling cycles the rotor control angles converge to different values in each case (table 7.4). Despite of initializing the first cycle with the same prescribed aerodynamic load distribution on the actuator disk surface, it can be observed that while the collective angle θ_0 is not strongly affected by the influence of the fuselage, the longitudinal cyclic θ_{1s} and especially the lateral cyclic θ_{1c} show significant variations.

	Isolated rotor	Rotor + Fuselage
θ_0	2.53°	2.51°
θ_{1c}	1.80°	2.10°
θ_{1s}	-1.27°	-1.39°

Table 7.4: Computed pitch controls after 8 coupling cycles with and without a fuselage underneath the rotor

The cause of these changes in the pitch control angles is related to the flow that goes around the fuselage surface. As it is pointed by van der Wall et al. [86], in forward flight the fuselage generates an upwash in the front part of the rotor and a downwash in the rear part (figure 7.5). The impact of these interference effects on the rotor performance is increased with the flight speed and the closeness between the rotor and the fuselage. Thus, the pres-

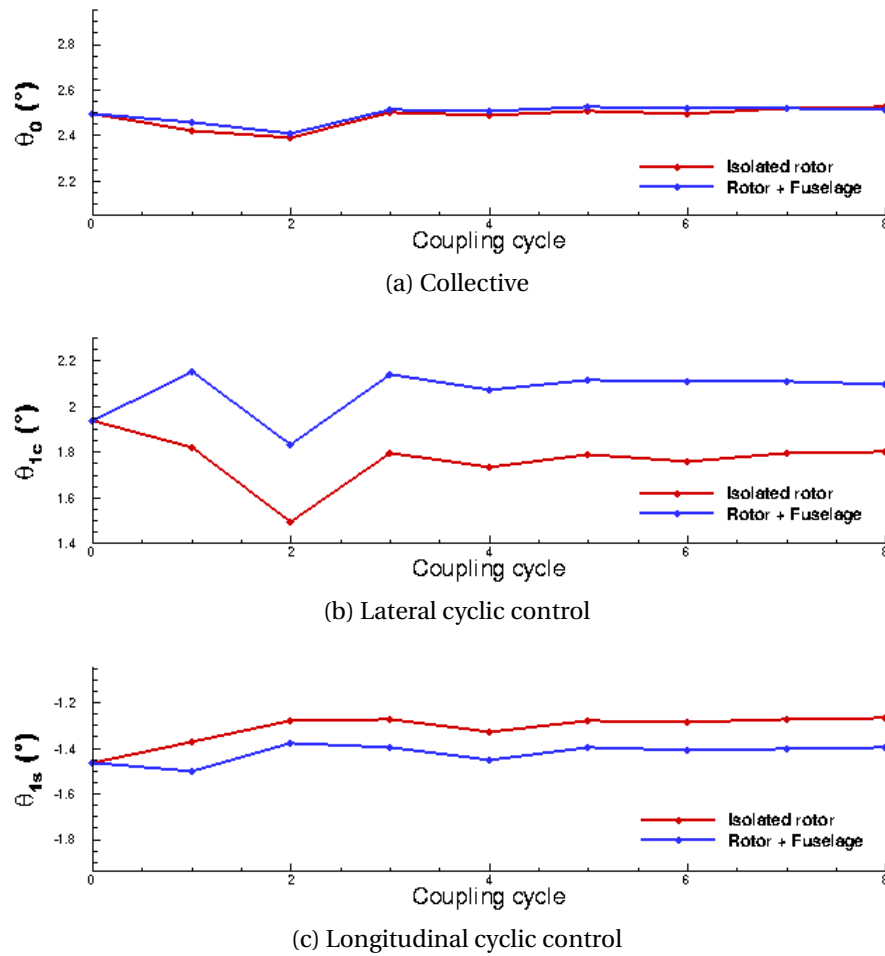


Figure 7.4: Computed pitch control angles at different coupling cycles with and without a fuselage underneath the rotor

ence of the fuselage underneath the rotor alters the angle of attack and the flow dynamic pressure relative to each blade sectional element with respect to the isolated rotor case.

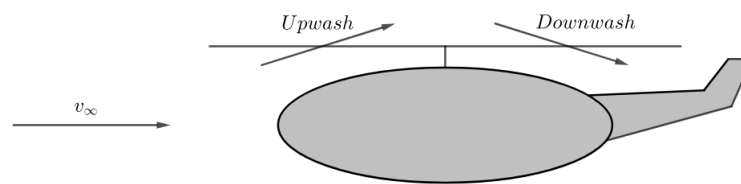


Figure 7.5: Fuselage-rotor interference

In order to evaluate the contribution of the fuselage on the velocity field over the actuator disk surface, figure 7.6 displays the captured axial velocity by TAU after the first coupling cycle where the same axial and tangential aerodynamic load distributions are prescribed. It can be seen that at the front region of the rotor hub the captured axial velocity is higher in the case in which the fuselage is considered. On the other hand due to the downwash induced by the fuselage at the rear region of the rotor hub, the axial velocity reaches lower values than the ones obtained in the isolated rotor configuration.

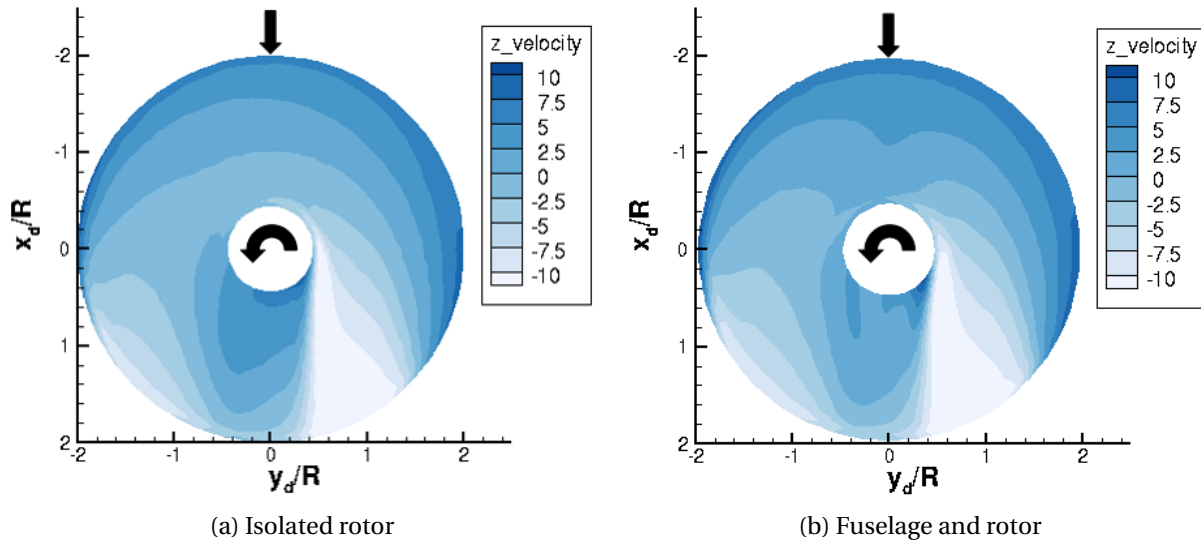


Figure 7.6: Axial velocity distribution over the actuator disk surface computed at the first coupling cycle

From the aspects described above, the differences in pitch control angles found between both configurations can be explained. The small variation in collective is due to the fact that the effect of the upwash on the lift production at the front part of the rotor is nearly neutralized by the effect of the downwash on its rear part. Thus, the presence of the fuselage underneath the rotor does not have a large impact on the rotor thrust. On the other hand, the upwash increases the angle of attack and consequently the generated lift at the front part of the rotor, while the downwash has the opposite effect at the rear part of the rotor. This asymmetry in lift distribution can yield to undesirable moments about the rotor hub, hence, a rise in the lateral cyclic control angle is required. The longitudinal cyclic control is less affected than the lateral cyclic control since the velocity field induced by the fuselage is almost symmetrical with respect to the fuselage symmetry plane.

The aforementioned effects that the fuselage has on the velocity field and thus, on the trim controls are not addressed by any of the static inflow models available in BEAT. Therefore, if this rotor code is used individually, without being coupled with TAU, these effects can not be taken into account. Van der Wall et al. [86] developed a semi-empirical model from the observation of the flow pattern obtained by CFD simulations that can be implemented in comprehensive rotor codes in order to account for these effects. This mathematical model can be regarded in the future as an improvement of the BEAT features.

7.4.2. COMPARISON WITH EXPERIMENTAL RESULTS

In order to assess the accuracy of the coupling strategy between BEAT and TAU, the converged trim control angles computed after performing 8 coupling cycles are compared with those measured during the wind tunnel experiments. Table 7.5 contains the values of both the computed pitch controls and the ones measured during the HART II campaign. It can be observed that while the computed cyclic controls are in relative good agreement with the measured values, the computed collective control is substantially underestimated.

The elastic deformation of the rotor blades is a key factor that can have an important influence on the rotor aerodynamic performance. Nevertheless, this aspect is disregarded by BEAT, which computes the aerodynamic loads acting along the blade span under the

	BEAT-TAU	Experiment	$\theta_{exp} - \theta_{com}$
θ_0	2.51°	3.80°	1.29°
θ_{1c}	2.10°	1.92°	-0.18°
θ_{1s}	-1.39°	-1.34°	0.04°

Table 7.5: Rotor control angles of the HART II baseline case

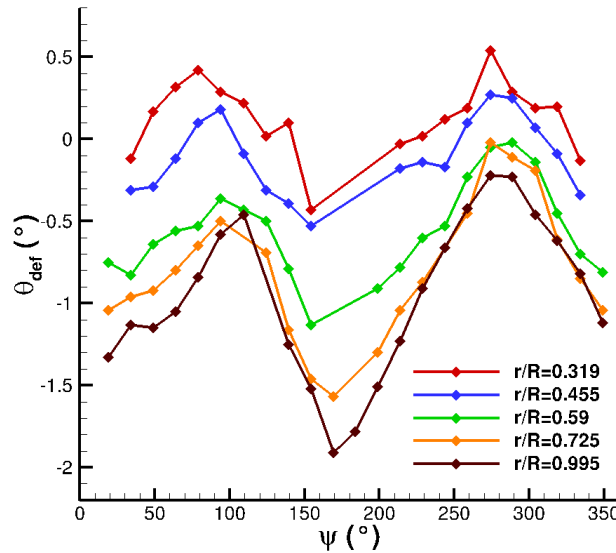


Figure 7.7: Measured blade torsional deformations of the HART II rotor [84, 85]

assumption of a fully stiff blade structure. According to Langer [87], the measured blade elastic deformations of the tested rotor in pitch, flap and lead-lag are not negligible and have a significant impact on its performance. Regarding the measured blade torsional deformations, as it can be seen from figure 7.7, they vary along the rotor radius and azimuth angle. In addition, it can be observed that due to the torsional deformation, the blade sectional pitch angle is reduced, especially at the regions located close to the blade tip.

The blade sectional pitch is defined by the sum of the blade geometrical twist, the pitch transmitted by the swashplate and the torsional deformation. Hence, it can be computed by:

$$\theta = \theta_r + \theta_{tw}r + \theta_0 + \theta_{1c}\cos\psi + \theta_{1s}\sin\psi + \theta_{def} \quad (7.4)$$

It has to be noted that BEAT adjusts the pitch controls in order to reach trimmed flight conditions. Thus, the contribution that the elastic deformation of the blade has on the pitch angle has to be contained in the computed control angles. Figure 7.8 shows that both the measured and the computed blade sectional pitch angle distribution at 72.5% of the blade span where it can be observed that the resultant pitch angle distribution along the azimuth angle captured during the wind tunnel experiments shows some similarities with the values computed by performing the coupling between BEAT and TAU.

The modeling of the helicopter rotor as a zero thickness surface on which steady prescribed loads act, limits the accuracy of the vorticity analysis. The HART II case was performed under flight conditions in which unsteady blade-vortex interaction effects were

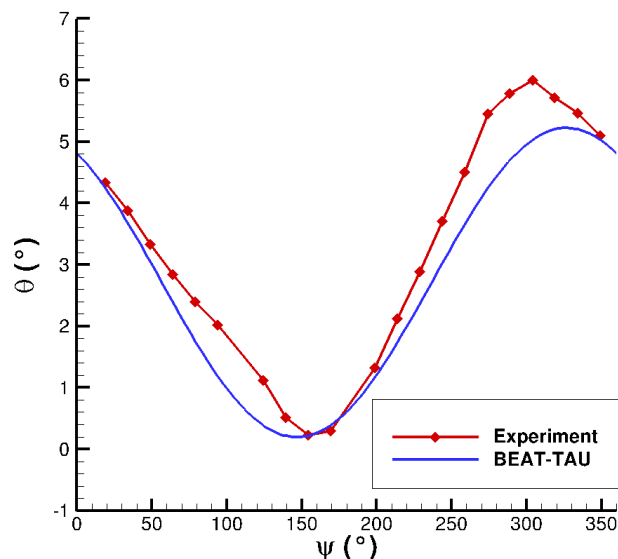


Figure 7.8: Comparison between the computed and the measured blade pitch angle distribution at $r/R = 0.725$

significant. Furthermore, it has to be pointed that the blade aerodynamic loads are determined by means of a two-dimensional analysis at each blade sectional element which means that the radial velocity components are disregarded. Regarding the blade geometrical modeling, the pre-cone angle of 2.5° is neglected due to the inability of BEAT to account for this parameter. Finally, precision errors in the measurements and wind tunnel disturbance effects can have a slight contribution on the found discrepancies.

From this analysis it can be concluded that the elastic behavior of the rotor blades and their aerodynamic performance are coupled facts. Elastic deformations modifies the blade sectional angle of attack and therefore, the aerodynamic loads which act on the blades. On the other hand, changes in the aerodynamic load distribution alter the deformation pattern of the blades. In order to account for the elastic effects and consequently, to improve the accuracy of the results obtained by the coupling between BEAT and TAU, it is recommended to include a structural module in BEAT or to couple it with an existing structural code in future versions of this rotor analysis code (figure 7.9).

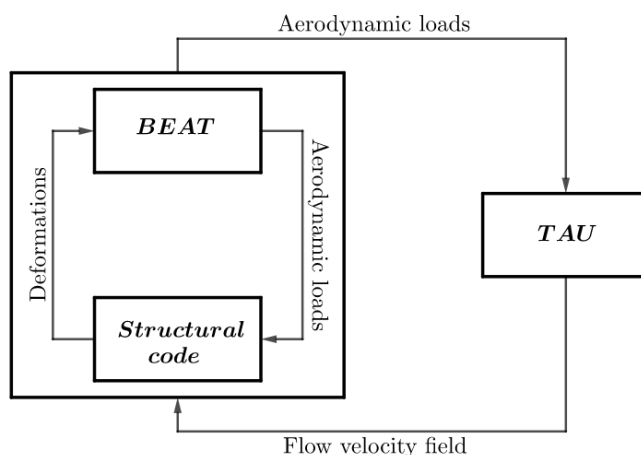


Figure 7.9: Recommended scheme for a future coupling version

7.4.3. COMPARISON WITH OTHER APPROACHES

The measured data in the HART II campaign have been used for the validation of different helicopter rotor modeling approaches. At DLR, the elastic behavior of the blade is usually addressed by the use of the comprehensive rotor code HOST, which models the blade as a quasi one-dimensional beam based on an extended Euler-Bernoulli formulation assuming moderate deformations in pitch, flap and lead-lag. In addition, the flow about the blade geometry can be simulated by means of the block-structured flow solver FLOWer or the unstructured solver TAU. The iterative coupling between the rotor comprehensive code HOST and the flow solvers FLOWer/TAU can be defined in such a way that the aerodynamic loads acting on the individually modeled rotating blades are obtained by the flow solver and subsequently transferred to HOST which is responsible for the computation of the blade elastic deformations that are prescribed to the flow solver. Table 7.6 contains the pitch control angles computed by different methods: the coupling of BEAT with the TAU actuator disk and the coupling of HOST with FLOWer [54] and TAU [87]. Since the blades are modeled individually and blade elastic deformations are taken into consideration the latter approaches offer collective values closer to the measured one. Nevertheless, the longitudinal cyclic computed by performing the coupling between BEAT and the TAU actuator shows the minimum difference from the experimental value. Modeling is always subjected to uncertainties, which are defined as the difference between the model and the actual system to be modeled.

	BEAT-TAU Actuator Disk	HOST-FLOWer	HOST-TAU	Experiment
θ_0	2.51°	3.72°	3.44°	3.80°
θ_{1c}	2.10°	1.86°	1.67°	1.92°
θ_{1s}	-1.38°	-0.98°	-0.57°	-1.34°

Table 7.6: Trim controls computed by different approaches for the HART II baseline case

The main assumption associated with the actuator disk approach is the fact that the rotor is replaced by a zero thickness surface on which prescribed steady loads act. Thus, the complexity associated with the unsteady flow pattern that is captured by the other two aforementioned coupling strategies is reduced, which entails lower computational costs. The individual modeling of the blades in CFD simulations requires the computation of the flow pattern about the blades along the azimuth angle. As it is pointed by Wilke [54], some rotor revolutions need to be simulated to allow for the development of the rotor wake before valid results can be obtained. Table 7.7 contains the CPU time required to perform the first cycle simulation by the aforementioned coupling approaches where the physical domain is discretized by a grid of similar number of points (10-13 millions). It can be observed, that the cost associated with the coupling between BEAT and the TAU actuator disk is remarkably lower than the other two methods, which requires computational times 60 (HOST-FLOWer) and 144 (HOST-TAU) times higher. Hence, it can be stated that the main advantage of the developed approach over more accurate methods is the significant reduction of the computational cost that it offers.

	CPU time (hours)	Ratio
BEAT-TAU Actuator Disk	290	1
HOST-FLOWer	17400	60
HOST-TAU	41700	144

Table 7.7: CPU time required by the CFD solver to perform the first coupling cycle simulation

7.5. ANALYSIS OVERVIEW

From the analysis of the obtained results for the HART II test configuration conducted in this chapter some conclusions can be drawn. Firstly, it has been shown that the consideration of a fuselage underneath the rotor has a non-negligible influence on the computed velocity field about the actuator disk. The effect of additional bodies in the vicinity of the rotor is not addressed by BEAT, thus, it can only be captured by performing TAU simulations. Secondly, due to the fact that the blade elastic deformations are disregarded in the developed approach, differences in the trim control angles are found between the computed and the measured values. Nevertheless, the obtained pitch angle distribution at the 72.5% blade radial section is in relatively good agreement with the one captured during the wind tunnel test campaign. Finally, it has been demonstrated that the coupling between BEAT and the TAU actuator disk enables the computation of the flow about helicopter rotors at lower computational cost than other more accurate approaches. This fact empowers the idea of further developments of the method such as the implementation of a structural module in BEAT in order to account for blade deformations in pitch, flap and lead-lag. This modification can improve considerably the accuracy of the approach without important increments of the computation time which mainly depends on the way that the rotor is modeled by the flow solver.

8

CONCLUSIONS AND RECOMMENDATIONS

This chapter summarizes the outcome of the research carried out in the thesis. The main findings are discussed in section 8.1, while the recommendations for future work are streamlined in section 8.2.

8.1. CONCLUSIONS

A mid-fidelity method for the aerodynamic modeling of helicopter rotors in hovering and forward flight conditions has been developed. This approach consists of replacing the helicopter rotor by means of an actuator disk which imposes both pressure and tangential velocity jumps to the flow going through it. Flow simulations are performed in the CFD solver TAU, which includes an actuator disk module among its functionalities. On the other hand, both the axial and tangential aerodynamic load distributions over the actuator disk surface need to be prescribed. For this purpose, BEAT, a rotor analysis code based on the blade element theory has been created. The main idea of this coupling strategy is that the velocities captured at the grid points of the TAU actuator disk after each CFD simulation are transferred to BEAT, which computes an updated aerodynamic load distribution.

BEAT enables the computation of the blade loads by performing a two-dimensional aerodynamic analysis at each blade sectional element. The aerodynamic coefficients are taken from look-up tables for the corresponding sectional angle of attack and Mach number. Pitching and flapping degrees of freedom are considered and contribute to the calculation of the blade angle of attack. The pitch controls are adjusted to avoid undesirable moments with respect to the rotor hub and to reach the prescribed performance conditions by means of the implementation of a Newton-Raphson algorithm. Regarding the flapping angle distribution, it is determined by imposing equilibrium of moments about the flapping hinge. This condition defines a second-order differential equation that is solved by the use of explicit schemes. On the other hand, elastic deformations and leading-lagging blade motion are disregarded.

Before setting up the coupling between BEAT and the TAU actuator disk, the performance of the former has been verified. Firstly, the evaluation of the influence of the input parameters on the obtained results has revealed that those are coherent and consistent with the modeling assumptions. Secondly, it has been shown that the outcomes determined by BEAT are in good agreement with the results computed by the rotor comprehensive code HOST.

The stability of the coupling between BEAT and the TAU actuator disk has been tested for an isolated rotor configuration in hovering and forward flight conditions. In hover, the convergence of the CFD flow simulations towards the steady state solution is not satisfactory. This bad convergence behavior is caused, on the one hand, by the stiffness of the compressible Navier-Stokes equation system at low Mach numbers. The use of preconditioning algorithms can partially improve this pattern but it is not enough to obtain fully convergent solutions. On the other hand, the multigrid methods implemented in TAU to accelerate the convergence rate and to damp both the high and low-frequency errors are not robust in this flight condition. In addition, flow recirculation regions are captured in TAU at the inner and outer boundaries of the actuator disk. The influence of the reverse flow entails large gradients in lift production between neighboring blade sectional elements, which can result in the unstable formation of new flow recirculation zones. These effects are diminished in forward flight conditions, where the shed vorticity is displaced more quickly outside the rotor area. In addition, the robustness of the flow solver is remarkably better than in hovering flight.

The accuracy of the coupling approach has been validated by comparing the obtained results with those measured during the HART II wind tunnel test campaign. The found differences in the trim control angles between the computed and measured values are mainly assigned to the fact that the blade elastic deformations are disregarded in the developed approach. Moreover, the modeling of the helicopter rotor as a zero thickness surface on which steady prescribed loads act, limits the accuracy of the vorticity analysis.

Finally, it has been demonstrated that the coupling between BEAT and the TAU actuator disk reduces considerably the computation time required to compute the flow through the helicopter rotor with respect to other more accurate approaches. This fact empowers the idea of further developments of BEAT, which can improve its accuracy without important increments of the time requirements, that are mainly dependent on the way that the rotor is modeled by the flow solver.

8.2. RECOMMENDATIONS

The accuracy of the developed coupling approach can be enhanced by means of further improvements of BEAT. Currently, only linearly twisted rectangular blades of constant mass distribution can be modeled in BEAT. In further versions of the rotor analysis code, the modeling of non-uniform blade chord and mass distributions and both the sweep and anhedral angles would increase the range of rotor configurations that can be analyzed. Concerning the spatial discretization of the rotor disk, it is recommended to implement a non-uniform distribution of the control points or stations in order to increase their density both at the root and the tip, which are regions where vortices are shed. Furthermore, the pitch controls are adjusted to trim the rotor without taking into consideration the contribution of the other helicopter components such as the fuselage, vertical fins, horizontal stabilizer and tail rotor. The complex pattern of the interactions between the aforementioned components complicates the task of an accurate modeling. Semi-empirical models can be used to correct the static inflow models available in BEAT. Regarding the modeling of the blade flapping motion, the current version of BEAT assumes that the blade can freely flap about the flapping hinge. This assumption can reduce the accuracy of the tool especially when hingeless rotors are considered. Thus, the possibility to take into account the blade stiffness and the precone angle can be regarded as a powerful upgrade. In addition, not only

the pitching and flapping motion, but also the lagging motion of the blades should be modeled.

From the analysis carried out in this thesis, it can be concluded that the elastic behavior of the rotor blades and their aerodynamic performance are coupled facts. Elastic deformations modifies the blade sectional angle of attack and therefore, the aerodynamic loads acting on the blades. Moreover, changes in the aerodynamic load distribution alter the deformation pattern of the blades. In order to account for the elastic effects and consequently, to improve the accuracy of the results computed by BEAT, it is recommended to include a structural module or to couple it with an existing structural code.

Concerning the coupling approach between BEAT and TAU, further research should be carried out to improve the robustness of the flow solver TAU in hovering flight conditions. Furthermore, the application of hub and tip correction factors in BEAT would reduce the pressure gradients at the actuator disk boundaries and thus, the flow recirculation effects can be alleviated.

A

AXIAL LOAD DISTRIBUTION IN FORWARD FLIGHT CONDITIONS

In this appendix, the evolution of the aerodynamic axial load distribution computed by BEAT during the coupling approach with TAU for forward flight conditions and an isolated rotor configuration (subsection 6.4.2) is displayed. Two cases are addressed: low speed (section A.1) and high speed (section A.2).

A.1. LOW SPEED FORWARD FLIGHT ($v_h=20$ m/s)

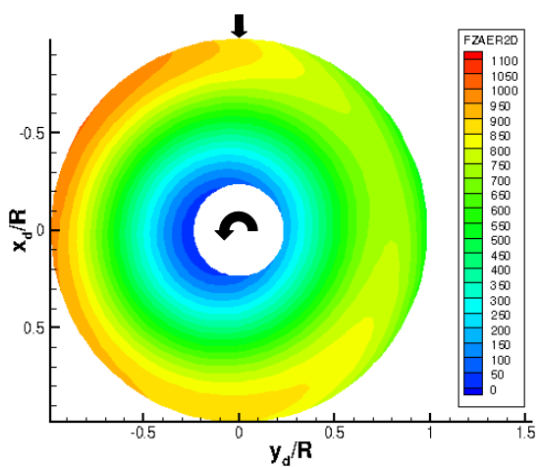


Figure A.1: Initial axial load distribution computed by BEAT ($v_h = 20$ m/s)

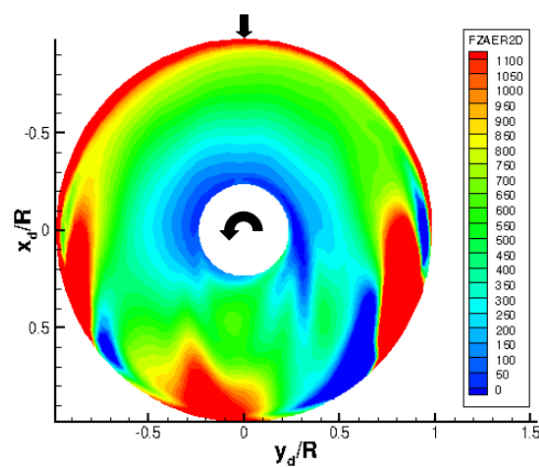


Figure A.2: Axial load distribution computed by BEAT after 3 coupling cycles ($v_h = 20$ m/s)

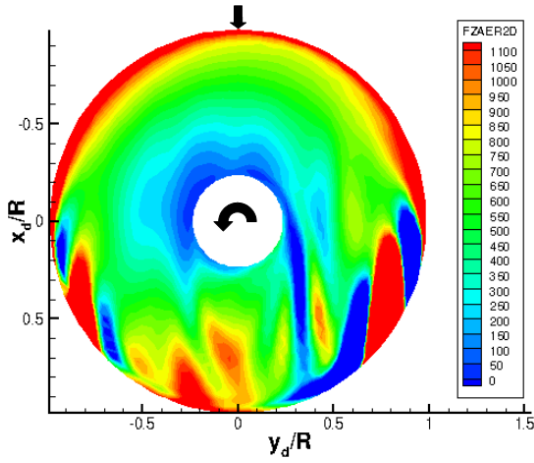


Figure A.3: Axial load distribution computed by BEAT after 6 coupling cycles ($v_h = 20 \text{ m/s}$)

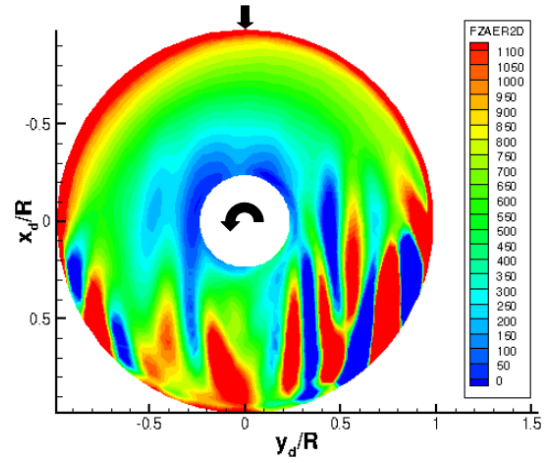


Figure A.4: Axial load distribution computed by BEAT after 8 coupling cycles ($v_h = 20 \text{ m/s}$)

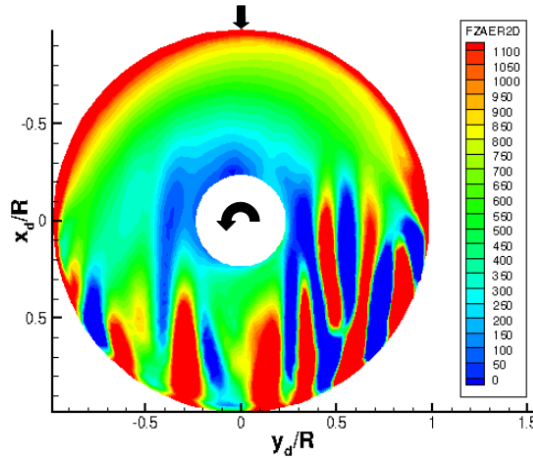


Figure A.5: Axial load distribution computed by BEAT after 10 coupling cycles ($v_h = 20 \text{ m/s}$)

A.2. HIGH SPEED FORWARD FLIGHT ($v_h=66.7 \text{ m/s}$)

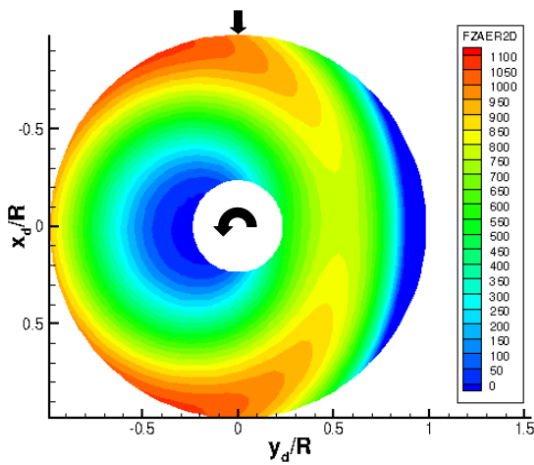


Figure A.6: Initial axial load distribution computed by BEAT ($v_h = 66.7 \text{ m/s}$)

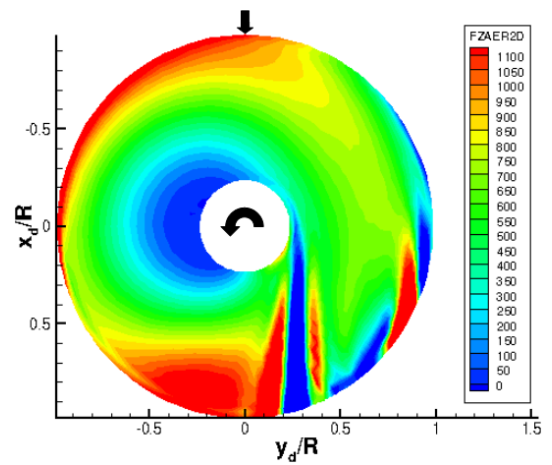


Figure A.7: Axial load distribution computed by BEAT after 3 coupling cycles ($v_h = 66.7 \text{ m/s}$)

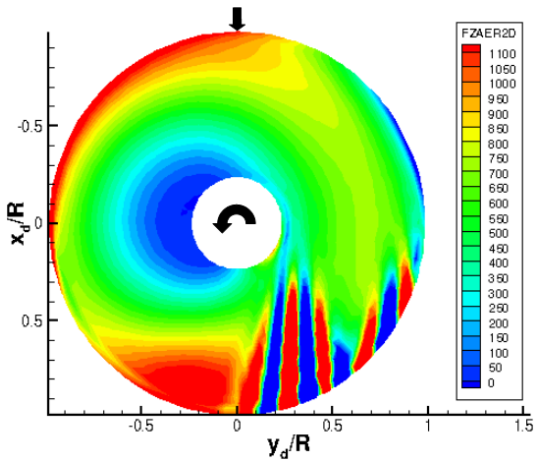


Figure A.8: Axial load distribution computed by BEAT after 6 coupling cycles ($v_h = 66.7$ m/s)

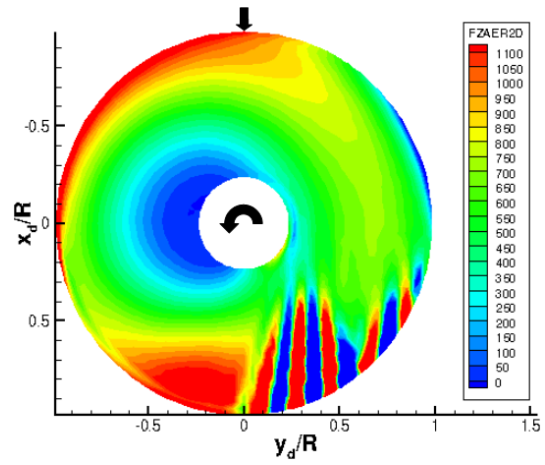


Figure A.9: Axial load distribution computed by BEAT after 8 coupling cycles ($v_h = 66.7$ m/s)

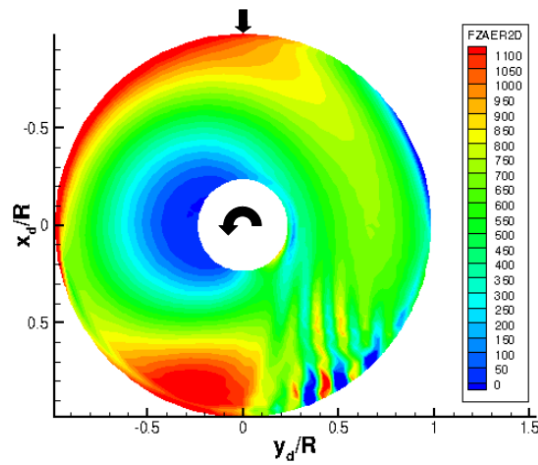


Figure A.10: Axial load distribution computed by BEAT after 10 coupling cycles ($v_h = 66.7$ m/s)

BIBLIOGRAPHY

- [1] W. J. Rankine, *On the mechanical principles of the action of propellers*, Trans. Inst. Naval Architects **6**, 13 (1865).
- [2] R. E. Froude, *On the part played in propulsion by differences of fluid pressure*, Trans. Inst. Naval Architects **30**, 390 (1889).
- [3] G. A. M. Van Kuik, J. N. Sørensen, and V. L. Okulov, *Rotor theories by Professor Joukowski: momentum theories*, Progress in Aerospace Sciences **73**, 1 (2015).
- [4] H. Glauert, *Airplane propellers*, in *Aerodynamic theory* (Springer, 1935) pp. 169–360.
- [5] W. Froude, *On the elementary relation between pitch, slip and propulsive efficiency*, Trans. Inst. Naval Architects **19**, 22 (1878).
- [6] S. Drzewiecki, *Méthode pour la détermination des éléments mécaniques des propulseurs hélicoïdaux* (Association technique maritime, 1892).
- [7] V. L. Okulov, J. N. Sørensen, and D. H. Wood, *The rotor theories by Professor Joukowski: Vortex theories*, Progress in Aerospace Sciences **73**, 19 (2015).
- [8] W. Johnson, *Helicopter theory* (Courier Corporation, 2012).
- [9] G. De Bothezat, *The General Theory of Blade Screws: Including Propellers, Fans, Helicopter Screws, Helicodal Pumps, Turbo-motors, and Different Kinds of Helicodal Brakes*, 29-30 (US Government Printing Office, 1919).
- [10] L. Prandtl, *Tragflügeltheorie. I. Mitteilung*, Nachrichten von der Gesellschaft der Wissenschaften zu Göttingen, Mathematisch-Physikalische Klasse **1918**, 451 (1918).
- [11] S. Goldstein, *On the vortex theory of screw propellers*, Proceedings of the Royal Society of London. Series A, Containing Papers of a Mathematical and Physical Character **123**, 440 (1929).
- [12] J. A. Benek, P. Buning, and J. Steger, *A 3-D chimera grid embedding technique*, in *7th Computational Physics Conference* (1985) p. 1523.
- [13] M. S. Chaffin and J. D. Berry, *Helicopter Fuselage Aerodynamics Under a Rotor by Navier-Stokes Simulation*, Journal of the American Helicopter Society **42**, 235 (1997).
- [14] N. Hariharan, L. Sankar, J. Russell, and P. Chen, *Numerical simulation of the fuselage-rotor interaction phenomenon*, in *34th Aerospace Sciences Meeting and Exhibit* (1996) p. 672.
- [15] R. Meakin, *Moving body overset grid methods for complete aircraft tiltrotor simulations*, in *11th Computational Fluid Dynamics Conference* (1993) p. 3350.

- [16] H. Pomin and S. Wagner, *Navier-Stokes analysis of helicopter rotor aerodynamics in hover and forward flight*, Journal of Aircraft **39**, 813 (2002).
- [17] A. Yang and X. Yang, *Multigrid acceleration and chimera technique for viscous flow past a hovering rotor*, Journal of aircraft **48**, 713 (2011).
- [18] Y. M. Park and O. J. Kwon, *Simulation of unsteady rotor flow field using unstructured adaptive sliding meshes*, Journal of the American Helicopter Society **49**, 391 (2004).
- [19] D. S. Jenney, J. H. Olson, and A. J. Landgrebe, *A Reassessment of Rotor Hovering Performance Prediction Methods*, Journal of the American Helicopter Society **13**, 1 (1968).
- [20] R. H. Miller, *Vortex theory for hovering rotors*, AIAA Journal **20**, 1754 (1982).
- [21] Y. Wang, M. White, and G. Barakos, *Helicopter Wake Encounter Study*, Tech. Rep. (University of Liverpool, 2015).
- [22] A. J. Landgrebe, *The wake geometry of a hovering helicopter rotor and its influence on rotor performance*, Journal of the American Helicopter Society **17**, 3 (1972).
- [23] T. S. Beddoes, *A wake model for high resolution airloads*, in *International Conference on Rotorcraft Basic Research, Research Triangle Park, NC, Proceedings*, Vol. 19 (1985).
- [24] J. G. Leishman, M. J. Bhagwat, and A. Bagai, *Free-vortex filament methods for the analysis of helicopter rotor wakes*, Journal of aircraft **39**, 759 (2002).
- [25] I. Fejtek and L. Roberts, *Navier-Stokes computation of wing/rotor interaction for a tilt rotor in hover*, AIAA journal **30**, 2595 (1992).
- [26] E. B. Giovanetti and K. C. Hall, *Axisymmetric potential flow model of single or coaxial actuator disks*, in *72nd Annual Forum-AHS International* (2016).
- [27] R. G. Rajagopalan and S. R. Mathur, *Three dimensional analysis of a rotor in forward flight*, Journal of the American Helicopter Society **38**, 14 (1993).
- [28] J. T. Conway, *Exact actuator disk solutions for non-uniform heavy loading and slip-stream contraction*, Journal of Fluid Mechanics **365**, 235 (1998).
- [29] D. O'Brien and M. Smith, *Analysis of rotor-fuselage interactions using various rotor models*, in *43rd AIAA Aerospace Sciences Meeting and Exhibit* (2005) p. 468.
- [30] F. Le Chuiton, *Actuator disc modelling for helicopter rotors*, Aerospace Science and Technology **8**, 285 (2004).
- [31] G. Gaonkar and D. Peters, *Review of dynamic inflow modeling for rotorcraft flight dynamics*, in *27th Structures, Structural Dynamics and Materials Conference* (1988) p. 845.
- [32] W. R. M. Van Hoydonck, H. Haverdings, and M. D. Pavel, *A review of rotorcraft wake modeling methods for flight dynamics applications*, in *35th European Rotorcraft Forum* (2009).

- [33] P. J. Carpenter and B. Fridovich, *Effect of a rapid blade-pitch increase on the thrust and induced-velocity response of a full-scale helicopter rotor*, (1953).
- [34] D. M. Pitt and D. A. Peters, *Theoretical prediction of dynamic-inflow derivatives*, *Vertica* **5**, 21 (1981).
- [35] D. A. Peters and C. J. He, *Correlation of Measured Induced Velocities with a Finite-State Wake Model*, *Journal of the American Helicopter Society* **36**, 59 (1991).
- [36] D. A. Peters, *How dynamic inflow survives in the competitive world of rotorcraft aerodynamics*, *Journal of the American Helicopter Society* **54**, 11001 (2009).
- [37] J. J. Chattot, *Actuator Disk Theory-Steady and Unsteady Models*, *Journal of Solar Energy Engineering* **136** (2014).
- [38] W. Yu, C. Simao Ferreira, and G. van Kuik, *Analytical actuator disc solution for unsteady load*, in *34th Wind Energy Symposium* (2016) p. 0751.
- [39] R. G. Rajagopalan and C. K. Lim, *Laminar flow analysis of a rotor in hover*, *Journal of the American Helicopter Society* **36**, 12 (1991).
- [40] N. Kroll, C. C. Rossow, K. Becker, and F. Thiele, *MEGAFLOW-a numerical flow simulation system*, in *21st ICAS congress* (1998) pp. 13.09–18.09.
- [41] T. Gerhold, *Overview of the hybrid RANS code TAU*, in *MEGAFLOW-Numerical Flow Simulation for Aircraft Design* (Springer, 2005) pp. 81–92.
- [42] K. Pahlke and B. G. Van Der Wall, *Chimera simulations of multibladed rotors in high-speed forward flight with weak fluid-structure-coupling*, *Aerospace Science and Technology* **9**, 379 (2005).
- [43] M. Costes, J. Raddatz, S. Borie, L. Sudre, A. D’Alascio, M. Embacher, and P. Spiegel, *Advanced rotorcraft aeromechanics studies in the French-German SHANEL project*, in *35th European Rotorcraft Forum* (2009).
- [44] M. Imiela, *High-fidelity optimization framework for helicopter rotors*, *Aerospace Science and Technology* **23**, 2 (2012).
- [45] K. Pahlke and B. G. van der Wall, *Progress in weak fluid-structure-coupling for multibladed rotors in high-speed forward flight*, in *28th European Rotorcraft Forum Proceedings* (2002) pp. 67.1–67.13.
- [46] B. Benoit, A. M. Dequin, K. Kampa, W. von Grünhagen, P. M. Basset, and B. Gimonet, *HOST, a General Helicopter Simulation Tool for Germany and France*, in *American Helicopter Society, 56th Annual Forum and Technology Display, Virginia Beach, USA, May 2-4* (2000).
- [47] G. Wilke, *Multi-objective optimizations in rotor aerodynamics using variable fidelity simulations*, in *38th European Rotorcraft Forum*, Vol. 1 (38th European Rotorcraft Forum, 2013) pp. 1–13.

- [48] B. G. van der Wall, B. Junker, C. Burley, T. Brooks, Y. Yu, C. Tung, M. Raffel, H. Richard, W. Wagner, E. Mercker, *et al.*, *The hart ii test in the llf of the dnw-a major step towards rotor wake understanding*, in *28th European Rotorcraft Forum Proceedings* (2002) pp. 42–1.
- [49] T. Schwarz and K. Pahlke, *The GOAHEAD project - overview and selected results*, in *36th European Rotorcraft Forum* (2010).
- [50] S. R. Ahmed and V. T. Vidjaja, *Unsteady panel method calculation of pressure distribution on BO 105 model rotor blades*, *Journal of the American Helicopter Society* **43**, 47 (1998).
- [51] J. P. Yin and S. R. Ahmed, *Helicopter Main-Rotor/Tail-Rotor Interaction*, *Journal of the American helicopter society* **45**, 293 (2000).
- [52] J. Yin, B. G. van der Wall, and G. Wilke, *Rotor aerodynamic and noise under influence of elastic blade motion and different fuselage modeling*, in *40th European Rotorcraft Forum (ERF) 2014* (2014).
- [53] G. Wilke, *Variable fidelity optimization of required power of rotor blades: Investigation of aerodynamic models and their application*, (2012).
- [54] G. Wilke, *Efficient aero-acoustic simulation of the hart ii rotor with the compact pade scheme*, in *42nd European Rotorcraft Forum* (2016).
- [55] A. R. Bramwell, D. Balmford, and G. Done, *Bramwell's helicopter dynamics* (Butterworth-Heinemann, 2001).
- [56] R. T. N. Chen, *A survey of nonuniform inflow models for rotorcraft flight dynamics and control applications*, *Vertica* **14**, 147 (1990).
- [57] A. Markus, *Modern Fortran in practice* (Cambridge University Press, 2012).
- [58] G. J. Leishman, *Principles of helicopter aerodynamics* (Cambridge university press, 2006).
- [59] J. Shaw, N. Albion, E. J. Hanker, and R. S. Teal, *Higher harmonic control: wind tunnel demonstration of fully effective vibratory hub force suppression*, *Journal of the American Helicopter Society* **34**, 14 (1989).
- [60] R. W. Prouty and H. C. Curtiss, *Helicopter control systems: A history*, *Journal of Guidance, Control, and Dynamics* **26**, 12 (2003).
- [61] W. Van Hoydonck, *Computation of Rotorcraft Wake Geometry using NURBS*, Ph.D. thesis, TU Delft, Delft University of Technology (2013).
- [62] A. Gessow and A. D. Crim, *A method for studying the transient blade-flapping behavior of lifting rotors at extreme operating conditions* (National Advisory Committee for Aeronautics, Washington, DC, 1955).

- [63] A. Gessow, *Equations and procedures for numerically calculating the aerodynamic characteristics of lifting rotors* (National Advisory Committee for Aeronautics, Washington, D.C., 1956).
- [64] R. Roos, D. Weber-Steinhaus, and M. S. Muttulingam, *Failure analysis of a star segment*, in *Proceedings of the American Society for Composites* (2014).
- [65] M. J. Smith, J. W. Lim, B. G. van der Wall, J. D. Baeder, R. T. Biedron, D. D. Boyd Jr, B. Jayaraman, S. N. Jung, and B.-Y. Min, *An assessment of CFD/CSD prediction state-of-the-art using the HART II international workshop data*, in *68th Annual Forum of the American Helicopter Society, Ft. Worth, TX* (2012).
- [66] M. Rwigema, *Propeller blade element momentum theory with vortex wake deflection*, in *Proceedings of the 27th Congress of the International Council of the Aeronautical Sciences, Nice, France, September* (2010) pp. 19–24.
- [67] J. Blazek, *Computational fluid dynamics: principles and applications* (Butterworth-Heinemann, 2015).
- [68] T. Gerhold, M. Galle, O. Friedrich, J. Evans, T. Gerhold, M. Galle, O. Friedrich, and J. Evans, *Calculation of complex three-dimensional configurations employing the DLR-TAU-code*, in *35th Aerospace Sciences Meeting and Exhibit*, p. 167.
- [69] A. Schwöppe and B. Diskin, *Accuracy of the Cell-Centered Grid Metric in the DLR TAU-Code*, in *New Results in Numerical and Experimental Fluid Mechanics VIII* (Springer, 2013) pp. 429–437.
- [70] L. Alcaraz Capsada, *Simulation of atmospheric effects with the DLR code TAU*, (2015).
- [71] P. Aumann, H. Barnewitz, H. Schwarten, K. Becker, R. Heinrich, B. Roll, M. Galle, N. Kroll, T. Gerhold, D. Schwamborn, *et al.*, *MEGAFLOW: Parallel complete aircraft CFD*, *Parallel Computing* **27**, 415 (2001).
- [72] T. Alrutz, *Investigation of the parallel performance of the unstructured DLR-TAU-Code on distributed computing systems*, *Proceedings of Parallel CFD 2005*, 509 (2005).
- [73] E. Andres, M. Widhalm, and A. Caloto, *Achieving High Speed CFD Simulations: Optimization, Parallelization, and FPGA Acceleration for the Unstructured DLR TAU Code*, in *Proc. 47th AIAA Aerospace Sciences Meeting Including The New Horizons Forum and Aerospace Exposition, Orlando, FL, January* (2009) pp. 5–8.
- [74] T. Schwarz, *The overlapping grid technique for the time accurate simulation of rotorcraft flows*, (2005).
- [75] C. Wolf, *A Chimera Simulation Method and Detached Eddy Simulation for Vortex-Airfoil Interactions*, Ph.D. thesis, Georg-August-Universität Göttingen (2011).
- [76] V. Hannemann, *Structured multigrid agglomeration on a data structure for unstructured meshes*, *International journal for numerical methods in Fluids* **40**, 361 (2002).

- [77] S. Langer, A. Schwöppe, and N. Kroll, *Investigation and comparison of implicit smoothers applied in agglomeration multigrid*, AIAA Journal (2015).
- [78] R. Schweikhard, *Actuator Disk for Helicopter Rotors in an Unstructured Flow Solver*, Journal of the American Helicopter Society **52**, 58 (2007).
- [79] DLR, *Technical Documentation of the DLR TAU-Code Release 2016.1.0*, Tech. Rep. (Institute of Aerodynamics and Flow Technology, 2016).
- [80] A. Raichle, S. Melber-Wilkending, and J. Himisch, *A New Actuator Disk Model for the TAU Code and Application to a Sailplane with a Folding Engine*, New Results in Numerical and Experimental Fluid Mechanics VI, 52 (2008).
- [81] E. Turkel, *Preconditioning techniques in computational fluid dynamics*, Annual Review of Fluid Mechanics **31**, 385 (1999).
- [82] H. van der Ven and O. Boelens, *High-order simulation of a rotor in forward flight using a four-dimensional adaptive flow solver*, in *Symposium on High Fidelity Flow Simulations*, Vol. 2 (2010).
- [83] A. Bauknecht, B. Ewers, C. Wolf, F. Leopold, J. Yin, and M. Raffel, *Three-dimensional reconstruction of helicopter blade-tip vortices using a multi-camera BOS system*, Experiments in Fluids **56**, 1866 (2015).
- [84] B. G. van der Wall, *2nd HHC aeroacoustic rotor test (HART II)-Part I: Test Documentation*, (2003).
- [85] B. G. van der Wall and C. L. Burley, *2nd HHC aeroacoustic rotor test (HART II)-Part II: representative results*, (2005).
- [86] B. G. van der Wall, M. Wentrup, G. Rajagopalan, S. N. Jung, and J. Yin, *A simple analytical model for investigation of fuselage-rotor interference*, in *72nd Annual Forum-AHS International* (2016).
- [87] A. Länger, *Validation of TAU-HOST coupling chain with HART-II test cases*, (2014).